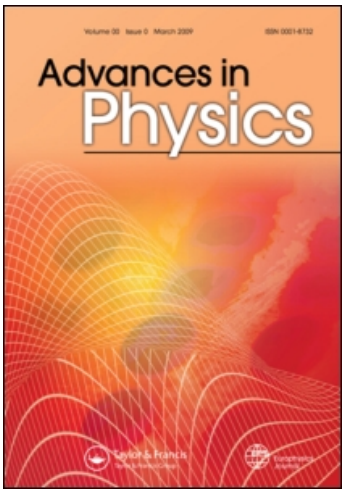

Advances in Physics
Publication details, including instructions for authors and subscription information:
http://www.informaworld.com/smpp/title~content=t713736250

Dynamics and statistical mechanics of ultra-cold Bose gases using c-field techniques

P. B. Blakie [a]; A. S. Bradley [ab]; M. J. Davis [b]; R. J. Ballagh [a]; C. W. Gardiner [a]
[a] Jack Dodd Centre for Quantum Technology, Department of Physics, University of Otago, Dunedin, New Zealand [b] The University of Queensland, School of Physical Sciences, ARC Centre of Excellence for Quantum-Atom Optics, Queensland 4072, Australia

Online Publication Date: 01 September 2008

To cite this Article Blakie, P. B., Bradley, A. S., Davis, M. J., Ballagh, R. J. and Gardiner, C. W.(2008)'Dynamics and statistical mechanics of ultra-cold Bose gases using c-field techniques',Advances in Physics,57:5,363 — 455
To link to this Article: DOI: 10.1080/00018730802564254
URL: http://dx.doi.org/10.1080/00018730802564254

Advances in Physics
Vol. 57, No. 5, September–October 2008, 363–455

Taylor & Francis
Taylor & Francis Group

Dynamics and statistical mechanics of ultra-cold Bose gases using c-field techniques

P.B. Blakie[a]*†, A.S. Bradley[ab]†, M.J. Davis[b], R.J. Ballagh[a] and C.W. Gardiner[a]

[a]*Jack Dodd Centre for Quantum Technology, Department of Physics, University of Otago, Dunedin, New Zealand;* [b]*The University of Queensland, School of Physical Sciences, ARC Centre of Excellence for Quantum-Atom Optics, Queensland 4072, Australia*

(*Received 31 August 2008; final version received 17 October 2008*)

We review phase-space techniques based on the Wigner representation that provide an approximate description of dilute ultra-cold Bose gases. In this approach the quantum field evolution can be represented using equations of motion of a similar form to the Gross–Pitaevskii equation but with stochastic modifications that include quantum effects in a controlled degree of approximation. These techniques provide a practical quantitative description of both equilibrium and dynamical properties of Bose gas systems. We develop versions of the formalism appropriate at zero temperature, where quantum fluctuations can be important, and at finite temperature where thermal fluctuations dominate. The numerical techniques necessary for implementing the formalism are discussed in detail, together with methods for extracting observables of interest. Numerous applications to a wide range of phenomena are presented.

Keywords: Ultra-cold Bose gas; Quantum and finite temperature dynamics

Contents

*Corresponding author. Email: bblakie@physics.otago.ac.nz
†The first two authors acknowledge equal contributions to this review.

ISSN 0001–8732 print/ISSN 1460–6976 online

DOI: 10.1080/00018730802564254
http://www.informaworld.com

1. Introduction

The dilute ultra-cold Bose gas presents a rare opportunity for theoretical physics: it has well-characterized interactions, and it is feasible to begin with the full quantum theory and subsequently use well-controlled approximations to develop formalisms suitable for calculations. These systems can be precisely manipulated and observed in experiments and offer a unique chance to compare computational quantum field theories directly with experiments.

Several aspects of experiments present challenges for theory. First, the experiments are usually non-equilibrium with long relaxation times and are well beyond any sort of linearized treatment. Second, the harmonic trapping potentials used in experiments complicate the traditional many-body methods which are more suitable for uniform systems. The low-energy collective dynamics and numerous finite-sized aspects of this system critically rely on the external potential being treated as a primary consideration of the theory.

At zero temperature an almost pure Bose–Einstein condensate (BEC) forms, and for a wide range of situations its dynamics are well described by the time-dependent Gross–Pitaevskii equation (GPE); see, e.g., [1,2]. This approach assumes that all of the atoms are well represented by a single condensate wavefunction, and the GPE describes the coherent evolution of this wavefunction neglecting all spontaneous and incoherent processes. However, experiments routinely operate in regimes where such processes are important and the GPE provides an inadequate physical description, and we provide some examples below.

- At higher temperatures, approaching the condensation temperature, T_c, a sizable thermal cloud will be present. Experiments examining collective oscillation frequencies of BECs found that for temperatures higher than about $0.6T_c$ the GPE, owing to its neglect of the interplay between the condensate and thermal cloud, incorrectly predicts the collective mode frequencies and damping [3–5].
- Two nearly-pure BECs colliding produce a halo of atoms scattered onto a spherical shell in momentum space [6]. Provided that the phase-space density of the scattered atoms is low, this can be viewed as incoherent scattering of the individual atoms in the condensates, and the GPE can be augmented [7] to account for these. However, at higher scattered densities Bose stimulation becomes important, and a theory which includes both Bose stimulation as well as incoherent scattering is required.

In order to treat these examples and many others it is necessary to formulate a description of Bose gases that combines coherent and incoherent physics in a general, yet tractable manner. The key to a successful theoretical approach is the recognition that in all of these examples, even when there is no BEC, one or many modes of the system have an occupation which is much larger than one quantum. The systems are then highly Bose degenerate, and the matter-wave field behaves much like a classical field. A set of theoretical approaches relying on the existence of significant Bose degeneracy, known generically as *c-field* methods, provide a comprehensive solution to this problem.

An example simulation demonstrating such a scenario is shown in Figure 1. The averaged momentum density of a c-field simulation (see Section 3) which describes many degenerate modes of a trapped Bose gas is shown for a range of temperatures spanning the critical temperature. The condensate is seen to emerge from the broad thermal cloud as the temperature decreases below T_c.

There are two main unifying features of the c-field techniques we present in this review. The first is that the modes of the field theoretic description are divided into two regions.

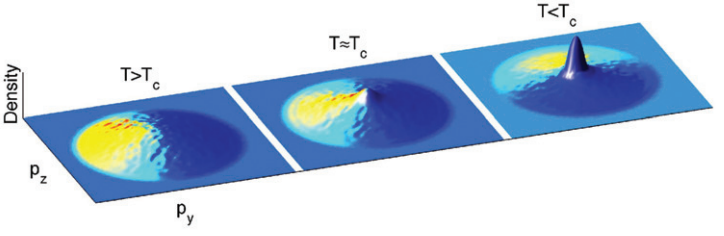

Figure 1. Momentum space density (logarithmic) for classical field simulations at various temperatures. Emergence of the condensate is visible as a prominent spike at temperatures below T_c.

The precise way this is done depends on the approach, but generically we have the following two regions.

C: **c-field region.** This region is of primary importance in the description of the system and is so-named because it is simulated using classical stochastic field equations. In the theories we develop here this region is chosen to contain not only the condensate, but all other highly Bose-degenerate modes. It may also contain modes of low occupation in which important dynamics occur.

I: **Incoherent region.** This region consists of the remaining modes which will individually be sparsely occupied (high-energy) thermal or vacuum modes. Depending on the temperature and the density of states this region may contain a significant or even dominant fraction of the total number of particles in the system. However, they have only a weak influence on the dynamics of the c-field region. In the techniques we develop in this review the static and dynamical properties of this region will be approximated as being incoherent.

The second common feature to the c-field techniques is that their evolution equations are of similar form to the GPE, but with important modifications. This is the primary advantage of the formalism: its computational tractability and capability to simulate experimentally realistic parameter regimes.

This review is organized as follows. We begin in Section 2 where we outline the background theory relevant to the application of c-field techniques[1]. We then identify three separate implementations of the c-field techniques for different physical regimes, which are subsequently described in their own sections.

These techniques are as follows.

(i) **Projected GPE (PGPE).** In all c-field approaches the GPE-like evolution is strictly limited to the **C** region. This is implemented using a projection operator, and when this is the sole modification of the GPE we refer to the evolution equation as the *projected* GPE (PGPE).

The PGPE is used to simulate the c-field region as a microcanonical system, i.e. as an isolated system of fixed energy and number, with all couplings to the incoherent region neglected. This approach is valid for high temperatures ($T \sim T_c$) where the energy cutoff is chosen so that all c-field region modes are highly occupied, and quantum fluctuations can be neglected. This theory is discussed in Section 3, along with applications of this formalism to finite temperature phenomena.

(ii) **Truncated Wigner PGPE (TWPGPE).** When there are modes with low occupation in the c-field region, additional noise terms must be included in the initial conditions to model the quantum-mechanical vacuum fluctuations. Inclusion of quantum fluctuations cannot be done exactly, but can be well approximated by stochastic sampling of a Wigner distribution for the initial state of the system. The method introduces spontaneous processes which are absent in the pure GPE theory for which all scattering is stimulated. This formalism underlies all of the c-field techniques and is presented in Section 2.3, with applications of the theory to the non-equilibrium dynamics of systems at $T \ll T_c$ considered in Section 4.

(iii) **Stochastic PGPE (SPGPE).** When exchange of energy and matter between the c-field region and the incoherent region is important, additional noise terms appear in the theory as well as in the initial conditions, via the truncated Wigner function method as above.

This approach is applicable in the same temperature regime as the PGPE, however it differs from that formalism in that scattering processes, which couple to the incoherent region, are included. The theory is implemented by solving the PGPE with additional dissipative and stochastic terms. This transforms the description of the c-field region to a grand canonical form which includes the exchange of particles and energy between the regions. This method, discussed in Section 5, is well suited for modelling the dynamics of evaporative cooling and, for example, vortex formation during Bose–Einstein condensation.

In all of the above c-field techniques it is important to ensure that the numerical solutions of the equations inside the c-field region do not develop components outside that region. Significant research has gone into developing numerical methods for efficiently evolving projected equations, particularly the challenge of implementing a projection operator efficiently and without compromising the tractability of the equation compared with the usual GPE. This is discussed further in Appendix A and Appendix B. In this review we show that a wide range of problems can be solved using these methods, and that accurate and reliable quantitative results can be computed.

2. Background formalism

2.1. *Effective field theory for the dilute Bose gas*

In this section we develop the basic formalism for the review. We begin by restricting the full Hamiltonian to a low-energy subspace, **L**, for which an *effective* field theory provides an accurate description of the gas with a contact interaction. We then further divide this subspace into the **C** and **I** regions central to our development of the c-field techniques. Our basic approach here follows the derivation given in [8].

Our starting point for describing a system of bosonic atoms interacting via an interatomic potential $U(\mathbf{x})$ is the second quantized Hamiltonian

$$\hat{H} = \int d^3\mathbf{x}\, \hat{\Psi}^\dagger(\mathbf{x}) H_{\rm sp} \hat{\Psi}(\mathbf{x}) + \frac{1}{2}\int\int d^3\mathbf{x}\, d^3\mathbf{x}'\, \hat{\Psi}^\dagger(\mathbf{x})\hat{\Psi}^\dagger(\mathbf{x}')U(\mathbf{x}-\mathbf{x}')\hat{\Psi}(\mathbf{x}')\hat{\Psi}(\mathbf{x}), \tag{1}$$

where $\hat{\Psi}(\mathrm{x})$ is the bosonic field operator, and

$$H_{\rm sp} = H_0 + \delta V(\mathbf{x}, t), \tag{2}$$

$$H_0 = -\frac{\hbar^2\nabla^2}{2m} + V_0(\mathbf{x}), \tag{3}$$

are the *single particle* and *basis* Hamiltonians, respectively, with $V_0(\mathbf{x})$ the external potential. These Hamiltonians differ by the inclusion of a 'perturbation potential' $\delta V(\mathbf{x}, t)$, which we include for generality. The basis Hamiltonian, H_0, is so-named because we use its eigenstates as a basis for the low-energy description of the system, in particular to define the c-field region in Section 2.2. The inter-atomic potential, $U(\mathbf{x})$, has a size characterized by the effective range parameter, r_0, and only depends on the relative separation of the atoms.

In typical ultra-cold atom experiments the length scales of interest are much greater than r_0, and the full details of the inter-atomic potential are unnecessary. It is desirable,

therefore, to develop a theory that eliminates the need to consider such small length scales, and hence the microscopic details of the collisional interaction can be parameterized in terms of the S-wave scattering length alone: such an approach is known as an *effective field theory*.

Formally this procedure can be implemented by restricting our attention to a *low-energy subspace*, **L**, that is spanned by single-particle states of energy less than an appropriately chosen energy cutoff $E_{\max}$. This eliminates all momentum states with momentum exceeding $\hbar\Lambda(\mathbf{x}) \simeq \sqrt{2m(E_{\max} - V_0(\mathbf{x}))}$ at $\mathbf{x}$, and in doing so effectively 'coarse grains' our description to a length scale of $1/\Lambda(\mathbf{x})$. While our choice of $E_{\max}$ is in principle arbitrary, the following criteria ensure a simple and accurate effective field theory emerges.

(i) We have $E_{\max} \ll h^2/2mr_0^2$, so that we eliminate the need to include short-wavelength components of the wavefunction that occur in the interaction region. Integrating out these high-energy states allows the inter-atomic interaction to be replaced by the two-body T-matrix, which in the zero energy limit becomes [8,9]

$$T(0) \to g = \frac{4\pi a_s \hbar^2}{m}, \tag{4}$$

where a_s is the S-wave scattering length.

(ii) We have $E_{\max} \gg k_B T, \mu$, where μ is the chemical potential, so that the eliminated states will not be occupied by thermal or interaction effects. This requirement ensures that the T-matrix does not depend on the population of states that are eliminated in the theory, i.e. avoiding the need to consider a many-body T-matrix.

As long as these conditions are satisfied, the effective field theory derived should be insensitive to the precise value of $E_{\max}$ used.

We can introduce a coarse-grained field operator, $\hat{\psi}(\mathbf{x})$, which only contains modes in **L**, and is described by the *effective* Hamiltonian

$$\hat{H}_{\text{eff}} = \int d^3\mathbf{x}\, \hat{\psi}^\dagger(\mathbf{x}) H_{\text{sp}} \hat{\psi}(\mathbf{x}) + \frac{u}{2} \int d^3\mathbf{x}\, \hat{\psi}^\dagger(\mathbf{x}) \hat{\psi}^\dagger(\mathbf{x}) \hat{\psi}(\mathbf{x}) \hat{\psi}(\mathbf{x}). \tag{5}$$

It must be emphasized that this resulting field theory has a cutoff, so that the commutation relations of these new field operators are not precise delta functions:

$$[\hat{\psi}(\mathbf{x}), \hat{\psi}^\dagger(\mathbf{x}')] = \delta_{\mathbf{L}}(\mathbf{x} - \mathbf{x}'). \tag{6}$$

In Equation (5), we have introduced the coupling constant

$$u = \frac{g}{1 - g \int_{\mathbf{L}} d^3k\, (\hbar^2 k^2/(2\pi)^3 m)}, \tag{7}$$

where the integral is taken over the momentum space of the **L**-region and accounts for the cutoff dependence of the coupling constant (see, e.g., [10, Appendix A]).

For the special case where the potential is slowly varying compared with the local cutoff wavevector $\Lambda(\mathbf{x})$, we have $\delta_{\mathbf{L}}(\mathbf{x} - \mathbf{x}') \simeq \sin(\Lambda(\mathbf{x})|\mathbf{x}' - \mathbf{x}|)/2\pi^2|\mathbf{x}' - \mathbf{x}|^3$. The function $\delta_{\mathbf{L}}$ plays the role of a kind of coarse-grained delta function which in general has a spatially dependent width; however, it is also a projector into the subspace of non-eliminated modes.

Using the commutation relation (6) the Heisenberg equation of motion for the corresponding field operator takes the form

$$i\hbar\frac{\partial\hat{\psi}(\mathbf{x})}{\partial t}=\int d^3\mathbf{x}'\,\delta_{\mathbf{L}}(\mathbf{x}-\mathbf{x}')\left\{H_{\rm sp}\hat{\psi}(\mathbf{x}')+u\hat{\psi}^{\dagger}(\mathbf{x}')\hat{\psi}(\mathbf{x}')\hat{\psi}(\mathbf{x}')\right\}. \tag{8}$$

The main purpose of the methods discussed in this review is to simulate this equation in various regimes.

2.2. *Projection into the c-field region*

2.2.1. *Projection operators*

In Section 2.1, we developed an effective field theory description of the cold-atom Hamiltonian derived by eliminating states outside of the **L** region. The resulting effective Hamiltonian (5) and equation of motion (8) are restricted to this space.

We now turn to a quantitative definition of the **L** region. This is accomplished by expanding the coarse-grained field operator as

$$\hat{\psi}(\mathbf{x})=\sum_{n\in\mathbf{L}}\hat{a}_n\phi_n(\mathbf{x}), \tag{9}$$

where $\phi_n(\mathbf{x})$ are single-particle eigenstates of the basis Hamiltonian with energy ϵ_n, i.e.

$$\epsilon_n\phi_n(\mathbf{x})=H_0\phi_n(\mathbf{x}). \tag{10}$$

The operators $\hat{a}_n$ satisfy the usual Bose commutation relations, $[\hat{a}_i,\hat{a}_j]=0$, and $[\hat{a}_i,\hat{a}_j^{\dagger}]=\delta_{ij}$. The restriction of the summation in (9) to modes in **L** is defined by $\mathbf{L}=\{n:\epsilon_n\le E_{\rm max}\}$.

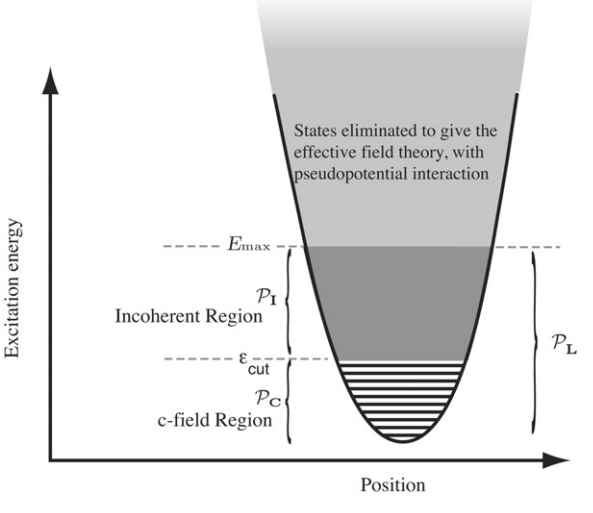

Figure 2. Schematic view of the c-field region, the incoherent region and eliminated states for a harmonic trap. The c-field atoms require a quantum description and incoherent atoms may be treated using quantum kinetic theory.

In general the requirements put on $E_{\max}$ for a useful effective field theory to emerge lead to an **L**-space that is far too large to simulate. Furthermore, the validity conditions for the c-field methods typically restrict their application to describing a subsystem of **L.** Thus, it is necessary to further subdivide **L** into two regions as follows (see Figure 2).

(i) The *c-field region* $(\mathbf{C})^2$, which will normally consist of the lowest energy modes in **L** and will be numerically simulated using classical fields.
(ii) The *incoherent region* (**I**), consisting of all of the modes of **L** not in **C**. The choice of **I** will be such that any atoms occupying this region will be best described by a particle-like description.

For all cases considered in this review, these regions are defined by a single-particle energy $\epsilon_{\rm cut}$, such that **C** is spanned by the single-particle modes with energy $\epsilon \leq \epsilon_{\rm cut}$ and **I** is spanned by the single-particle modes with energy $\epsilon_{\rm cut} < \epsilon < E_{\max}$. We define projectors for these regions as

$$\mathcal{P}_{\mathbf{C}}\{F(\mathbf{x})\} \equiv \sum_{n\in\mathbf{C}} \phi_n(\mathbf{x}) \int d^3\mathbf{x}'\, \phi_n^*(\mathbf{x}')F(\mathbf{x}'), \tag{11}$$

$$\mathcal{P}_{\mathbf{I}}\{F(\mathbf{x})\} \equiv \sum_{n\in\mathbf{I}} \phi_n(\mathbf{x}) \int d^3\mathbf{x}'\, \phi_n^*(\mathbf{x}')F(\mathbf{x}'), \tag{12}$$

where $\mathbf{C} = \{n : \epsilon_n \leq \epsilon_{\rm cut}\}$ and $\mathbf{I} = \{n : \epsilon_{\rm cut} < \epsilon_n \leq E_{\max}\}$, such that $\mathbf{L} = \mathbf{C} + \mathbf{I}$ and $\mathcal{P}_{\mathbf{I}}\mathcal{P}_{\mathbf{C}} \equiv 0$.

We define quantum field operators for the c-field and incoherent regions as

$$\hat{\psi}_{\mathbf{C}}(\mathbf{x}) \equiv \mathcal{P}_{\mathbf{C}}\{\hat{\psi}(\mathbf{x})\} = \sum_{n\in\mathbf{C}} \hat{a}_n\phi_n(\mathbf{x}), \tag{13}$$

$$\hat{\psi}_{\mathbf{I}}(\mathbf{x}) \equiv \mathcal{P}_{\mathbf{I}}\{\hat{\psi}(\mathbf{x})\} = \sum_{n\in\mathbf{I}} \hat{a}_n\phi_n(\mathbf{x}), \tag{14}$$

$$\hat{\psi}(\mathbf{x}) = \hat{\psi}_{\mathbf{C}}(\mathbf{x}) + \hat{\psi}_{\mathbf{I}}(\mathbf{x}). \tag{15}$$

Most of the theoretical developments in this review are made in terms of the $\hat{\psi}_{\mathbf{C}}(\mathbf{x})$ and $\hat{\psi}_{\mathbf{I}}(\mathbf{x})$ operators.

Properties of projectors. It is important to note that the kernel of the $\mathcal{P}_{\mathbf{C}}$-projector, namely

$$\delta_{\mathbf{C}}(\mathbf{x}, \mathbf{x}') \equiv \sum_{n\in\mathbf{C}} \phi_n(\mathbf{x})\phi_n^*(\mathbf{x}'), \tag{16}$$

is the commutator of the c-field operator, i.e.

$$[\hat{\psi}_{\mathbf{C}}(\mathbf{x}), \hat{\psi}_{\mathbf{C}}^{\dagger}(\mathbf{x}')] = \delta_{\mathbf{C}}(\mathbf{x}, \mathbf{x}'). \tag{17}$$

The function $\delta_{\mathbf{C}}$ plays the role of a Dirac-delta function for any function in **C**, e.g.,

$$\int d^3\mathbf{x}'\delta_{\mathbf{C}}(\mathbf{x}, \mathbf{x}')\psi_{\mathbf{C}}(\mathbf{x}') = \psi_{\mathbf{C}}(\mathbf{x}), \tag{18}$$

which also follows from the idempotence property, $\mathcal{P}_{\mathbf{C}}\mathcal{P}_{\mathbf{C}} \equiv \mathcal{P}_{\mathbf{C}}$. The imposition of an energy cutoff thus has major consequences for the field theory. Imposing a cutoff in momentum leads to a discretized form of the continuous field theory with $\delta_{\mathbf{C}}(\mathbf{x}_j, \mathbf{x}_k) = \delta_{jk}/\Delta V$ for a lattice representation with volume ΔV per lattice point. Imposing it in another basis leads to a field theory with a position-dependent commutator (16).

2.2.2. *The Hamiltonian and equation of motion*

The effective Hamiltonian can now be rewritten in terms of $\hat{\psi}_{\mathbf{C}}$ and $\hat{\psi}_{\mathbf{I}}$, and because the projection is in terms of eigenfunctions of the single-particle Hamiltonian, cross terms in the result will appear only in the quartic interaction term. The different ways of approaching the implementation of the c-field theory depend on the how these cross terms, which connect **C** and **I**, are dealt with. The three cases are as follows.

(i) **PGPE.** The cross terms are dropped, but it is assumed that all mode occupations in **C** are significantly greater than one throughout the dynamical evolution. Thus, there is significant occupation of **I**, but this is taken as fully thermalized, and conditions are chosen so that when the motion in **C** reaches equilibrium it matches smoothly to **I**.

(ii) **TWPGPE.** Here one deals with processes in which many modes in **C** are unoccupied, including all of the higher modes. In this case **I** is unoccupied, and the effect of the cross terms is negligible, and they are dropped. However, the quantum fluctuations in **C** have a significant effect, and this is taken into account by including a random element corresponding to half a quantum occupation in each mode.

(iii) **SPGPE.** Here one accounts for interactions between **C** and **I** by assuming that **I** is thermally occupied, and by using quantum stochastic techniques, terms which involve dynamic noise and damping are introduced. When the TWPGPE is also used, the resulting equation of motion is a modified PGPE with noise and damping.

These methods differ in both their conditions for validity and in the details of their numerical implementation. We stress that, in general, a system may evolve from a regime where (ii) is the best description (zero-temperature BEC), through to a regime where (i) is applicable (a thermalized classical field), and finally through sufficient heating, to the realm where (iii) may be appropriate. The parameters determining this crossover, and therefore the appropriate definition of **C** and **I**, are the mode occupancies, strength of interactions and temperature of the system which are, in general, time dependent. Thus, some care must be taken when applying the methods and we return to this point when discussing validity criteria in Section 2.3.9.

2.3. *Wigner formalism and the truncated Wigner approximation*

The justification for all three c-field techniques can be made using a Wigner distribution methodology. A discussion of the properties of the Wigner distribution can be found in many places (see, for example, [11,12]). Here we provide an introduction to the theory using the single mode case in Sections 2.3.1 and 2.3.2, before discussing the quantum field case in Section 2.3.3.

2.3.1. *Wigner representation of a single quantum mode*

The Fourier transform of a classical probability distribution is known as its characteristic function, and moments of the distribution are proportional to derivatives of the characteristic function. This same procedure can be generalized to a system described by a quantum density operator: for a single bosonic mode with density operator $\hat{\rho}$, the *symmetrically ordered*[3] characteristic function is defined as

$$\chi_W(\lambda, \lambda^*) = \mathrm{tr}\{\hat{\rho} e^{\lambda \hat{a}^\dagger - \lambda^* \hat{a}}\}, \tag{19}$$

where λ is a complex variable. The symmetrically ordered moments are given by the derivative of χ_W at $\lambda = 0$, i.e.

$$\left\langle \left\{ \hat{a}^s (\hat{a}^\dagger)^r \right\}_{\mathrm{sym}} \right\rangle = \left(\frac{\partial}{\partial \lambda} \right)^r \left(-\frac{\partial}{\partial \lambda^*} \right)^s \chi_W(\lambda, \lambda^*)\big|_{\lambda=0}, \tag{20}$$

where $\{\cdot\}_{\mathrm{sym}}$ means a symmetrical product of the operators, which is an average of all ways of ordering the operators, e.g.

$$\{\hat{a}\hat{a}^\dagger\}_{\mathrm{sym}} = \frac{1}{2}\{\hat{a}\hat{a}^\dagger + \hat{a}^\dagger \hat{a}\}, \tag{21}$$

$$\left\{ \hat{a}^2 (\hat{a}^\dagger)^2 \right\}_{\mathrm{sym}} = \frac{1}{6}\left\{ (\hat{a}^\dagger)^2 \hat{a}^2 + \hat{a}^\dagger \hat{a} \hat{a}^\dagger \hat{a} + \hat{a}^\dagger \hat{a}^2 \hat{a}^\dagger + \hat{a} (\hat{a}^\dagger)^2 \hat{a} + \hat{a}\hat{a}^\dagger \hat{a}\hat{a}^\dagger + \hat{a}^2 (\hat{a}^\dagger)^2 \right\}. \tag{22}$$

The Wigner function was introduced by Wigner in 1932 [13] and is defined as a Fourier transform of the symmetrically ordered quantum characteristic function

$$W(\alpha, \alpha^*) = \frac{1}{\pi^2} \int d^2\lambda \, e^{\lambda^* \alpha - \lambda \alpha^*} \chi_W(\lambda, \lambda^*). \tag{23}$$

The Wigner function exists for any density matrix (see [11] for a proof), and in Section 2.3.7 we give the Wigner functions for several standard quantum states.

Integrating Equation (23) by parts we see that

$$\int d^2\alpha \, \alpha^s (\alpha^*)^r W(\alpha, \alpha^*) = \left(\frac{\partial}{\partial \lambda} \right)^r \left(-\frac{\partial}{\partial \lambda^*} \right)^s \chi_W(\lambda, \lambda^*)\big|_{\lambda=0}. \tag{24}$$

Thus, (from Equation (20)) the moments of the Wigner function give symmetrically ordered operator averages

$$\langle \{\hat{a}^s (\hat{a}^\dagger)^r\}_{\mathrm{sym}} \rangle = \overline{\alpha^s (\alpha^*)^r} \equiv \int d^2\alpha \, \alpha^s (\alpha^*)^r W(\alpha, \alpha^*), \tag{25}$$

where we have introduced the notation $\overline{F(\alpha, \alpha^*)}$ for averaging a function of phase-space variables $F(\alpha, \alpha^*)$ over the Wigner distribution. This suggests that the Wigner function acts like a probability distribution, indeed $W(\alpha, \alpha^*)$ is commonly referred to as a *quasi-probability* since it need not be positive. However, for many important classes of quantum states the Wigner function is either positive (or is well approximated by a positive function) and can be interpreted as a probability distribution. In these cases the average $\overline{F(\alpha, \alpha^*)}$ is equivalently calculated by statistically sampling α as a random variable from this distribution and calculating the average of $F(\alpha, \alpha^*)$ over many such samples.

Correlation functions of experimental interest are often normally ordered, requiring some tedious reordering in order to calculate them from symmetrically ordered Wigner averages. However, for a normally ordered operator in the form

$$O(\hat{a}, \hat{a}^\dagger) \equiv \sum_{n,m} c_{nm} \hat{a}^{\dagger n} \hat{a}^m, \tag{26}$$

it can be shown that the kernel, $O_W(\alpha, \alpha^*)$, for the equivalent stochastic average over the Wigner function, $\overline{O_W(\alpha, \alpha^*)} = \langle O(\hat{a}, \hat{a}^\dagger) \rangle$ is given by [14]

$$O_W(\alpha, \alpha^*) = \sum_{n,m} c_{nm} (-1)^m \left(\frac{\partial}{\partial z} + \frac{z^*}{2} \right)^n \left(\frac{\partial}{\partial z^*} + \frac{z}{2} \right)^m e^{z\alpha^* - z^*\alpha} \Big|_{z=z^*=0}, \tag{27}$$

giving, for example,

$$\langle \hat{a}^\dagger \hat{a} \rangle = \overline{|\alpha|^2} - \frac{1}{2}, \tag{28}$$

$$\langle \hat{a}^{\dagger 2} \hat{a}^2 \rangle = \overline{|\alpha|^4} - 2\overline{|\alpha|^2} + \frac{1}{2}. \tag{29}$$

An explicit form for $O_W(\alpha, \alpha^*)$ can also be found by evaluating the expression

$$O_W(\alpha, \alpha^*) = \frac{1}{2\pi} \int d^2\eta \, e^{-|\eta|^2/2} O(\alpha - \eta/2, \, \alpha^* + \eta^*/2), \tag{30}$$

which can be useful in certain circumstances, e.g. for reordering exponential operators [15]. For example, choosing $O(\hat{a}, \hat{a}^\dagger) = \hat{a}^\dagger \hat{a}$, we obtain

$$O_W(\alpha, \alpha^*) = \frac{1}{2\pi} \int d^2\eta \, e^{-|\eta|^2/2} (\alpha^* + \eta^*/2)(\alpha - \eta/2) = |\alpha|^2 - \frac{1}{2}. \tag{31}$$

2.3.2. *Operator correspondences and equations of motion*

The equation of motion for the density operator under Hamiltonian evolution is von Neumann's equation

$$i\hbar \frac{\partial \hat{\rho}}{\partial t} = \left[\hat{H}, \hat{\rho} \right], \tag{32}$$

where $\hat{H}$ is the Hamiltonian. For typical Hamiltonians the right-hand side of Equation (32) will involve products of operators and the density operator, and here we discuss how this equivalently maps onto a differential operator acting on the Wigner function. Consider, for example, the operator product $\hat{a}\hat{\rho}$. Using

$$e^{\lambda \hat{a}^\dagger - \lambda^* \hat{a}} = e^{\lambda \hat{a}^\dagger} e^{-\lambda^* \hat{a}} e^{-|\lambda|^2/2}, \tag{33}$$

(e.g. see the discussion of the Baker–Hausdorff formula in [11]) and the invariance of the trace under cyclic permutation we have (cf. Equation (19))

$$\mathrm{tr}\left\{ \hat{a}\hat{\rho} e^{\lambda \hat{a}^\dagger - \lambda^* \hat{a}} \right\} = \mathrm{tr}\left\{ \hat{\rho} e^{\lambda \hat{a}^\dagger} e^{-\lambda^* \hat{a}} e^{-|\lambda|^2/2} \hat{a} \right\} \tag{34}$$

$$= \left(\frac{1}{2}\lambda - \frac{\partial}{\partial \lambda^*} \right) \chi_W(\lambda, \, \lambda^*). \tag{35}$$

Fourier transforming Equation (35) and integrating by parts we obtain the correspondence

$$\hat{a}\hat{\rho} \leftrightarrow \left(\alpha + \frac{1}{2}\frac{\partial}{\partial \alpha^*}\right) W(\alpha, \alpha^*). \tag{36}$$

Similarly, the other correspondences are

$$\hat{a}^\dagger \hat{\rho} \leftrightarrow \left(\alpha^* - \frac{1}{2}\frac{\partial}{\partial \alpha}\right) W(\alpha, \alpha^*), \tag{37}$$

$$\hat{\rho}\hat{a} \leftrightarrow \left(\alpha - \frac{1}{2}\frac{\partial}{\partial \alpha^*}\right) W(\alpha, \alpha^*), \tag{38}$$

$$\hat{\rho}\hat{a}^\dagger \leftrightarrow \left(\alpha^* + \frac{1}{2}\frac{\partial}{\partial \alpha}\right) W(\alpha, \alpha^*). \tag{39}$$

We now have a set of mappings from operator equations involving the density matrix to a partial differential equation for the Wigner function.

Application to the damped and driven harmonic oscillator. As a demonstration of the Wigner formalism we consider the driven harmonic oscillator with Hamiltonian

$$\hat{H} = \hbar\omega \hat{a}^\dagger \hat{a} + \hbar(g\hat{a}^\dagger + g^*\hat{a}), \tag{40}$$

where ω is the oscillator frequency, and g is the driving strength. Such a Hamiltonian arises when considering a single mode of an optical resonator driven by a coherent laser field. Damping to a vacuum field outside the cavity adds additional non-Hamiltonian terms, leading to the master equation

$$\frac{\partial \hat{\rho}}{\partial t} = -\frac{i}{\hbar}[\hat{H}, \hat{\rho}] + \frac{\gamma}{2}\left(2\hat{a}\hat{\rho}\hat{a}^\dagger - \hat{a}^\dagger\hat{a}\hat{\rho} - \hat{\rho}\hat{a}^\dagger\hat{a}\right). \tag{41}$$

Using the operator correspondences (36)–(39) we obtain the equivalent equation of motion for the Wigner function

$$\frac{\partial W}{\partial t} = \left[\frac{\partial}{\partial \alpha}\left(i\omega\alpha + \frac{\gamma}{2}\alpha + ig\right) + \frac{\partial}{\partial \alpha^*}\left(-i\omega\alpha^* + \frac{\gamma}{2}\alpha^* - ig^*\right)\right] W(\alpha, \alpha^*, t) + \frac{\gamma}{2}\frac{\partial^2}{\partial \alpha \partial \alpha^*} W(\alpha, \alpha^*, t). \tag{42}$$

This evolution equation is of the form of a Fokker–Planck equation (FPE) with a drift (first derivative) term and a diffusion (second derivative) term. Here, an important tool emerges which is central to the techniques in this review: if the initial Wigner distribution $W(\alpha, \alpha^*, 0)$ is positive and our interest is in moments of the Wigner distribution at some later time (e.g. Equation (25)), then we can avoid solving the partial differential Equation (42) and instead simulate a large number of *trajectories* governed by the (Itô) stochastic differential equation (SDE)

$$\mathrm{d}\alpha = (-i\omega - \gamma/2)\alpha\,\mathrm{d}t - ig\,\mathrm{d}t + \sqrt{\gamma/2}\,\mathrm{d}w(t), \tag{43}$$

with the initial conditions $\alpha(0)$ sampled from $W(\alpha, \alpha^*, 0)$. Here the dissipative process has generated a diffusive term in the SDE which is a complex Gaussian noise satisfying $\overline{\mathrm{d}w(t)} = 0$ and $\overline{\mathrm{d}w^*(t)\mathrm{d}w(t)} = \mathrm{d}t$. The justification for this procedure is the standard mapping of a FPE onto a SDE [16]. In the case where dissipation is absent, the SDE simplifies to an ordinary differential equation. This is the situation for much of the work described in this review, but the reasons for the simplification to an ordinary differential equation of motion are more subtle and are discussed in detail in Section 2.3.6. The SDE (43) also contains the essential technical elements of the phase-space mapping required for deriving the SPGPE described in Section 5. A more complete discussion of the correspondence between SDEs and FPEs is presented in Appendix C. Moving to spatially continuous, modally finite-dimensional field theories adds some further complexities which are addressed in the following sections.

2.3.3. *Adaption to quantum field theory in the c-field region*

The extension from the single-mode case to quantum field theory is accomplished using the projected functional generalization of the single-mode formalism. As there are only a finite number of modes, the theory can be generalized in a form which involves minimal additional calculus. For a system with M modes in the c-field region, we define the vector of mode amplitudes $\boldsymbol{\alpha} = [\alpha_0, \alpha_1, \ldots, \alpha_{M-1}]^{\mathrm{T}}$ and the notation

$$\int d^2\boldsymbol{\alpha} \equiv \prod_{n\in\mathbf{C}} \int d^2\alpha_n. \tag{44}$$

The multimode Wigner function is then given by

$$W_{\mathbf{C}}(\boldsymbol{\alpha}, \boldsymbol{\alpha}^*) = \int \frac{d^2\boldsymbol{\lambda}}{\pi^{2M}} \exp\left(\boldsymbol{\lambda}^\dagger \boldsymbol{\alpha} - \boldsymbol{\alpha}^\dagger \boldsymbol{\lambda}\right) \chi_W(\boldsymbol{\lambda}, \boldsymbol{\lambda}^*), \tag{45}$$

where $\boldsymbol{\alpha}^\dagger = (\boldsymbol{\alpha}^*)^T$, and χ_W is the characteristic function for the c-field region density operator, $\hat{\rho}_{\mathbf{C}}$. Moments of the Wigner distribution give symmetrically ordered operator averages, for example

$$\int d^2\boldsymbol{\alpha}\, |\alpha_q|^2 W_{\mathbf{C}}(\boldsymbol{\alpha}, \boldsymbol{\alpha}^*) = \left\langle \frac{\hat{a}_q^\dagger \hat{a}_q + \hat{a}_q \hat{a}_q^\dagger}{2} \right\rangle. \tag{46}$$

Introducing the c-number c-field (cf. Equation (13))

$$\psi_{\mathbf{C}}(\mathbf{x}) = \sum_{n\in\mathbf{C}} \alpha_n \phi_n(\mathbf{x}), \tag{47}$$

the field density average corresponding to Equation (46) is

$$\int d^2\boldsymbol{\alpha}\, |\psi_{\mathbf{C}}(\mathbf{x})|^2 W_{\mathbf{C}}(\boldsymbol{\alpha}, \boldsymbol{\alpha}^*) = \left\langle \frac{\hat{\psi}_{\mathbf{C}}^\dagger(\mathbf{x})\hat{\psi}_{\mathbf{C}}(\mathbf{x}) + \hat{\psi}_{\mathbf{C}}(\mathbf{x})\hat{\psi}_{\mathbf{C}}^\dagger(\mathbf{x})}{2} \right\rangle, \tag{48}$$

$$= \left\langle \hat{\psi}_{\mathbf{C}}^\dagger(\mathbf{x})\hat{\psi}_{\mathbf{C}}(\mathbf{x}) \right\rangle + \frac{\delta_{\mathbf{C}}(\mathbf{x}, \mathbf{x})}{2}. \tag{49}$$

The contribution from the projector in Equation (49) represents a central result of the Wigner representation of quantum field theory. Physics beyond mean-field theory arises in

the truncated Wigner method because of vacuum noise evident in the commutator term $\delta_{\mathbf{C}}(\mathbf{x},\mathbf{x})$ (17), which accounts for half a quantum per mode of noise present in the theory. This noise mimics the role of vacuum fluctuations, but would render the theory ultraviolet divergent if all physically allowed modes were included. However, the projection into the c-field region involves a finite number of basis functions, so that in this situation the term is a well-defined finite contribution to the stochastic average.

2.3.4. *Functional derivative notation*

There is a useful connection between projectors and functional calculus that greatly simplifies multimode calculations while still including all of the necessary projectors into low-energy modes. We define the projected derivative operators as

$$\frac{\bar{\delta}}{\bar{\delta}\psi_{\mathbf{C}}(\mathbf{x})} \equiv \sum_{n\in\mathbf{C}} \phi_n^*(\mathbf{x}) \frac{\partial}{\partial \alpha_n}, \tag{50}$$

$$\frac{\bar{\delta}}{\bar{\delta}\psi_{\mathbf{C}}^*(\mathbf{x})} \equiv \sum_{n\in\mathbf{C}} \phi_n(\mathbf{x}) \frac{\partial}{\partial \alpha_n^*}. \tag{51}$$

2.3.5. *Operator correspondences*

Using the projected functional derivatives, one then finds functional operator correspondences between the density operator, $\hat{\rho}_{\mathbf{C}}$, and the Wigner function [11]

$$\hat{\psi}_{\mathbf{C}}(\mathbf{x})\hat{\rho}_{\mathbf{C}} \longleftrightarrow \left(\psi_{\mathbf{C}}(\mathbf{x}) + \frac{1}{2}\frac{\bar{\delta}}{\bar{\delta}\psi_{\mathbf{C}}^*(\mathbf{x})}\right) W_{\mathbf{C}}, \tag{52}$$

$$\hat{\psi}_{\mathbf{C}}^\dagger(\mathbf{x})\hat{\rho}_{\mathbf{C}} \longleftrightarrow \left(\psi_{\mathbf{C}}^*(\mathbf{x}) - \frac{1}{2}\frac{\bar{\delta}}{\bar{\delta}\psi_{\mathbf{C}}(\mathbf{x})}\right) W_{\mathbf{C}}, \tag{53}$$

$$\hat{\rho}_{\mathbf{C}}\hat{\psi}_{\mathbf{C}}(\mathbf{x}) \longleftrightarrow \left(\psi_{\mathbf{C}}(\mathbf{x}) - \frac{1}{2}\frac{\bar{\delta}}{\bar{\delta}\psi_{\mathbf{C}}^*(\mathbf{x})}\right) W_{\mathbf{C}}, \tag{54}$$

$$\hat{\rho}_{\mathbf{C}}\hat{\psi}_{\mathbf{C}}^\dagger(\mathbf{x}) \longleftrightarrow \left(\psi_{\mathbf{C}}^*(\mathbf{x}) + \frac{1}{2}\frac{\bar{\delta}}{\bar{\delta}\psi_{\mathbf{C}}(\mathbf{x})}\right) W_{\mathbf{C}}, \tag{55}$$

which are used to map the equation of motion for the density operator to an equation of motion for $W_{\mathbf{C}}$.

2.3.6. *Truncated Wigner approximation*

From Equation (5) we see that the time development of $\hat{\psi}_{\mathbf{C}}$ in isolation[4] is governed by the Hamiltonian

$$\hat{H}_{\mathbf{C}} = \int d^3\mathbf{x}\, \hat{\psi}_{\mathbf{C}}^\dagger(\mathbf{x}) H_{\mathrm{sp}} \hat{\psi}_{\mathbf{C}}(\mathbf{x}) + \frac{u}{2}\int d^3\mathbf{x}\, \hat{\psi}_{\mathbf{C}}^\dagger(\mathbf{x})\hat{\psi}_{\mathbf{C}}^\dagger(\mathbf{x})\hat{\psi}_{\mathbf{C}}(\mathbf{x})\hat{\psi}_{\mathbf{C}}(\mathbf{x}). \tag{56}$$

The equation of motion for the density operator in **C** is then von Neumann's equation

$$i\hbar\frac{\partial\hat{\rho}_{\mathbf{C}}(t)}{\partial t}=[\hat{H}_{\mathbf{C}},\hat{\rho}_{\mathbf{C}}(t)]. \tag{57}$$

Using the operator correspondences (52)–(55), the Hamiltonian (56) generates the time evolution equation

$$\begin{aligned}\left.\frac{\partial W_{\mathbf{C}}}{\partial t}\right|_{\hat{H}_{\mathbf{C}}}=\int d^3\mathbf{x}\Bigg\{&\frac{iu}{4\hbar}\frac{\bar{\delta}}{\bar{\delta}\psi_{\mathbf{C}}(\mathbf{x})\bar{\delta}\psi^*_{\mathbf{C}}(\mathbf{x})}\psi^*_{\mathbf{C}}(\mathbf{x})\frac{\bar{\delta}}{\bar{\delta}\psi^*_{\mathbf{C}}(\mathbf{x})}+\text{h.c.}\\&\frac{i}{\hbar}\frac{\bar{\delta}}{\bar{\delta}\psi_{\mathbf{C}}(\mathbf{x})}(H_{\rm sp}+u[|\psi_{\mathbf{C}}(\mathbf{x})|^2-\delta_{\mathbf{C}}(\mathbf{x},\mathbf{x})])\psi_{\mathbf{C}}(\mathbf{x})+\text{h.c.}\Bigg\}W_{\mathbf{C}},\end{aligned} \tag{58}$$

where h.c. represents the Hermitian conjugate. Equation (58) as it stands is very difficult to solve. However, if we are able to neglect the first line of right-hand side terms, i.e. those containing third-order derivatives, then progress can be made. This approximation, which is referred to as the *truncated Wigner approximation* (TWA), is valid over a wide regime for the quantum degenerate gas. The resulting description is also obtained formally in the classical limit which we describe below. (We discuss the basic validity conditions for this approximation further in Section 2.3.9.) As discussed in Appendix C, a mapping to ordinary SDEs is not possible for Equation (58). However, when making the TWA, the Wigner function evolution takes the form of a FPE with drift but no diffusion terms, i.e.

$$\left.\frac{\partial W_{\mathbf{C}}}{\partial t}\right|_{\hat{H}_{\mathbf{C}}}\approx\int d^3\mathbf{x}\left\{\frac{i}{\hbar}\frac{\bar{\delta}}{\bar{\delta}\psi_{\mathbf{C}}(\mathbf{x})}\Big(H_{\rm sp}+u[|\psi_{\mathbf{C}}(\mathbf{x})|^2-\delta_{\mathbf{C}}(\mathbf{x},\mathbf{x})]\Big)\psi_{\mathbf{C}}(\mathbf{x})+\text{h.c.}\right\}W_{\mathbf{C}}. \tag{59}$$

The Fokker–Planck evolution can be equivalently mapped to a stochastic partial differential equation [16] that describes the trajectory of a single realization of the field $\psi_{\mathbf{C}}(\mathbf{x})$, which we refer to as the TWPGPE

$$i\hbar\frac{\partial\psi_{\mathbf{C}}(\mathbf{x})}{\partial t}=\mathcal{P}_{\mathbf{C}}\Big\{\Big(H_{\rm sp}+u[|\psi_{\mathbf{C}}(\mathbf{x})|^2-\delta_{\mathbf{C}}(\mathbf{x},\mathbf{x})]\Big)\psi_{\mathbf{C}}(\mathbf{x})\Big\}. \tag{60}$$

The lack of a diffusion term in (59) means that no explicit noise term appears in the TWPGPE, however, as we discuss further in Section 2.3.7 the initial conditions are stochastic and need to be appropriately sampled from the initial Wigner function. We remark that the equation of motion (59) is also known as a Liouville equation. A formal property of the Liouville equation is that the distribution function is constant along any trajectory in phase space. This can be seen by applying the method of characteristics to (59), which shows that, within the TWA, the Wigner function is constant along classical trajectories given by (60).

Classical limit. While we consider the validity conditions for the truncation in Section 2.3.9, here we show that the truncation is exact in the *classical limit*, which we define as

$$N_{\mathbf{C}}\to\infty,\quad u\to 0,\quad uN_{\mathbf{C}}=\text{constant}, \tag{61}$$

where $N_{\mathbf{C}}$ is the number of c-field region particles

$$N_{\mathbf{C}}=\int d^3\mathbf{x}|\psi_{\mathbf{C}}(\mathbf{x})|^2\quad\text{(classical limit)}. \tag{62}$$

This expression for $N_{\mathbf{C}}$ is only valid in the classical limit, and the general case, obtained from Equation (49), is $N_{\mathbf{C}} = \int d^3\mathbf{x}[|\psi_{\mathbf{C}}(\mathbf{x})|^2 - \delta_{\mathbf{C}}(\mathbf{x},\mathbf{x})/2]$. The integral $\int d^3\mathbf{x}\delta_{\mathbf{C}}(\mathbf{x},\mathbf{x})/2 = M/2$, representing the half quantum per mode vacuum noise included in the Wigner description.

Renormalizing the c-field according to $\phi_{\mathbf{C}} = \sqrt{N_{\mathbf{C}}}\psi_{\mathbf{C}}$, Equation (58) becomes

$$\left.\frac{\partial W_{\mathbf{C}}}{\partial t}\right|_{\hat{H}_{\mathbf{C}}} = \int d^3\mathbf{x}\Bigg\{\frac{iu}{4\hbar N_{\mathbf{C}}}\frac{\bar{\delta}}{\bar{\delta}\phi_{\mathbf{C}}(\mathbf{x})\bar{\delta}\phi^*_{\mathbf{C}}(\mathbf{x})}\phi^*_{\mathbf{C}}(\mathbf{x})\frac{\bar{\delta}}{\bar{\delta}\phi^*_{\mathbf{C}}(\mathbf{x})} + \text{h.c.} - \frac{i}{\hbar}\frac{\bar{\delta}}{\bar{\delta}\phi_{\mathbf{C}}(\mathbf{x})}\left(H_{\text{sp}} + uN_{\mathbf{C}}|\phi_{\mathbf{C}}(\mathbf{x})|^2\right)\phi_{\mathbf{C}}(\mathbf{x}) + \text{h.c.}\Bigg\}W_{\mathbf{C}}. \tag{63}$$

In the classical limit we have $u/N_{\mathbf{C}} \to 0$, so that the third-order derivatives vanish in Equation (63), and the TWPGPE (60) is the asymptotically exact equation of motion for the system. However, stochastic initial conditions are still present, reflecting quantum or thermal fluctuations, or uncertainties in the initial data of the problem.

A purely *deterministic* classical description is recovered when the initial state approaches a delta function in phase space which is precisely the limit obtained for a zero-temperature BEC in a coherent state. For $N_{\mathbf{C}}$ atoms in a single mode coherent state with mode function $\xi_0(\mathbf{x})$, the renormalized field can be written as $\phi_{\mathbf{C}}(\mathbf{x}) = \alpha\xi_0(\mathbf{x})$, with phase-space distribution

$$W(\alpha,\alpha^*) = \frac{2N_{\mathbf{C}}}{\pi}\exp\left(-2N_{\mathbf{C}}\left|\alpha - \frac{\alpha_0}{\sqrt{N_{\mathbf{C}}}}\right|^2\right), \tag{64}$$

where $|\alpha_0|^2 = N_{\mathbf{C}}$. In the classical limit $W(\alpha,\alpha^*) \to \delta^{(2)}(\alpha - 1)$, giving the TWPGPE for the system dynamics with non-stochastic initial conditions. In general, thermal fluctuations will be present even in the classical limit, and the problem remains stochastic, subject to deterministic evolution. We note that in the classical limit vacuum noise is unimportant, but it can play an important role in BEC physics where $N_{\mathbf{C}} \sim 10^3$–10^9. Indeed, the effect of zero-point fluctuations can be rather striking and even the dominant effect in certain circumstances. An important example is given by the dynamics of condensate collisions, described in Section 4.2.

Classical mechanics treatment. For future reference, we note that replacing the field operator by the classical field $\psi_{\mathbf{C}}$ in Hamiltonian (56) yields the Hamiltonian

$$H_{\mathbf{C}} = \int d^3\mathbf{x}\psi^*_{\mathbf{C}}(\mathbf{x})H_{\text{sp}}\psi_{\mathbf{C}}(\mathbf{x}) + \frac{u}{2}\int d^3\mathbf{x}|\psi_{\mathbf{C}}(\mathbf{x})|^4, \tag{65}$$

which we also refer to as the energy functional for the field $\psi_{\mathbf{C}}$. The classical equation of motion can then be found by defining the *Poisson bracket* $\{F, G\}$ for any two functionals F and G of the classical field $\psi_{\mathbf{C}}(\mathbf{x})$ as

$$\{F,G\} = \int d^3\mathbf{x}\frac{\bar{\delta}F}{\bar{\delta}\psi_{\mathbf{C}}(\mathbf{x})}\frac{\bar{\delta}G}{\bar{\delta}\psi^*_{\mathbf{C}}(\mathbf{x})} - \frac{\bar{\delta}F}{\bar{\delta}\psi^*_{\mathbf{C}}(\mathbf{x})}\frac{\bar{\delta}G}{\bar{\delta}\psi_{\mathbf{C}}(\mathbf{x})}. \tag{66}$$

The equation of motion is then found as

$$i\hbar\frac{\partial\psi_{\mathbf{C}}(\mathbf{x})}{\partial t} = \{\psi_{\mathbf{C}}(\mathbf{x}), H_{\mathbf{C}}\} = \frac{\bar{\delta}H_{\mathbf{C}}}{\bar{\delta}\psi^*_{\mathbf{C}}(\mathbf{x})}, \tag{67}$$

which yields the PGPE

$$i\hbar\frac{\partial\psi_{\mathbf{C}}(\mathbf{x})}{\partial t}=\mathcal{P}_{\mathbf{C}}\left\{\left(H_{\rm sp}+u|\psi_{\mathbf{C}}(\mathbf{x})|^2\right)\psi_{\mathbf{C}}(\mathbf{x})\right\}, \tag{68}$$

as the classical equation of motion of the system. This equation is equivalent to the TWPGPE (60) in the classical limit where the $\delta_{\mathbf{C}}$ term can be neglected. The theory can be cast in standard Hamiltonian form by introducing the canonical position and momentum variables

$$Q_n=1/\sqrt{2\epsilon_n}(\alpha_n+\alpha_n^*), \tag{69}$$

$$P_n=i\sqrt{\epsilon_n/2}(\alpha_n^*-\alpha_n), \tag{70}$$

where the α_n are the basis amplitudes of $\psi_{\mathbf{C}}(\mathbf{x})$ (see (47)) and ϵ_n are the energies of the modes comprising the basis. The Poisson bracket then takes the Hamiltonian form and any function $F(P_n, Q_n, t)$ obeys the equation of motion

$$\frac{dF}{dt}=\frac{1}{\hbar}\sum_n\left(\frac{\partial F}{\partial Q_n}\frac{\partial H_{\mathbf{C}}}{\partial P_n}-\frac{\partial F}{\partial P_n}\frac{\partial H_{\mathbf{C}}}{\partial Q_n}\right)+\frac{\partial F}{\partial t}. \tag{71}$$

We emphasize that the Hamiltonian classical mechanics formulation is not only recovered in the continuum limit, but holds generally as a consequence of including the projection operator formally in the definition of the classical field $\psi_{\mathbf{C}}(\mathbf{x})$. This Hamiltonian property is used in Section 3.2.5 to determine microcanonical thermodynamic quantities of the c-field.

2.3.7. *Sampling the Wigner distribution*

We have shown that by making the TWA, simulations of ultra-cold Bose gas dynamics under the Hamiltonian $\hat{H}_{\mathbf{C}}$ (56) are reduced to simulations of the PGPE (or more accurately the TWPGPE (60)) for an ensemble of samples of the initial state of the system. The equation of motion is quite easy to solve, but sampling the Wigner distribution for a general many-body system is difficult. However, sometimes this sampling issue can be avoided, e.g., in the PGPE method a random initial field can be used and allowed to thermalize by evolution (see Section 3.2.2).

Bogoliubov formalism. Here, our basic aim is to present a procedure for sampling the Wigner distribution for a cold ($T\ll T_{\rm c}$) Bose condensed cloud in thermal equilibrium. In this regime, the Bogoliubov method provides an appropriate many-body description of the system, provided that the number of non-condensate particles, $N_{\rm ex}\equiv N_{\mathbf{C}}-N_0$, satisfies $N_{\rm ex}\ll N_{\mathbf{C}}$. We briefly review the Bogoliubov formalism, and refer to the interested reader [4,17–22] for a more complete discussion. The basic Bogoliubov approach is to expand the field operator in the form

$$\hat{\psi}_{\mathbf{C}}(\mathbf{x})=\frac{\hat{a}_0}{\sqrt{N_0}}\xi_0(\mathbf{x})+\sum_{j>0}\left[u_j(\mathbf{x})\hat{b}_j+v_j^*(\mathbf{x})\hat{b}_j^\dagger\right], \tag{72}$$

where ξ_0 is the condensate mode normalized to N_0 atoms, $\{u_j(\mathbf{x}), v_j(\mathbf{x})\}$ are the quasiparticle amplitudes, and $\{\hat{b}_j, \hat{b}_j^\dagger\}$ are quasiparticle operators that satisfy the usual Bose

commutation relations. The standard procedure is to take the condensate mode as a solution to the time-independent GPE

$$\mu\xi_0(\mathbf{x}) = H_{\rm sp}\xi_0(\mathbf{x}) + u\left|\xi_0(\mathbf{x})\right|^2\xi_0(\mathbf{x}), \tag{73}$$

where μ is the chemical potential, and then determine $\{U_j, V_j\}$ and the quasi-particle eigenvalues ϵ_j^B from the Bogoliubov–de Gennes equations

$$\epsilon_j^B U_j(\mathbf{x}) = \left[H_{\rm sp} + 2u\left|\xi_0(\mathbf{x})\right|^2 - \mu\right]U_j(\mathbf{x}) + u\xi_0(\mathbf{x})^2 V_j(\mathbf{x}), \tag{74}$$

$$-\epsilon_j^B V_j(\mathbf{x}) = \left[H_{\rm sp} + 2u\left|\xi_0(\mathbf{x})\right|^2 - \mu\right]V_j(\mathbf{x}) + u\xi_0^*(\mathbf{x})^2 U_j(\mathbf{x}). \tag{75}$$

The expansion in Equation (72) diagonalizes the many-body Hamiltonian (56) to quadratic order in the quasiparticle operators, which is adequate in the regime of small condensate depletion, so that the quasiparticle levels are thermally occupied according to

$$\langle\hat{b}_i^\dagger\hat{b}_j\rangle = \delta_{ij}\frac{1}{e^{\epsilon_j^B/k_{\rm B}T} - 1}, \tag{76}$$

$$= \delta_{ij}\bar{n}_j. \tag{77}$$

We note that the Bogoliubov modes, $\{U_j(\mathbf{x}), V_j(\mathbf{x})\}$, are in general not orthogonal to the condensate. Even though the correct eigenfrequencies are obtained, orthogonality is automatic only for the special case of a uniform system. The correct modes for the expansion of the field operator (72) can be recovered from (74) and (75) by taking the projection orthogonal to the condensate [23]. Defining the projector

$$\mathcal{P}_0\psi(\mathbf{x}) = \psi(\mathbf{x}) - N_0^{-1}\xi_0(\mathbf{x})\int d^3\mathbf{x}'\xi_0^*(\mathbf{x}')\psi(\mathbf{x}'), \tag{78}$$

the orthogonal modes are given by $\{u_i(\mathbf{x}), v_i(\mathbf{x})\} = \{\mathcal{P}_0 U_i(\mathbf{x}), (\mathcal{P}_0^* V_i^*(\mathbf{x}))^*\}$.

Wigner sampling of the Bogoliubov state. By introducing the random variables α_0 and $\boldsymbol{\beta}$ (an $M-1$ element vector) in place of the operators $\hat{a}_0$ and $\{\hat{b}_j\}$, respectively, the Wigner distribution for the Bogoliubov state is appropriately sampled as the stochastic c-field

$$\psi_{\mathbf{C}}(\mathbf{x}) = \frac{\alpha_0}{\sqrt{N_0}}\xi_0(\mathbf{x}) + \sum_{j>0}\left[u_j(\mathbf{x})\beta_j + v_j^*(\mathbf{x})\beta_j^*\right]. \tag{79}$$

In the Bogoliubov theory outlined above, the condensate and quasiparticle occupations are uncorrelated, i.e. the Wigner distribution is of the separable form $W_{\mathbf{C}} = W_0(\alpha_0, \alpha_0^*)W_{\rm qp}(\boldsymbol{\beta}, \boldsymbol{\beta}^*)$, and in the following paragraphs we discuss how these can be independently sampled. We note that within a number conserving Bogoliubov approach additional correlations between the condensate and quasiparticles arise [10,24], providing a better description of the low temperature many-body state of the gas.

Condensate mode: coherent state. To a good approximation the condensate can be regarded as being in a coherent state, for which the Wigner function is

$$W_0(\alpha, \alpha^*) = \frac{2}{\pi}\exp\left(-2|\alpha - \alpha_0|^2\right), \tag{80}$$

where $N_0 = |\alpha_0|^2$. For large condensate occupation the finite width of W_0 can be neglected and for all samples of the condensate amplitude we can take $\alpha_0 \approx \sqrt{N_0}$.

Quasiparticle modes: thermalized states. The quasiparticle levels are thermalized modes, with a Wigner distribution of the form of a product of uncorrelated Gaussian quasi-probability distributions, i.e.

$$W_{\rm qp}(\boldsymbol{\beta}, \boldsymbol{\beta}^*) = \prod_{j>0} W_j(\beta_j, \beta_j^*), \tag{81}$$

$$W_j(\beta_j, \beta_j^*) = \frac{2}{\pi} \tanh\left(\frac{\epsilon_j^B}{k_{\rm B}T}\right) \exp\left[-2|\beta_j|^2 \tanh\left(\frac{\epsilon_j^B}{k_{\rm B}T}\right)\right]. \tag{82}$$

This distribution is sampled by the Gaussian complex random variables, $\{\beta_j\}$, with the properties

$$\overline{\beta_j} = \overline{\beta_i \beta_j} = 0, \tag{83}$$

$$\overline{\beta_i^* \beta_j} = \delta_{ij}\left(\bar{n}_j + \frac{1}{2}\right). \tag{84}$$

In practice, these variables can be generated as

$$\beta_j = \sqrt{\bar{n}_j + 1/2}\left(\frac{x_j + i y_j}{\sqrt{2}}\right), \tag{85}$$

where x_j, y_j are normally distributed Gaussian random variables with mean zero and unit variance. Sampling the field in this way, we recover the correct symmetrically ordered moments, e.g.

$$\overline{\psi_{\mathbf{C}}(\mathbf{x})} = \langle \hat{\psi}_{\mathbf{C}}(\mathbf{x}) \rangle, \tag{86}$$

$$= \xi_0(\mathbf{x}), \tag{87}$$

$$\overline{|\psi_{\mathbf{C}}(\mathbf{x})|^2} = \langle \{\hat{\psi}_{\mathbf{C}}^\dagger(\mathbf{x}) \hat{\psi}_{\mathbf{C}}(\mathbf{x})\}_{\rm sym} \rangle, \tag{88}$$

$$= |\xi_0(\mathbf{x})|^2 + \sum_{j>0} \frac{1}{2} (\langle \hat{\beta}_j^\dagger \hat{\beta}_j \rangle + \langle \hat{\beta}_j \hat{\beta}_j^\dagger \rangle)(|u_j(\mathbf{x})|^2 + |v_j(\mathbf{x})|^2). \tag{89}$$

Vacuum occupation. We note that even in the zero-temperature limit, where $\bar{n}_j \to 0$, the random variables β_j have the finite variance $\overline{|\beta_j|^2} = 1/2$, i.e. each mode of the system has on average half an atom of *vacuum noise*, necessary to ensure the symmetrically ordered interpretation of Wigner moments. Thus, an attribute of the Wigner method is that for a simulation with M modes, $M/2$ virtual particles (i.e. vacuum noise) are included in the field in addition to the $N_{\mathbf{C}}$ real particles.

2.3.8. *Alternative methods for sampling the Wigner distribution*

Efficient sampling of a number-conserving Bogoliubov state. Sinatra *et al.* have shown how a number-conserving version of the Bogoliubov formalism can be implemented via

a Brownian motion simulation. This approach, developed in [10,24,25], has the advantage that it does not require diagonalization of the Bogoliubov–de Gennes equations.

Approximate ground-state construction. For a nearly pure condensate the appropriate ground-state of the system is sampled as the $T=0$ limit of expression (79). However, for many non-equilibrium scenarios, the quasiparticle properties of the low-energy modes are unimportant, and the vacuum noise can be added in any basis orthonormal to the condensate. That is

$$\psi_{\mathbf{C}}(\mathbf{x}) = \frac{\alpha_0}{\sqrt{N_0}}\xi_0(\mathbf{x}) + \sum_j \bar{\xi}_j(\mathbf{x})\alpha_j, \tag{90}$$

where $\{\bar{\xi}_j(\mathbf{x})\}$ is an orthonormal basis. The condensate amplitude, α_0, is sampled as described below Equation (80), and the other mode amplitudes are sampled as Gaussian random variables with $\overline{\alpha_j^*\alpha_j} = \delta_{ij}/2$. This type of construction is useful in collision experiments where the vacuum fluctuation of the high-energy modes drive scattering events.

Ideal gas ground state. In the absence of interactions, the ground state Wigner function can be sampled as

$$\psi_{\mathbf{C}}(\mathbf{x}) = \sum_j \phi_j(\mathbf{x})\alpha_j, \tag{91}$$

where $\phi_n(\mathbf{x})$ are the single particle basis states and the α are sampled according to $\alpha_0 = \sqrt{N_{\mathbf{C}}}$ and $\overline{\alpha_i^*\alpha_j} = \delta_{ij}/2$, for $i, j > 0$.

Ideal gas high-temperature state. For temperatures above T_c expansion (91) also suffices to describe the thermalized state of the system but with all α_j sampled as Gaussian random variables with

$$\overline{\alpha_i^*\alpha_j} = \delta_{ij}\left(\bar{n}_{\mathrm{BE}}(\epsilon_j) + \frac{1}{2}\right), \tag{92}$$

where $\bar{n}_{\mathrm{BE}}(\epsilon_j) = \{\exp[(\epsilon_j - \mu)/k_{\mathrm{B}}T] - 1\}^{-1}$ is the Bose–Einstein distribution.

More general condensate states. It is possible to consider more general states for the condensate, e.g. the number state $|N_0\rangle$, which has the Wigner function

$$W_0(\alpha, \alpha^*) = \frac{2(-1)^{N_0}}{\pi}\exp\left(-2|\alpha|^2\right)\mathrm{L}_{N_0}(4|\alpha|^2), \tag{93}$$

where $\mathrm{L}_n(x)$ is the Laguerre polynomial. The number state Wigner function for $N_0 = 10$ is shown in Figure 3(c). It is non-positive-definite, and is highly oscillatory for large numbers which makes exact stochastic sampling difficult. However, for large N_0 the radial distribution is well approximated by a delta function [26]. A Gaussian approximation is thus suitable in this regime and a method for sampling the number state Wigner function has been developed and shown to reproduce all moments with error of approximately $O(1/N_0)$ (see [27]). However, more simply we can take $\alpha_0 \approx \sqrt{N_0}e^{i\theta}$, where θ is a uniformly distributed random phase, $\theta \in [0, 2\pi]$. Sampling θ this way preserves the $U(1)$ symmetry of the system.

Other quantum states, such as squeezed states (see Figure 3(b)), and crescent states can be sampled (see, e.g., [28]) to investigate their influence on the many-body dynamics.

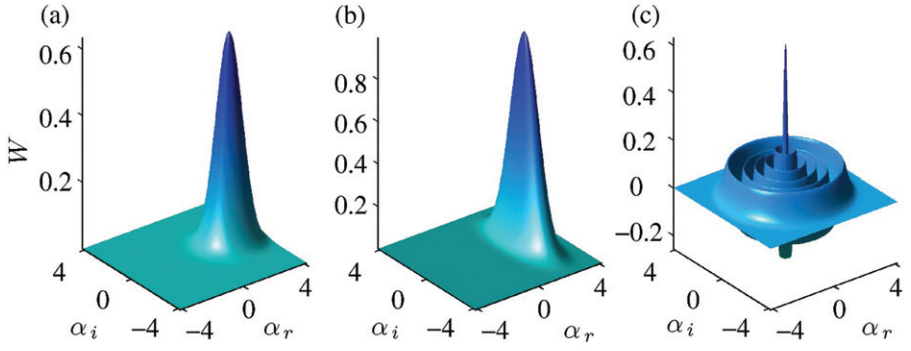

Figure 3. Some possible Wigner functions for the condensate mode of a small BEC: (a) coherent state; (b) squeezed state; and (c) number state. Wigner distribution for $\langle N_0 \rangle = 10$ atoms and $\alpha = \alpha_r + i\alpha_i$.

Adiabatic mapping. In [29], Polkovnikov and Wang sampled the Wigner function of an ideal Bose gas in an optical lattice at $T = 0$. In the ideal case the bare modes, $\{\phi_j(\mathbf{x})\}$, form the appropriate basis and the Wigner function can be sampled as discussed below Equation (91). The interactions are slowly ramped up to the desired value to generate samples of the interacting system (justified by the quantum adiabatic theorem).

2.3.9. *Validity criteria for the truncated Wigner method*

The only approximation made in deriving the TWPGPE has been the neglect of third-order derivatives in the evolution equation for the multimode Wigner function (58). The complete set of validity conditions for the truncation is still the subject of current research. Polkovnikov and Gritsev, who derived the TWA using a path integral method, have obtained expressions for the next order corrections in quantum scattering processes [15,30] that can be used to assess the validity of any simulation. This approach represents a fundamental advance in the formulation and application of the truncated Wigner method: it promotes the truncated Wigner method to a *controlled* approximation theory since corrections to the TWA can, at least in principle, be calculated explicitly. In practice, evaluating the corrections is a challenging task for large multi-mode problems, and applications have thus far been restricted to discrete lattice systems where the relative strength of interactions to linear system evolution is straightforwardly defined. We also make note of comparisons that have been made between the TWA and exact results [31–33] to characterize the limitations of the approach for quantum optical systems.

Several practical conditions for ensuring the reliability of truncated Wigner simulations in a variety of regimes have emerged in the literature, and we summarize these here. Broadly these conditions fall into two categories: (i) those required to ensure consistency of short-time dynamics (relative to the thermalization timescale); and (ii) those required for simulations over longer timescales where the system may thermalize.

Short-time evolution: quantum dynamics. The strict condition of validity of the TWPGPE is that all modes of the c-field region are highly occupied, so that the classical limit discussed in Section 2.3.6 is approached. In general, this condition is rather restrictive, especially for systems well below the critical temperature.

Another criterion has been derived by Norrie *et al.* [34] for factorizable Gaussian states. In particular, Norrie *et al.* considered the class of states with a Wigner function of the form

$$W_{\mathbf{C}}(\boldsymbol{\alpha}, \boldsymbol{\alpha}^*) = \prod_j \frac{\Gamma_j}{\pi} \exp\left(-\Gamma_j |\alpha_j - \alpha_{j_0}|^2\right), \tag{94}$$

where the random variable α_j, with corresponding orthonormal basis mode $\xi_j(\mathbf{x})$, has mean value α_{j0}, and variance Γ_j^{-1}. A sufficient condition for the validity of the TWPGPE for these states is

$$\left| \langle \hat{\psi}_{\mathbf{C}}^\dagger(\mathbf{x}) \hat{\psi}_{\mathbf{C}}(\mathbf{x}) \rangle - \frac{1}{2} \delta_{\mathbf{C}}(\mathbf{x}, \mathbf{x}) \right| \gg \sum_j \frac{\Gamma_j}{4} |\xi_j(\mathbf{x})|^2, \tag{95}$$

i.e. the system must have sufficiently high density in position space. In general, this condition is much more readily satisfied than the condition of high mode occupancy.

Sinatra *et al.* [10] have made detailed comparisons of the truncated Wigner and time-dependent Bogoliubov approaches for a uniform Bose condensate in the regime $T \ll T_c$, where the non-condensate population is much smaller than the condensate. They find that the truncated Wigner predictions become inaccurate if the quantum noise sampled in the initial condition dominates the number of particles in the system, i.e. the condition for validity is

$$\frac{M}{2} \ll N_{\mathbf{C}}. \tag{96}$$

We note that this condition can be rewritten in terms of the spatial density as $n(\mathbf{x})\Delta V \gg 1$, where $n(\mathbf{x}) = N_{\mathbf{C}}/V$ and $\Delta V = V/M$. Since $\delta_{\mathbf{C}}(\mathbf{x}, \mathbf{x}) = 1/\Delta V$ and $|\xi_j|^2 = 1/V$ for the uniform gas, we see that results (96) and (95) are equivalent for this system.

***Long-time evolution*: *Thermalization*.** As discussed earlier, when modelling a system of M modes an additional half quantum per mode of noise is added on average to the initial condition. This introduces $M/2$ virtual particles into the TWPGPE simulation which should be subtracted to recover the correct operator averages. However, under evolution these virtual particles may thermalize, and change the equilibrium properties of the system.

Sinatra *et al.* [10] have proposed the condition

$$|T - T_{\text{class}}| \ll T, \tag{97}$$

to ensure the long-time validity of a truncated Wigner calculation for a system, where T is the initial temperature of the system, and T_{class} is the temperature once the noise has thermalized. In practice, they found that Equation (97) is best ensured by limiting the number of modes in the numerical calculation, and that an acceptable description is obtained if the largest single-particle (quasiparticle) energy in the calculation is no more than a few $k_B T$.

***Interactions and dimensionality*.** It is clear that the conditions listed above cannot be considered complete as they do not explicitly involve interactions or dimensionality. In regimes where interactions dominate the system can evolve into a strongly correlated state. Important examples for ultra-cold atoms are the Mott-insulating and Bose-glass states that emerge when a system of repulsive bosonic atoms is confined in a deep optical

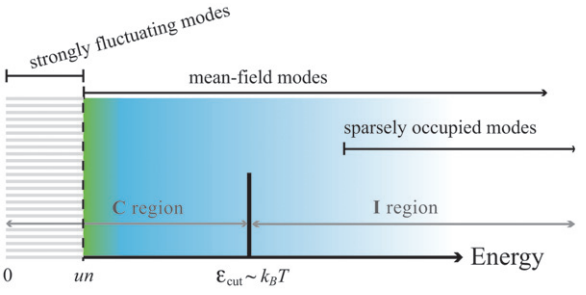

Figure 4. Schematic view of the modes in a critical system showing the appropriate choice of $\epsilon_{\rm cut}$.

lattice [35,36]. Generally speaking the TWA does not provide a good representation for such strongly correlated systems.

Another regime in which interactions play an important role is in the critical region where the system undergoes strong fluctuations. These *critical fluctuations* are classical in nature and thus amenable to the truncated Wigner treatment, however care is needed in choosing **C** to describe this regime. Typically strong fluctuations occur in the infrared modes up to the energy scale un where n is the density, above which the modes are well-described by mean-field theory (see, e.g., the discussion in [37,38]). To provide an accurate description the c-field region must be chosen to include these modes, i.e. we must have $\epsilon_{\rm cut} > un$, as shown schematically in Figure 4.

The occurrence of critical fluctuations can be identified by the Ginzburg criteria (see, e.g., [39]), which predicts that fluctuations are important for the three-dimensional Bose gas only in a narrow temperature range about $T_{\rm c}$. Outside this range a pure mean-field description provides a good description of the equilibrium system. In contrast, for low-dimensional systems strong fluctuations prevail over a broad temperature range, and inhibit the formation of phase coherence according to the Mermin–Wagner–Hohenberg theorem [40,41]. For these systems a pure mean-field analysis is of limited use, yet a c-field description of the low-energy modes (**C** region) with a mean-field description of the high-energy states (**I** region) can be used to provide a comprehensive description (see [38,42–44] and Section 3.4.2).

Low-dimensional systems exhibit several additional properties that make them well-suited to simulation by c-field techniques. First, in lower dimensionality the rate of thermalization is significantly reduced with respect to the three-dimensional case. This suggests that the thermalization of the vacuum noise that occurs in truncated Wigner evolution will happen more slowly and simulations in the low-temperature regime should be valid over longer time scales. Second, the density of states increases more slowly with energy as the dimensionality of the system decreases, and thus for one- and two-dimensional systems at finite temperature a larger portion of atoms reside in low-energy, highly occupied modes.

In general the study of one- and two-dimensional Bose gases is an active area of research, and many aspects of their behaviour, particularly dynamics, are not well understood. While the c-field techniques are widely applicable to describing these systems, a significant challenge remains to develop techniques for sampling the Wigner distribution when the Bogoliubov description fails. A few procedures have been developed for

quasi-one-dimensional lattice systems at $T \approx 0$ in [29], and for finite temperature quasi-two-dimensional trapped gases in [45].

Role of projection in ensuring validity. Both the short-time and long-time validity conditions are sensitive to the number of modes in the c-field region and the maximum energy of the modes represented. For this reason it is essential to have a projector in the formal theory to exert as much control as possible over the modes retained in the c-field description.

A natural question that arises is how dependent are the results of a simulation on the energy cutoff we use to define the **C** and **I** regions? For the case of a system in the critical regime it is clear that a lower bound for $\epsilon_{\rm cut}$ is provided by the energy scale *un* as discussed above (see Figure 4). More generally, this lower bound is also appropriate for inhomogeneous systems outside the critical regime. This is because we have chosen to implement the projector in the single-particle basis (see Section 2.2), which provides a good representation of the low-energy modes and a well-defined energy cutoff only when $\epsilon_{\rm cut} > un$.

The criteria for setting an upper bound on $\epsilon_{\rm cut}$ varies greatly according to the application. A large value of $\epsilon_{\rm cut}$ can be used for short-time simulations, subject to the condition given in Equation (96). For equilibrium situations (or long-time simulations where relaxation occurs) typically the condition $\epsilon_{\rm cut} \sim k_{\rm B}T$ (see [10]) ensures that all of the modes in the c-field region are occupied appreciably, and thus described accurately by the Wigner approach (we discuss this case in more detail in Section 3).

Within the aforementioned guides for choosing the cutoff, there is still an appreciable degree of freedom. For example, consider the situation shown in Figure 4, where a particular choice of $\epsilon_{\rm cut}$ is indicated that splits our system of interest into the **C** and **I** regions, which we take to be described by c-field and mean-field descriptions, respectively. In this case, it is clear that an appreciable number of modes appropriately described by mean-field theory are included in the **C** region. Moderate shifts in the value of $\epsilon_{\rm cut}$ result in the transfer of some modes, well described by mean-field theory, between the regions. Clearly this scenario will have no effect on the physical predictions for the complete system as the modes shifted between the regions are equally well described by both formalisms. However, large changes in $\epsilon_{\rm cut}$ will lead to problems: if $\epsilon_{\rm cut}$ is set too low, then strongly fluctuating modes will inappropriately appear in the **I** region; if $\epsilon_{\rm cut}$ is too high, then many sparsely occupied modes will be included in **C**.

While the theoretical motivation for choosing the cutoff is clear, there are only a few studies that have examined the dependence of simulation results on the cutoff. Of most note are the following studies.

- Sinatra *et al*. [10] studied the damping rates for coherent excitations as the number of **C** modes was varied by an order of magnitude. They found that the damping rate varied by a factor of two over this range, and the best results (i.e. those agreeing with the Beliaev–Landau damping result) were obtained for low cutoffs.
- Bradley *et al*. [46] derived Ehrenfest relations for a c-field system, which display an explicit dependence on the projector. They also presented results showing that the macroscopic properties of density distribution and the condensate fraction varied appreciably when the numerical method used was changed from a spectral approach using oscillator states (i.e. implementing the **C** region using a well-defined energy cutoff in the single-particle basis) to a uniform grid (i.e. implicit projection that only provides a momentum cutoff at the inverse of the grid point spacing).

2.3.10. *Features and interpretation of the truncated Wigner method*

Single trajectory interpretation. Phase-space methods provide a practical means for calculating correlation functions, which can only be compared with the equivalent quantities calculated as an ensemble average of experimental measurements. However, for highly occupied fields, the behaviour observed in each trajectory of the TWA seems to be typical of that seen in single realizations of experiments (see, e.g., the results in Sections 4.2 and 4.4). Thus, it is plausible that single realizations of Wigner trajectories should approximately correspond to a possible outcome of a given experiment. This is no more surprising than the observation that the GPE is a remarkably good predictor of the dynamics of individual experimental runs, and follows from taking the classical limit of the full quantum evolution, with the important addition of initial fluctuations.

Restriction to states with positive Wigner function. However, this is not the full story as the Wigner function can be negative for some states (see Figure 3(c)). Negative Wigner functions are not amenable to exact treatment by diffusive processes and so there are, in fact, certain quantum states that are inaccessible to the stochastic sampling methods described in this review. There are actually two points here. First, negative Wigner functions are difficult to sample as an initial condition. Second, a positive Wigner function will not become negative under diffusive TWA evolution. While it may predict the mean fields accurately, it may not (and cannot) give the correct correlation functions for some processes. These are, however, fairly rare with BEC. This restriction limits the range of quantum phenomena to states with positive Wigner functions, ruling out superpositions of number states and demonstrations of the non-locality of quantum mechanics (violation of a Bell inequality).

Spontaneous scattering. The GPE is fundamentally a theory of stimulated (Bose-enhanced) scattering, which does not include spontaneous processes. In particular, scattering into initially unoccupied modes will not occur, although this may eventually occur in computational simulations due to the gradual accumulation of numerical errors. The Wigner method, however, sets an irreducible level of initial fluctuations in all modes of the c-field, i.e. half an atom of vacuum fluctuations. In effect, spontaneous scattering becomes modelled by weakly seeded stimulated scattering.

Multimode averaging. The c-field used in truncated Wigner simulations usually consists of some large number of stochastically sampled modes M. Many observables of interest (e.g. column density, cloud root mean square (rms) width) depend on the values of a significant portion of these modes, so that the statistical fluctuations in the value of such observables can be quite small. Often the behaviour and evolution of these observables exhibit little difference between independent trajectories.

Long-time dynamics. Sampling the initial state introduces fictitious population into the system, i.e. the vacuum noise. In ensemble-averaged calculations, this is subtracted when constructing operator averages from trajectory averages. In single-trajectory dynamics of the truncated Wigner method, the extra population becomes dynamically thermalized and indistinguishable from the rest of the field. There are two effects at work here. First, the truncation of the equation of motion means that quantum-mechanical corrections, which prevent this thermalization, have been neglected. Second, by considering single trajectories, the formal correspondence to operator averages is lost and the results must be interpreted within the context of classical field theory. For long times, the advantage of

the truncated Wigner method is that it provides a more complete physical picture of the system evolution than the GPE, but it must be interpreted with some care. The primary gain is the inclusion of spontaneous effects in the dynamics from the outset.

3. The PGPE

The PGPE formalism is valid for degenerate Bose gases at finite temperature, a system for which many excited modes (in addition to the condensate) of the atomic field may have a high mean occupation, i.e. satisfying the criterion $\langle \hat{a}_j^\dagger \hat{a}_j \rangle \gg 1$. In this section, we describe the PGPE formalism, and show how it can be formulated to make quantitative comparisons with experiments in this regime. Unlike the other c-field techniques described in this review, the PGPE formalism can be described as a 'classical field theory' in the sense of the classical limit taken in Section 2.3.6.

3.1. *Classical field description of thermal Bose fields*

The suggestion that the GPE could be used to describe the dynamical evolution of the Bose field in the limit of large mode occupation was first made by Svistunov in 1991 [47], and later by Kagan *et al*. in [48–50]. Damle *et al*. [51] were the first to investigate this using numerical calculations in 1996. They used the homogeneous GPE with a very weak non-linearity to study the phase-ordering kinetics of a Bose gas in two and three dimensions on small grids, and performed a scaling analysis of the growth of the condensate fraction in a temperature quench.

Subsequently, Marshall *et al*. [52] studied equilibration of a harmonically trapped Bose gas in two dimensions using the GPE. They observed changes in the population distribution of the bare harmonic oscillator states, and relaxation of the density profile from an initial asymmetric form to a radially symmetric one, and interpreted these changes as thermalization.

The introduction of a projection operator to restrict the modes represented by the GPE was first reported by Davis *et al*. [53] for the case of a three-dimensional homogenous gas. At a similar time thermalization for a homogeneous system was demonstrated by Gòral *et al*. [54], who solved the equations of motion for the mode amplitudes explicitly in the classical approximation.

3.1.1. *Importance of the projector and numerical methods*

It has long been known that applying classical field theory to the electromagnetic field results in the ultraviolet (UV) catastrophe in which an infinite number of modes each have the equipartition share of energy, $k_B T$. Thus, it would seem that the effects of a UV catastrophe would also have an impact on the classical field description of the Bose gas. However, the manifestation of the catastrophe is rather different. The GPE is the equation of motion for a classical microcanonical field in which the total energy and particle number (field normalization) is conserved. In thermal equilibrium this energy is shared equally (equipartitioned) between all system modes. Any numerical solution of the GPE is constructed from some finite basis, e.g. choosing an equally spaced grid (equivalent to choosing a basis of planewaves in the first Brillouin zone). Increasing the number of grid points on which the thermally equilibrated GPE solution is constructed means the fixed

energy is now shared between a larger number of modes, so that the average energy per mode (i.e. temperature of the system) will decrease. In this sense, the results of calculations are dependent on the numerical basis, or more correctly the number and nature of the modes contained in the calculation. However, as we discuss in Section 3.1.2, if the modes of the calculation correspond to only the highly occupied modes of the physical system, then a quantitative description of the system can be made. For this reason the use of an explicit projector in the PGPE (68) is of great importance, because it precisely defines the calculation without reference to the numerical implementation. In addition, great care must be taken in implementing numerical methods for propagating the PGPE so that *all* modes of the c-field region are evolved accurately in order to avoid spurious dynamics which can lead to an incorrect representation of the physical system of interest. We note that a classical field formalism has been developed using unprojected grid methods, summarized by Brewczyk *et al.* [55]. While such an approach seems suitable for investigating qualitative behaviour of Bose gases in various regimes, it has not been applied to quantitative comparison with experiments.

Use of grid methods. Grid methods are ubiquitous in the solution of the GPE, but care must be taken in using these methods as the basis of classical field simulations. For example, the cubic non-linearity in the PGPE can generate momentum components up to three times larger than those present in the classical field. In a grid representation of the field this leads to *aliasing*, which corresponds to (unphysical) collisions between modes that do not conserve momentum. Grid methods can be used effectively for numerically solving the PGPE for a uniform gas, if several adjustments are made.

(i) The projector needs to be implemented explicitly. For example, the single-particle energy cutoff, discussed in Section 2.2, can be implemented by setting all modes outside a sphere of radius $\hbar k_{\rm cut} = \sqrt{2m\epsilon_{\rm cut}}$, to zero in momentum space.
(ii) A large number of momentum states outside the projected region need to be retained to avoid the aliasing problem. The equivalent position space requirement is that if $k_{\rm cut}$ is the largest wavevector retained by the projector, then a spatial grid of spacing $\Delta x = \pi/2k_{\rm cut}$ needs to be used to evaluate the non-linear term, which is twice as dense as the Nyquist sampling requirement, $\Delta x_N = \pi/k_{\rm cut}$. An additional discussion of these issues is given in Appendix B.

The experimentally relevant harmonically trapped system poses a more formidable challenge since the natural modes of the grid representation (i.e. planewave modes) bear little resemblance to the harmonic oscillator modes, making projection difficult. Also, we note that in typical experimental regimes there should be of the order of 10^2–10^4 modes in the c-field region (see Section 3.1.2), whereas grid methods usually require more than about 10^5 points to accurately simulate the GPE in three dimensions. Details of an efficient numerical algorithm for the PGPE in a harmonic trap is summarized in Appendix A.

3.1.2. *c-field region for the PGPE: the 'classical region'*

For the PGPE formalism, the occupations of all of the modes of the c-field region satisfy the mean occupation requirement

$$\langle \hat{a}_n^\dagger \hat{a}_n \rangle \approx \overline{\alpha_n^* \alpha_n} \geq n_{\rm cut}, \tag{98}$$

where $n_{\rm cut}$ is a number of the order of one (typical choices range from about 1 to 10). Loosely speaking, $n_{\rm cut}$ is the degree of coherence of the mode, and should be compared with the basic level of quantum fluctuations set by the Wigner function requirement $\overline{(\alpha_n^*\alpha_n)}_{vac} = \frac{1}{2}$ for vacuum modes. We hence refer to the modes satisfying this condition as constituting the *classical region*, in the sense that quantum corrections to c-field equation of motion (68) for these modes are small (see Section 2.3.6).

A further justification for setting $n_{\rm cut}$ can be obtained from Figure 5, where the mean mode occupation is examined as a function of the scaled single-particle energy. When the parameter $(\epsilon-\mu)/k_BT \ll 1$, then the exponential in the quantum Bose–Einstein distribution

$$\bar{n}_{\rm BE}(\epsilon) = \frac{1}{\exp[(\epsilon-\mu)/k_{\rm B}T]-1}, \tag{99}$$

can be expanded to first order to give the classical equipartition distribution

$$\bar{n}_{\rm EQ}(\epsilon) = \frac{k_{\rm B}T}{\epsilon-\mu}. \tag{100}$$

In Figure 5, it can be seen that these two distributions are in good agreement for highly occupied modes, i.e. modes satisfying $\epsilon-\mu \lesssim k_BT$ with mean occupation $\bar{n} \gtrsim 1$.

The properties and size of the classical region for typical experimental parameters are not *a priori* obvious, especially for the case of an interacting gas. In Figure 6, we consider the case of a harmonically trapped system and estimate the number of classical region modes and the number of particles occupying those modes using a Hartree–Fock mean-field calculation [56]. Those results reveal that the number of classical modes is maximum at the condensation transition, with of the order of several thousand modes satisfying condition (98) for the parameters of this calculation.

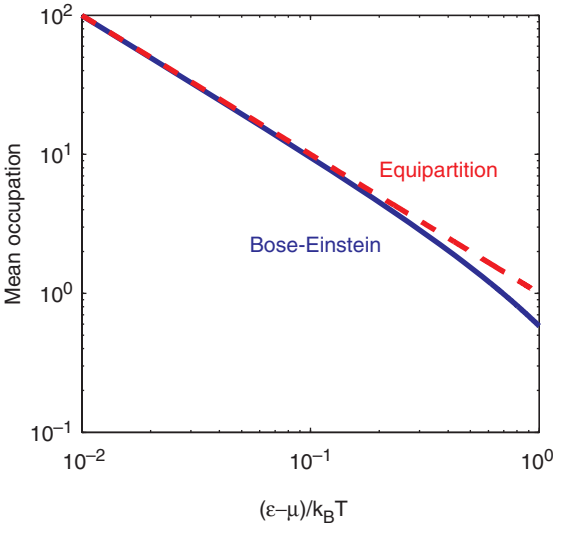

Figure 5. Comparison of the quantum Bose–Einstein and classical equipartition predictions for the mean occupation of a single-particle mode.

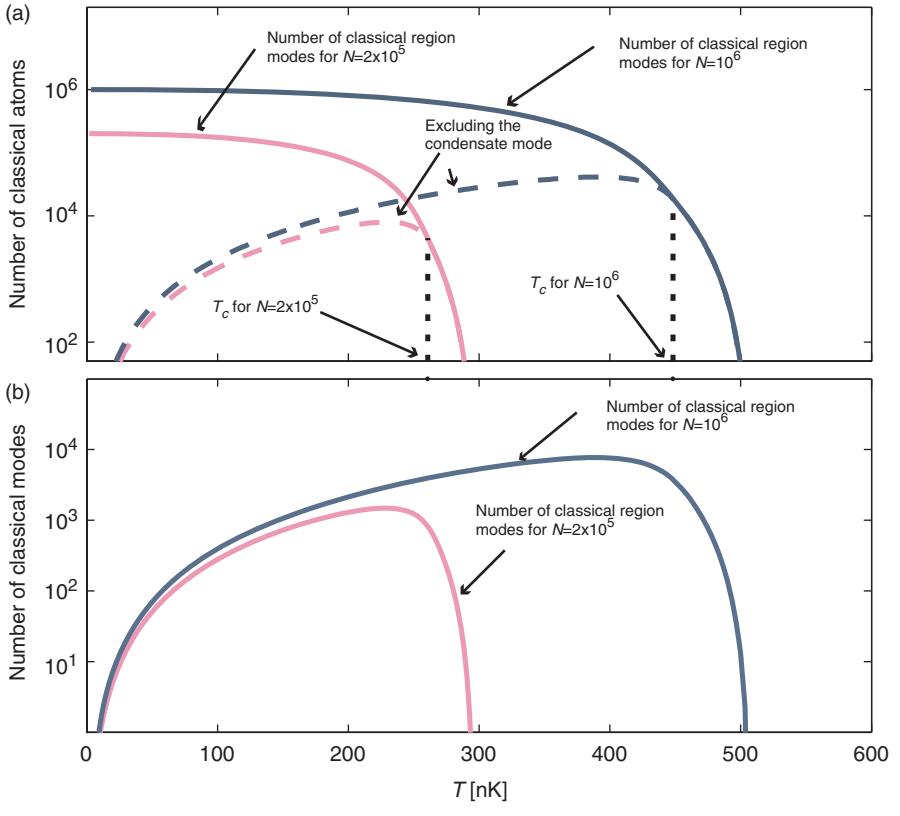

Figure 6. Size and population of the classical region for a harmonically trapped system. (a) Classical region population including (line) and excluding (dashed) the condensate occupation. (b) Number of classical region modes. Results: pink (grey) $N = 2 \times 10^5$ atoms; and blue (black) $N = 1 \times 10^6$ atoms. Results calculated using Hartree–Fock theory (see [56]) for rubidium-87 atoms in an isotropic harmonic trap of frequency 100 Hz with $n_{\rm cut} = 3$ used to define the classical region. Colour refers to the online version.

Strictly, Equation (98) is only applicable to the non-interacting modes of the gas, but can be generalized to the interacting system, e.g. by analysing the occupation of the natural orbitals of the one-body density matrix. However, typically $\epsilon_{\rm cut}$ is sufficiently large compared with the interaction energy scale, that the highest-energy non-interacting modes (i.e. $\phi_n(\mathbf{x})$ with $\epsilon_n \approx \epsilon_{\rm cut}$) in **C** are a good approximation to the modes of the interacting system. In this case Equation (98) can be applied directly to these high-energy modes.

3.1.3. *PGPE formalism*

The appropriate equation of motion for the c-field is the PGPE (68). Since all of the modes in **C** are highly occupied, in a three-dimensional system we find an appreciable number of atoms residing in the incoherent region. Thus, the detailed non-equilibrium dynamics of the system will in general depend on the exchange of energy and particles between **C** and **I.** A consistent formalism for including these processes is described in Section 5. However, for the purposes of this section, we assume that for near equilibrium scenarios the **C** and **I**

regions are weakly coupled, and we can treat each region in isolation as long as we match their temperatures and chemical potentials. Building on this assumption, in the remainder of Section 3 we mainly concern ourselves with the properties and interpretation of the PGPE (68) as a microcanonical means for describing the classical region of a finite temperature Bose gas. In Section 3.2.6 we discuss a mean-field treatment of the incoherent region, **I**, as a means to providing a quantitative description of the full system.

3.2. *Hands-on introduction to the PGPE formalism*

In this section we introduce the basic ideas of the PGPE formalism by example. To do this we present a hands-on case study of how to prepare initial states and evolve them to thermal equilibrium. We introduce various tools for analysing PGPE simulations as needed.

3.2.1. *Simulation parameters*

To guide our presentation we illustrate the PGPE method using simulations for an experimentally realistic system. We take this system to be a harmonically trapped gas of rubidium-87 atoms in a potential

$$V_0(\mathbf{x}) = \frac{1}{2}m(\omega_x^2 x^2 + \omega_y^2 y^2 + \omega_z^2 z^2), \tag{101}$$

where $\{\omega_x, \omega_y, \omega_z\}$ are the oscillation frequencies (and with $\delta V = 0$). For definiteness we take $\omega_x = 2\pi \times 120\,\mathrm{Hz}$, $\omega_{y,z} = 2\pi \times 30\,\mathrm{Hz}$, i.e. the trap has a *fat pancake* geometry with the x-direction being tightly confined. For the calculations we fix the cutoff defining the c-field region at $\epsilon_{\mathrm{cut}} = 33\hbar\omega_z$, so that there are $M = 1560$ single particle modes in **C.** We take the number of atoms in this region to be fixed at $N_{\mathbf{C}} = 10^4$ (see Equation (62)), and verify *a posteriori* that all of the modes are highly occupied as required for the validity of the PGPE formalism.

3.2.2. *Initial state preparation*

The non-linearity of the PGPE causes its evolution to be ergodic and many of the issues involved with appropriate sampling of initial conditions in the truncated Wigner approach can be avoided if we are only interested in the equilibrium properties of the system.

Thus, the generic method to study finite temperature regimes is to begin with a randomized initial state with some definite energy, as specified by the c-field Hamiltonian $E_{\mathbf{C}} = H_{\mathbf{C}}[\psi_{\mathbf{C}}]$ (see (65)). The c-field energy is a constant of motion for the PGPE (68) and forms a convenient macroscopic constraint for specifying the thermal state of the system. The procedure for making such energy states is rather arbitrary. We choose to make use of the Thomas–Fermi approximation to the condensate mode

$$\xi_{\mathrm{TF}}(\mathbf{x}) = \sqrt{\frac{\mu_{\mathrm{TF}} - V_0(\mathbf{x})}{u}}\,\theta(\mu_{\mathrm{TF}} - V_0(\mathbf{x})), \tag{102}$$

where $\theta(x)$ is the unit step function and

$$\mu_{\mathrm{TF}} = \frac{\hbar\bar{\omega}}{2}\left(\frac{15aN_0}{\bar{a}}\right)^{2/5}, \tag{103}$$

is the Thomas–Fermi chemical potential [57], with $\bar{\omega}^3 = \omega_x\omega_y\omega_z$ and $\bar{a} = \sqrt{\hbar/m\bar{\omega}}$. We can generate a state of desired energy by superimposing the Thomas–Fermi state with a (high-energy) randomized state, $\xi_r(\mathbf{x})$, according to

$$\xi_E(\mathbf{x}) = p_0\xi_{\rm TF}(\mathbf{x}) + p_1\xi_r(\mathbf{x}), \tag{104}$$

where the variables p_0 and p_1 are adjusted to obtain the desired energy. In practice, ξ_r is approximately orthogonal to $\xi_{\rm TF}$ and we can take $p_1 = \sqrt{1-|p_0|^2}$.

For reference, under the constraint of fixed c-field normalization, $N_{\mathbf{C}}$, the minimum energy configuration corresponds to the zero-temperature case with all atoms residing in the condensate mode $\xi_0(\mathbf{x})$ (i.e. $N_0 = N_{\mathbf{C}}$), which can be obtained by solving the time-independent GPE (73).

3.2.3. *PGPE thermalization*

Here, we present evidence for the thermalization of the PGPE in the trapped system. To do this we consider two initial microstates of the c-field, $\xi_E^{(\rm a)}(\mathbf{x})$ and $\xi_E^{(\rm b)}(\mathbf{x})$, which we refer to as cases (a) and (b), respectively. Both of these initial states have the same energy $E_{\mathbf{C}} = 20.0N_{\mathbf{C}}\hbar\omega_z$, and are constructed according to the procedure outlined in Section 3.2.2 but with a modified choice of the Thomas–Fermi state, $\xi_{\rm TF}$, as we discuss below. Such initial states will not be equilibrium states, and during PGPE evolution will thermalize. To emphasize the initial non-equilibrium dynamics and the role of thermalization we choose to use distorted Thomas–Fermi states in (104): the initial state $\xi_E^{(\rm a)}(\mathbf{x})$ is produced using a Thomas–Fermi state that has been squeezed in the x direction; the initial state $\xi_E^{(\rm b)}(\mathbf{x})$ is produced using a Thomas–Fermi state that has been squeezed in the y direction. These two initial states, while having the same energy, are clearly very distinct in spatial character as revealed by the density slices shown in Figure 7(a1), (a2), (b1) and (b2). The final states after PGPE evolution for 1000 ms are shown in Figure 7(a3), (a4), (b3) and (b4).

These results show that the system thermalizes, in the sense that the system evolves to more-likely microstates. Indeed, while the states in Figures C7(a3), (a4), (b3) and (b4) are not identical (differ by fluctuations), they are much more similar than their initial states.

To examine the dynamics of thermalization more carefully we show the x-widths of the states, as characterized by the rms value $x_{\rm rms^2} \equiv \langle x^2\rangle_t - \langle x\rangle_t^2$ (where $\langle\cdot\rangle_t$ is the expectation at time t), in Figure 7(c) and (d). Initially, systems (a) and (b) exhibit large oscillations and differ strongly in their width dynamics (see Figure 7(c)), reflecting the differences in the initial non-equilibrium states. After approximately 20 ms the large-scale width oscillations have damped significantly, leaving much smaller fluctuations. In Figure 7(d), we show the width dynamics from 50 to 500 ms. Here, the width fluctuations are about an order of magnitude smaller than the initial oscillations, and despite both systems beginning from very distinct initial states, these dynamics are consistent with both systems thermalizing to the same equilibrium, i.e. the same mean width and fluctuation properties.

There are a large variety of observables that we could compute to examine the thermalization of the system. However, in general, we typically find that the system relaxes towards equilibrium appreciably within a few trap periods. For typical simulations, where we are interested in equilibrium properties and start from the (undistorted) initial state described in Section 3.2.2, we evolve the c-field for several tens of trap periods to thermalize before sampling for system properties.

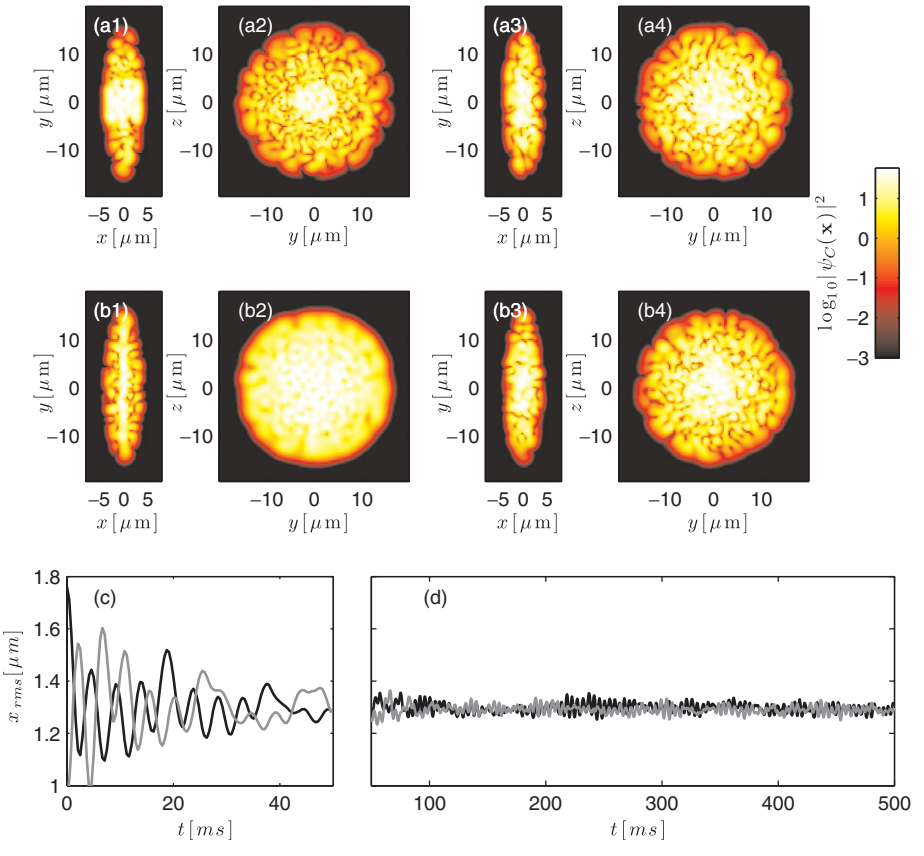

Figure 7. Relaxation to equilibrium. Density slices of the two non-equilibrium initial states: (a1), (a2) $\xi_E^{(a)}(\mathbf{x})$ and (b1), (b2) $\xi_E^{(b)}(\mathbf{x})$; and the respective states they evolve to at $t = 1000$ ms, (a3), (a4) and (b3), (b4). Both states have $E_{\mathbf{C}} = 20.0 N_{\mathbf{C}} \hbar\omega_z$. The rms width of the c-field in the x-direction (c) during the first few trap periods and (d) after 15 trap periods. Width of simulation 'case (a)' (black line) and the 'case (b)' (grey line). Note: the other parameters are given in Section 3.2.1 and the colourmap in the density plots corresponds to $\log_{10}$ of the density measured in units of $(\mu\mathrm{m})^{-3}$.

3.2.4. *Equilibrium: ergodicity, correlation functions and condensate fraction*

Ergodic averaging correlation functions. The c-field energy, given by the functional (65), is a constant of motion under PGPE evolution. Indeed, the energy and other such constants of motion, e.g. field normalization and angular momenta (when the trap has rotational symmetry), take the form of the macroscopic constraints on the thermal state of the system. In principle, the equilibrium properties of the system could be determined by ensemble averaging over all fields consistent with these constraints. The non-linearity of Equation (65) makes finding all functions $\psi_{\mathbf{C}}$, for a given normalization and energy, impossible without approximation. If we were to move beyond the microcanonical ensemble, some form of Monte Carlo sampling could be used, although we do not pursue this possibility here.

In contrast, numerical methods for evolving the PGPE are well developed and allow a different means to sample the ensemble: we can make use of the ergodic hypothesis

(that a system will in time visit every accessible configuration in phase space without bias) to sample microstates of the system. Thus, for an ergodic system, an ensemble average of an observable, O, can be calculated by a time average over a sufficiently long period of dynamical evolution, i.e.

$$\langle O\rangle = \lim_{\theta\to\infty}\left\{\frac{1}{\theta}\int_{\theta_i}^{\theta_i+\theta} \mathrm{d}t\, O\right\} \approx \frac{1}{M_s}\sum_{s=1}^{M_s} O(t_s), \tag{105}$$

where $\{t_s\}\in[\theta_i, \theta+\theta_i]$ is a set of M_s time instances at which the system evolution has been sampled [58,59]. For this choice to be an accurate estimate of the ensemble average we require $M_s \gg 1$, and the time span over which averaging is done to be long compared with the slowest time scale in the problem, e.g. the longest harmonic oscillator period.

In general, the observables of interest are of the form of a correlation function of the field, typically a product of quantum field operators such as

$$\langle \hat{O}\rangle \equiv \langle \hat{\psi}_{\mathbf{C}}^{\dagger}(\mathbf{x}_1)\ldots\hat{\psi}_{\mathbf{C}}^{\dagger}(\mathbf{x}_j)\hat{\psi}_{\mathbf{C}}(\mathbf{x}_{j+1})\ldots\hat{\psi}_{\mathbf{C}}(\mathbf{x}_n)\rangle. \tag{106}$$

This expression could also be generalized to multi-time correlations, although we will not do so here. Note that here the correlation functions only involve the c-field operator: we discuss correlations involving incoherent region operators in Sections 3.2.6 and 3.4.3. To evaluate (106) we make the substitution $\hat{\psi}_{\mathbf{C}}(\mathbf{x})\to\psi_{\mathbf{C}}(\mathbf{x})$, transforming the expression to the general classical field form, and then replace the ensemble average with a time-average according to (105). We note that this procedure is in accordance with that outlined for the truncated Wigner approach (see Section 2.3.1) as we can neglect the commutation relations of the operator fields for the highly occupied modes described by the PGPE.

Position space density. In Figures C8(a)–(c), we show the time-averaged density of the c-field in the $z=0$ plane, i.e.

$$n_{\mathbf{C}}(\mathbf{x}) = \langle \hat{\psi}_{\mathbf{C}}^{\dagger}(\mathbf{x})\hat{\psi}_{\mathbf{C}}(\mathbf{x})\rangle \approx \frac{1}{M_s}\sum_{s}|\psi_{\mathbf{C}}(\mathbf{x}, t_s)|^2. \tag{107}$$

While the instantaneous density (see, e.g., Figure 7(a3) and (a4)) exhibits spatial fluctuations and a random appearance of no particular symmetry, the averaged density is smooth and highly symmetric. The cases in Figure 8(a)–(c) vary from a condensate fraction of less than around 0.5% (Figure 8(a)) to 56% (Figure 8(c)), yet the spatial density profiles change rather gradually and do not provide clear evidence for condensation. We discuss our procedure for quantifying the condensate later in this section. We also note the work of Krauth who has developed a path integral quantum Monte Carlo scheme for the trapped Bose gas in [60] and has computed density profiles for systems with up to 10^4 atoms.

Momentum space density. It is also desirable to be able to calculate correlation functions of the momentum space field operator,

$$\hat{\phi}_{\mathbf{C}}(\mathbf{k}) = \frac{1}{(2\pi)^{3/2}}\int d^3\mathbf{x}\,\hat{\psi}_{\mathbf{C}}(\mathbf{x})e^{-i\mathbf{k}\cdot\mathbf{x}}. \tag{108}$$

A particularly useful example is the momentum density,

$$n_{\mathbf{C}}(\mathbf{k}) = \langle \hat{\phi}_{\mathbf{C}}^{\dagger}(\mathbf{k})\hat{\phi}_{\mathbf{C}}(\mathbf{k})\rangle. \tag{109}$$

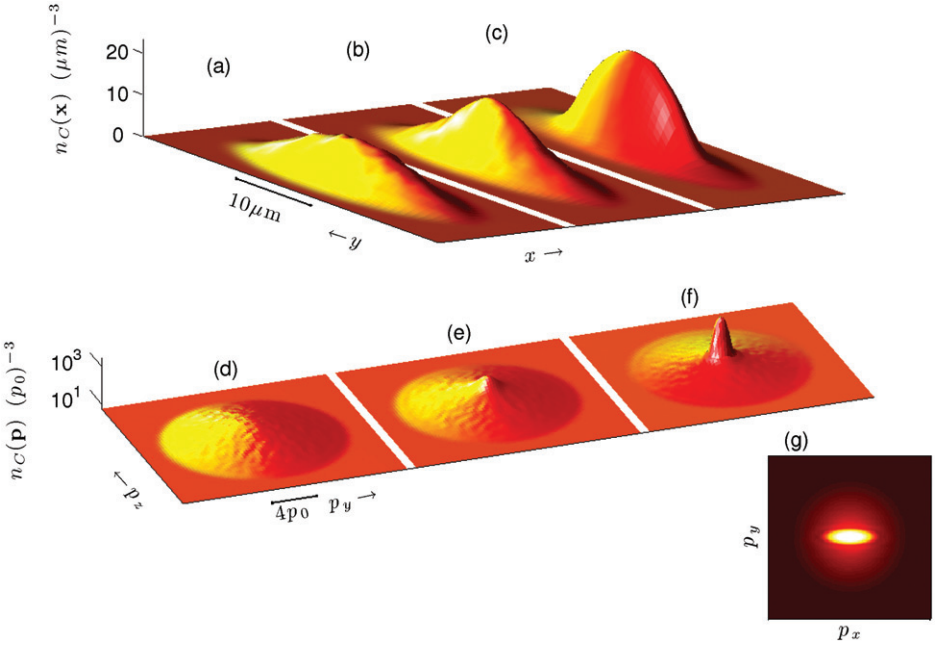

Figure 8. c-field position (a)–(c) and momentum (d)–(f) density. Simulation parameters: (a), (d) $E_{\mathbf{C}} = 24N_{\mathbf{C}}\hbar\omega_z$; (b), (e) $E_{\mathbf{C}} = 22N_{\mathbf{C}}\hbar\omega_z$; (c), (f), (g) $E_{\mathbf{C}} = 15N_{\mathbf{C}}\hbar\omega_z$. Other parameters: $N_{\mathbf{C}} = 10^4$ ^{87}Rb atoms, simulations are evolved for $t = 10^3\pi/\omega_z$, with $M_s = 2500$ samples taken over the last half of the simulation used to time average. Trap parameters and cutoff are given in Section 3.2.1.

The use of Fourier transforms to convert from the spatial to momentum representations of the c-field makes evaluating such observables quite efficient.

In Figure 8(d)–(f), the momentum density in the $k_x = 0$ plane is shown for the cases corresponding to the position space densities in Figure 8(a)–(c). Noting that the momentum density axis is logarithmic, we observe a strong peak forming as the condensate fraction increases, providing an unambiguous signature of condensation. In Figure 8(g), the momentum density for the case in Figure 8(f) is shown in the $k_z = 0$ plane, where the anisotropy of the condensate mode (owing to the anisotropy of the confinement potential in the xy-plane) is clearly apparent.

Condensate. It is important to quantify the amount and nature of condensate in the system. Unlike the uniform system, where the condensate mode is always the zero-momentum mode, particle interactions in the trapped system have a strong effect on the shape of the condensate mode and cause it to be significantly different from the ideal case (see Equation (73) for the regime $T \ll T_c$).

According to the criterion provided by Penrose and Onsager [61], the condensate number N_0 is identified as the largest eigenvalue of the one-body density matrix, defined in terms of the field as

$$G^{1B}(\mathbf{x}, \mathbf{x}') = \langle \psi^*_{\mathbf{C}}(\mathbf{x})\psi_{\mathbf{C}}(\mathbf{x}')\rangle. \tag{110}$$

The corresponding eigenvector is associated with the condensate mode of the system, $\xi_0(\mathbf{x})$, i.e.

$$\int d^3\mathbf{x}'\, G^{1B}(\mathbf{x},\mathbf{x}')\xi_0(\mathbf{x}') = N_0\xi_0(\mathbf{x}). \tag{111}$$

For the uniform system the one-body density matrix exhibits the property of *off-diagonal long-range order* (ODLRO) when a condensate is present [62], i.e.

$$G^{1B}(\mathbf{x},\mathbf{x}') \to \frac{N_0}{V} \quad \text{as } |\mathbf{x}-\mathbf{x}'| \to \infty. \tag{112}$$

In this case the condensate orbital is $\xi_0(\mathbf{x}) \propto 1/\sqrt{V}$, where V is the system volume and the thermodynamic limit is assumed.

Another widely used definition of the condensate 'order parameter' is given by

$$\xi_0(\mathbf{x}) = \langle\hat{\psi}(\mathbf{x})\rangle, \tag{113}$$

based on the idea of spontaneously broken gauge symmetry. The time-averaged value of $\langle\psi_{\mathbf{C}}\rangle$ in the c-field approaches is typically zero, and so this definition is of limited use for quantifying condensate in this review. For a comprehensive discussion on the various definitions of condensate we refer the reader to the review article of Leggett [63], who shows preference to the Penrose–Onsager definition, and states (on the topic of the broken symmetry definition) '...while possibly streamlining some calculations when judiciously used, is liable to generate pseudoproblems and is best avoided'.

In our formalism, $G^{1B}(\mathbf{x},\mathbf{x}')$ is equivalently and much more efficiently computed in the mode basis as $G^{1B}_{mn} = \langle\alpha^*_m\alpha_n\rangle$, which is quite feasible to compute for the typical classical region size (less than about 10^4 modes in $\mathbf{C}$) using time averaging. In the spectral basis the condensate mode is specified by a vector α^0_n such that $\sum_n G^{1B}_{mn}\alpha^0_n = N_0\alpha^0_m$.

In Figure 9, we show the time-averaged position density along two coordinate axes obtained from a c-field simulation. In addition to the total c-field density $n_{\mathbf{C}}$, we also show the condensate density $|\xi_0(\mathbf{x})|^2$. For reference, the condensate number, N_0, for simulations over a wide range of energies are given in Table C1. In the remainder of this section, we develop techniques for extracting other thermodynamic quantities to attribute to these calculations: temperature and chemical potential in Section 3.2.5 and incoherent region atoms in Section 3.2.6.

We note that the correlation functions discussed so far only apply to the c-field region. We return to this issue in Section 3.2.6, when we consider including contributions from the incoherent region. We also mention that higher-order correlation functions, including second-order (e.g. density fluctuations) correlations functions have been calculated using the PGPE approach, see [64–66] (see also [67]). A procedure for calculating two-point correlation functions is discussed in Section 3.4.3.

3.2.5. *Thermodynamic quantities: temperature and chemical potential*

It is desirable to find a means to attribute a temperature to the thermalized state of a c-field simulation. Previous attempts to do this have been based on fitting the occupation of high-energy modes to perturbative calculations for the spectrum based on Hartree–Fock–Bogoliubov (HFB) theory [58,68] (see Section 3.3.1). For harmonically

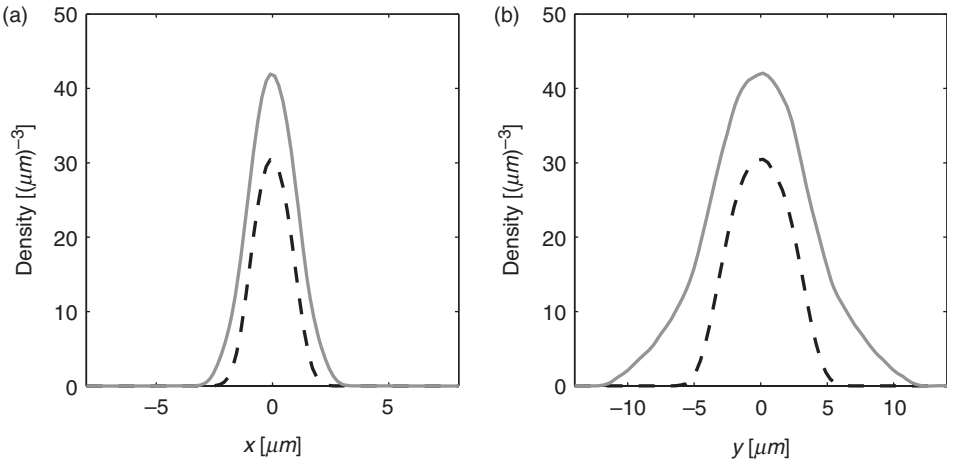

Figure 9. Equilibrium density for the c-field region description of a Bose gas. Condensate density (dashed black line) and c-field region density (solid grey line) densities along (a) the x-axis (more tightly confined direction) x and (b) the y-axis. Simulation for $E_{\mathbf{C}} = 20N_{\mathbf{C}}\hbar\omega_z$ with other parameters given in Section 3.2.1.

Table C1. Summary of PGPE thermalization results for a c-field region with $N_{\mathbf{C}} = 10{,}000$ Rb-87 atoms. Other parameters: $\{f_x, f_y, f_z\} = \{120, 30, 30\}$ Hz and $\epsilon_{\text{cut}} = 33\hbar\omega_z$. For reference, the Thomas–Fermi ground state energy is $E_{\text{TF}} = \frac{5}{7}N_{\mathbf{C}}\mu_{\text{TF}} \approx 9.04N_{\mathbf{C}}\hbar\omega_z$. Note: T and μ are determined by the average of two different choices of Rugh temperature (see [74]), one of which is shown in Figure 10.

$E_{\mathbf{C}}$ ($N_{\mathbf{C}}\hbar\omega_z$)	T (nK)	μ ($\hbar\omega_z$)	N_0 ($\times 10^3$)	N ($\times 10^3$)	$n_{\min}$
14.0	117	7.81	6.41	180	1.34
15.0	141	7.60	5.59	303	1.66
16.0	165	7.34	4.79	477	1.97
17.0	189	7.07	4.02	712	2.27
18.0	214	6.81	3.33	1019	2.58
19.0	238	6.58	2.59	1400	2.88
20.0	265	6.25	1.91	1890	3.20
21.0	289	6.07	1.18	2450	3.50
22.0	315	5.73	0.569	3170	3.83
23.0	350	4.85	0.176	4280	4.18
24.0	420	1.41	0.050	7270	4.63
25.0	602	−9.99	0.024	20,600	5.32

trapped gases, calculation of the HFB modes is much more difficult, and limits temperature calculations to perturbative regimes. However, the temperature can be crudely estimated by fitting the high-momentum components of the system to a non-interacting distribution [59].

An alternative approach of general applicability is found by extending Rugh's dynamical definition of temperature for classical Hamiltonian systems [69] to the PGPE. This scheme has the advantage that it is non-perturbative, and is quite accurate.

Rugh's approach was formulated for a classical mechanical system, and it is convenient to write the c-field Hamiltonian as $H_{\mathbf{C}} = H_{\mathbf{C}}(\mathbf{\Gamma})$, where $\mathbf{\Gamma} = \{Q_j, P_j\}$ is the vector of the

canonical position and momentum coordinates introduced in Section 2.3.6 (Equations (69) and (70)). We also need to explicitly account for the c-field normalization functional (62), $\mathcal{N}_{\mathbf{C}} = \sum_j |\alpha_j|^2$, which is another constant of motion and can also be written as a function of canonical coordinates, i.e. $\mathcal{N}_{\mathbf{C}} = \mathcal{N}_{\mathbf{C}}(\mathbf{\Gamma})$. The usual expression for the temperature of a system in the microcanonical ensemble is given by

$$\frac{1}{T} = \left(\frac{\partial S}{\partial E_{\mathbf{C}}}\right)_{N_{\mathbf{C}}}, \tag{114}$$

where the entropy is defined by

$$S = k_{\mathrm{B}} \ln\left\{\int d\mathbf{\Gamma}\, \delta[E_{\mathbf{C}} - H_{\mathbf{C}}(\mathbf{\Gamma})]\delta[N_{\mathbf{C}} - \mathcal{N}_{\mathbf{C}}(\mathbf{\Gamma})]\right\}, \tag{115}$$

with the delta functions ensuring our microcanonical description is one of fixed c-field energy and normalization.

There are several issues with using Equation (114) to determine the temperature in the PGPE approach. First, it is practically impossible to determine the entropy S when a large number of modes are in the c-field region. Second, Equation (114) cannot be evaluated using a single microcanonical ensemble average, since T depends on the derivative with respect to energy. In 1997 Rugh made a fundamental contribution to statistical mechanics by proving that a microcanonical average could be used to calculate the temperature. This approach is now used extensively in the molecular dynamics community since the microcanonical average can be replaced by a time average, as we do here.

Rugh's result, proven using differential geometry methods, showed that the temperature expression (114) could be equivalently written as

$$\frac{1}{k_{\mathrm{B}} T} = \langle \mathcal{D} \cdot \mathbf{X}_T(\mathbf{\Gamma}) \rangle, \tag{116}$$

rigorously shown to work for Hamiltonian systems at energies where the energy surface is regular [69–71]. The components of the vector operator $\mathcal{D}$ are

$$\mathcal{D}_i = e_i \frac{\partial}{\partial \Gamma_i}, \tag{117}$$

where e_i can be chosen to be any scalar value, including zero, and the vector field $\mathbf{X}_T$ can also be chosen freely within the constraints

$$\mathcal{D}H_{\mathbf{C}} \cdot \mathbf{X}_T = 1, \quad \mathcal{D}\mathcal{N}_{\mathbf{C}} \cdot \mathbf{X}_T = 0. \tag{118}$$

Geometrically this means that the vector field $\mathbf{X}_T$ has a non-zero component transverse to the $H_{\mathbf{C}}(\mathbf{\Gamma}) = E_{\mathbf{C}}$ energy surface, and is parallel to the $\mathcal{N}_{\mathbf{C}}(\mathbf{\Gamma}) = N_{\mathbf{C}}$ surface. A vector field that satisfies these constraints is

$$\mathbf{X}_T = \frac{\mathcal{D}H_{\mathbf{C}} - \lambda_N \mathcal{D}\mathcal{N}_{\mathbf{C}}}{|\mathcal{D}H_{\mathbf{C}}|^2 - \lambda_N(\mathcal{D}\mathcal{N}_{\mathbf{C}} \cdot \mathcal{D}H_{\mathbf{C}})}, \tag{119}$$

where we have introduced the parameter $\lambda_N = \mathcal{D}\mathcal{N}_{\mathbf{C}} \cdot \mathcal{D}H_{\mathbf{C}}/|\mathcal{D}\mathcal{N}_{\mathbf{C}}|^2$. The expectation value in (116) is over all possible states in the microcanonical ensemble and can be evaluated as a time average for our ergodic c-field system. In the interests of brevity we do not discuss

the additional technical details of how the matrix elements in Equation (119) are evaluated, however we point out that a procedure for doing this exactly and efficiently is given in [72].

It is worth giving an example to illustrate the formalism. Consider a simple system of M degenerate oscillators described by $H_{\mathbf{C}} = \sum_j \Gamma_j^2$, with no normalization constraint. Taking $\mathcal{D}_i = \partial/\partial\Gamma_i$ we have that $(X_T)_i = \mathcal{D}_i H_{\mathbf{C}} |\mathcal{D}H_{\mathbf{C}}|^2 = \Gamma_i/H_{\mathbf{C}}$, where we have used that $|\mathcal{D}H_{\mathbf{C}}|^2 = \sum_j \Gamma_j^2 = H_{\mathbf{C}}$. Finally, we have that $1/k_B T = \langle \mathcal{D} \cdot \mathbf{X}_T \rangle = (M-1)/E_{\mathbf{C}}$, which is the standard microcanonical result.

Similar to the discussion above, the chemical potential can be evaluated according to

$$\frac{\mu}{k_{\mathrm{B}} T} = -\left(\frac{\partial S}{\partial \mathcal{N}_{\mathbf{C}}}\right)_{E_{\mathbf{C}}} = \langle \mathcal{D} \cdot \mathbf{X}_\mu(\mathbf{\Gamma}) \rangle, \tag{120}$$

where the conditions on the vector field $\mathbf{X}_\mu$ are

$$\mathcal{D}H_{\mathbf{C}} \cdot \mathbf{X}_\mu = 0, \quad \mathcal{D}\mathcal{N}_{\mathbf{C}} \cdot \mathbf{X}_\mu = 1. \tag{121}$$

The appropriate vector field is of the same form as the right-hand side of Equation (119) but with $H_{\mathbf{C}}$ and $\mathcal{N}_{\mathbf{C}}$ interchanged.

In Figure 10, we show instantaneous values of the Rugh observables for temperature (i.e. $[k_{\mathrm{B}} \mathcal{D} \cdot \mathbf{X}_T]^{-1}$) and chemical potential (i.e. $k_{\mathrm{B}} T \mathcal{D} \cdot \mathbf{X}_\mu$) evaluated from a PGPE evolution. The time-averaged results for these parameters over a broad range of initial energies are given in Table C1.

3.2.6. *Including the incoherent region atoms*

To relate the PGPE results back to an experimental system we need to account for the sparsely occupied modes of the incoherent region, which we have so far ignored. To do this

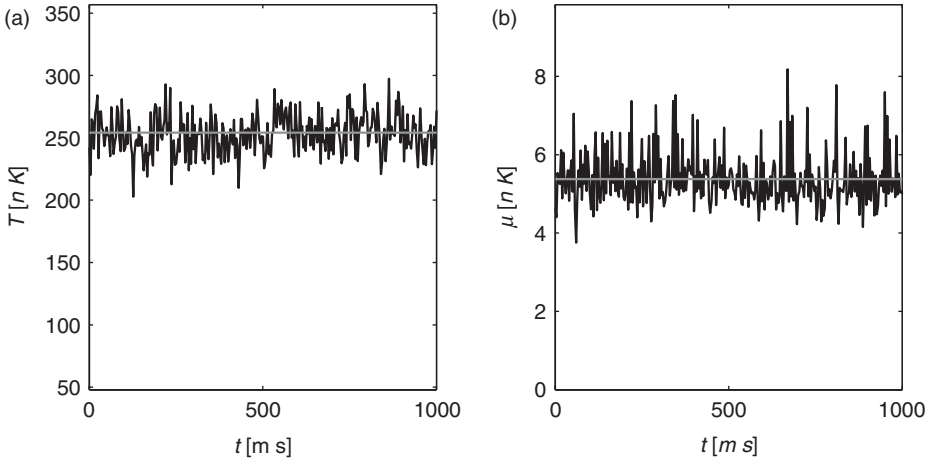

Figure 10. Extracting dynamical thermal quantities. Instantaneous value of Rugh observable for (a) temperature and (b) chemical potential shown as black lines evaluated over one second of evolution. Average values of T and μ shown as grey horizontal lines in (a) and (b), respectively. Simulation for $E_{\mathbf{C}} = 20 N_{\mathbf{C}} \hbar \omega_z$, with other parameters given in Section 3.2.1.

we take the classical region and the incoherent region to be weakly-coupled systems in thermal and diffusive equilibrium (see Figure 11), i.e. with the same temperature and chemical potential. The thermal cloud exists in the potential of the trap plus time-averaged c-field density $n_{\mathbf{C}}(\mathbf{x})$ determined from the PGPE simulations. To model the incoherent region modes we use a Hartree–Fock approximation. As discussed in Section 2.3.9, the mean-field approach provides a good description of the system away from the critical region (e.g. see [73]), and of modes well above the energy scale $un_{\mathbf{C}}$ (also see the discussion in Section 3.2.7).

The average properties of the incoherent region can be calculated from the one-particle Wigner distribution

$$F_{\mathbf{I}}(\mathbf{x},\mathbf{k}) = \frac{1}{\exp(\beta[\epsilon_{\mathrm{HF}}(\mathbf{x},\mathbf{k}) - \mu]) - 1}, \tag{122}$$

where

$$\epsilon_{\mathrm{HF}}(\mathbf{x},\mathbf{k}) = \frac{\hbar^2 k^2}{2m} + V_0(\mathbf{x}) + 2u(n_{\mathbf{C}}(\mathbf{x}) + n_{\mathbf{I}}(\mathbf{x})), \tag{123}$$

is the Hartree–Fock energy, and μ is the chemical potential. The one-particle Wigner distribution is related to the one-body density matrix for the incoherent region (see Equation (137)), and should not be confused with the multi-mode (many-body) Wigner function discussed in Section 2.3.

In this semiclassical description, $\mathbf{x}$ and $\mathbf{k}$ are treated as continuous (commuting) variables. However, care needs to be taken to ensure that (122) is only applied to the appropriate region of phase space spanned by the incoherent region, i.e. single-particle modes of energy exceeding ϵ_{cut}. Interpreted in phase-space coordinates, this region is

$$\Omega_{\mathbf{I}} = \left\{\mathbf{x},\mathbf{k} : \frac{\hbar^2 k^2}{2m} + V_0(\mathbf{x}) \geq \epsilon_{\mathrm{cut}}\right\}. \tag{124}$$

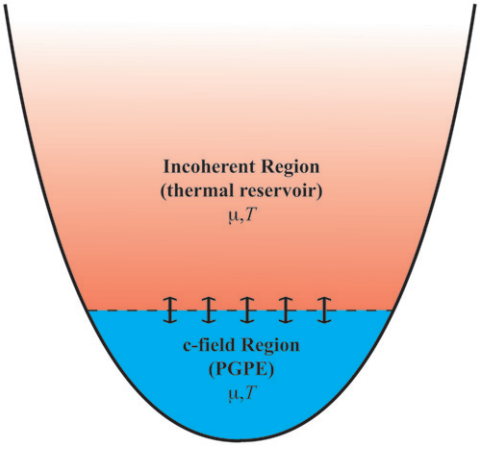

Figure 11. Schematic view of the coupling between the c-field region, described by the PGPE, and the incoherent region. The systems are assumed to be weakly interacting and in thermal and diffusive equilibrium.

A quantity of particular interest for us to calculate is the incoherent region density

$$n_{\mathbf{I}}(\mathbf{x}) = \int_{\Omega_{\mathbf{I}}} \frac{d^3\mathbf{k}}{(2\pi)^3} F_{\mathbf{I}}(\mathbf{x}, k) \tag{125}$$

$$= \int_{K_{\mathrm{cut}}(\mathbf{x})}^{\infty} \frac{dk}{2\pi^2} k^2 F_{\mathbf{I}}(\mathbf{x}, k), \tag{126}$$

where we have made use of the isotropic nature of the kinetic energy term and have implemented the phase-space restriction, $\Omega_{\mathbf{I}}$, as a spatially dependent lower cutoff on the integral

$$K_{\mathrm{cut}}(\mathbf{x}) = \frac{\sqrt{2m[\epsilon_{\mathrm{cut}} - V_0(\mathbf{x})]}}{\hbar} \theta(\epsilon_{\mathrm{cut}} - V_0(\mathbf{x})), \tag{127}$$

where $\theta(x)$ is the unit step function. The incoherent region atoms interact with those in the c-field region, which can be accounted for by adding an effective potential $\delta V = 2u n_{\mathbf{I}}(\mathbf{x})$ to the c-field description. To lowest order this shifts the system chemical potential by $\Delta\mu \approx 2u n_{\mathbf{I}}(\mathbf{0})$. To ensure complete self-consistency, the c-field properties would need to be re-simulated including the effective potential, however this is often unnecessary as the incoherent region density is often quite small and approximately uniform in the spatial region of overlap with the c-field atoms.

We can also calculate the momentum density of the system as

$$n_{\mathbf{I}}(\mathbf{k}) = \int \frac{d^3\mathbf{x}}{(2\pi)^3} F_{\mathbf{I}}(\mathbf{x}, \mathbf{k}) \theta\left(\frac{\hbar^2 k^2}{2m} + V_0(\mathbf{x}) - \epsilon_{\mathrm{cut}}\right). \tag{128}$$

Using the Hartree–Fock analysis we can now include the incoherent region atoms into the PGPE simulation results presented in the previous sections. In Figure 12, we show the typical profiles comparing the c-field and incoherent region density profiles, including the total density

$$n(\mathbf{x}) = n_{\mathbf{C}}(\mathbf{x}) + n_{\mathbf{I}}(\mathbf{x}). \tag{129}$$

These results also allow us to ascribe the total number of atoms, $N = N_{\mathbf{C}} + N_{\mathbf{I}}$, where $N_{\mathbf{I}} = \int d^3\mathbf{x}\, n_{\mathbf{I}}(\mathbf{x})$, to the simulated systems. Using this analysis of the incoherent region in Table C1 we can attribute total particle number to our PGPE simulations. For comparison, in Figure 12 we have also shown the result of a pure Hartree–Fock analysis (as described above, but taking $\epsilon_{\mathrm{cut}} \to 0$ so that all modes are treated using mean-field theory). The pure Hartree–Fock result is for the same temperature and total number as the c-field calculation, yet predicts no condensate, since the temperature is a few nanokelvin above the mean-field critical temperature. Outside such critical regimes the difference between mean-field and c-field calculations is generally much smaller.

The results in Table C1 show that for fixed c-field region (i.e. fixed cutoff ϵ_{cut} and $N_{\mathbf{C}}$), the temperature and total number of particles grow rapidly as the c-field energy increases.

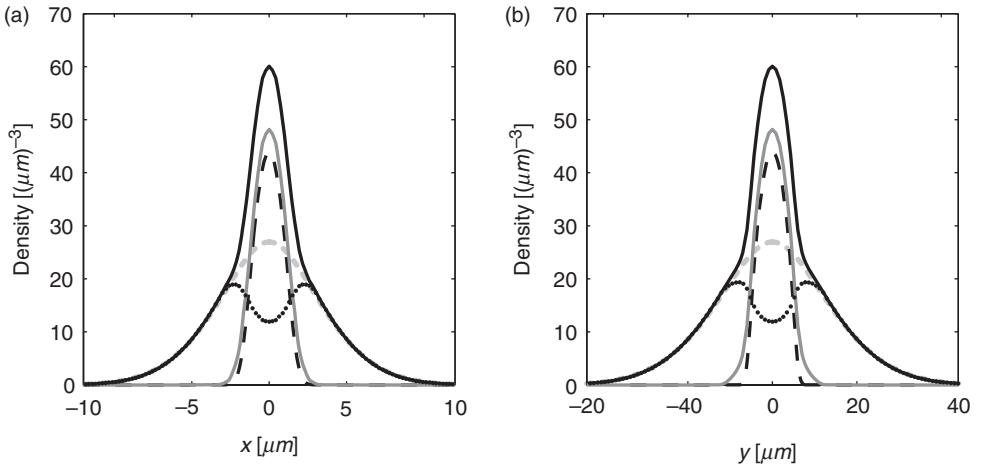

Figure 12. Total density profiles including the incoherent region. (a) Density along x-axis and (b) density along y-axis. Black dashed line, condensate density; grey solid line, c-field region density; black dots, incoherent region density; black solid line, total system density; and grey dashed line, the pure Hartree–Fock result for the total density. Simulation for $E_{\mathbf{C}} = 15\hbar\omega_z$, with other parameters given in Section 3.2.1.

In general, this means that to simulate a fixed total number of particles for various temperatures, we must appropriately manipulate the macroscopic parameters defining our microcanonical system, i.e. $\epsilon_{\rm cut}$, $N_{\mathbf{C}}$ and $E_{\mathbf{C}}$. We will see in Section 5 that use of the SPGPE formalism greatly eases the effort required to calculate systems at definite temperature by making use of a grand-canonical description.

3.2.7. *Validity conditions*

The high mode occupancy of c-field region described by the PGPE makes the validity requirements of this approach somewhat different from those listed for the truncated Wigner approach in Section 2.3.9. In particular, the dominance of classical fluctuations means that the thermalization of quantum noise is not a concern. Thus, the conditions for the PGPE method to provide an accurate description of the c-field region are as follows.

(i) *Good basis*. The cutoff has to be sufficiently large that the single-particle modes provide a good basis for describing the interacting c-field region modes. This condition can be expressed in terms of the peak (central) c-field density as $\epsilon_{\rm cut} - \epsilon_0 \gtrsim un_{\mathbf{C}}(\mathbf{0})$, where ϵ_0 is the ground single-particle energy. This condition also ensures the validity of the separation into **C** and **I** regions in the critical regime (see the discussion in Section 2.3.9).

(ii) *High mode occupation*. The mean occupation of the highest-energy single-particle state is greater than unity. In general, we refer to this quantity, extracted from simulations, as $n_{\rm min}$ which is also listed in Table C1 to demonstrate the validity of those results.

3.3. *Applications to the uniform Bose gas*

3.3.1. *Temperature and quasiparticle modes of the uniform system*

In a sufficiently weakly interacting Bose gas, the Hamiltonian for the system can be diagonalized approximately by a transformation to the Bogoliubov quasiparticle basis. For the uniform gas, the interaction term only mixes modes of opposite momentum, and the transformation from single-particle modes to Bogoliubov quasiparticles of a well-defined momentum $\mathbf{k}$ depends only on the product of the interaction strength u and the condensate number N_0. This is a quantity that can be determined from the PGPE calculations, and so the individual classical fields can be projected onto the Bogoliubov quasiparticle basis, and the time-averaged quasiparticle occupations $N_{\mathbf{k}}$ can be determined accurately.

When the Bogoliubov quasiparticles form a good basis, we expect that at thermal equilibrium the c-field method will result in the mean quasiparticle occupations being given by the equipartition relation (100). If we define the condensate eigenvalue as $\epsilon_0 \equiv \lambda$, and require that the condensate occupation also be given by the equipartition relation

$$N_0 = \frac{k_{\mathrm{B}}T}{\lambda - \mu}, \tag{130}$$

then we can solve for the thermodynamic chemical potential[5] $\mu = \lambda - k_{\mathrm{B}}T/N_0$. By substituting this result into (100) and rearranging we find

$$\frac{\varepsilon_k - \lambda}{k_{\mathrm{B}}T} = \left(\frac{1}{N_k} - \frac{1}{N_0}\right), \tag{131}$$

where the numerator of the left-hand side is the quasiparticle energy *relative* to the condensate. This suggests a prescription for determining the temperature of a simulation. The right-hand side can be measured accurately by ergodic averaging in c-field simulations, and the left-hand side can be evaluated using theoretical predictions of the spectrum $(\epsilon_k - \lambda)$ with the temperature forming a single fit parameter. This procedure was developed by Davis *et al.* [58,68] before the application of the method of Rugh for determining the temperature as described above in Section 3.2.5. We also note the non-projected classical field study of Brewczyk *et al.* [75].

Bogoliubov spectrum. In the limit of large condensate fraction $N_0/N_{\mathbf{C}} \sim 1$, we expect the Bogoliubov transformation to provide an accurate description of the system, with the dispersion relation

$$\varepsilon_k - \lambda = \left[\left(\frac{\hbar^2 k^2}{2m}\right)^2 + (c\hbar k)^2\right]^{1/2}, \tag{132}$$

where $c = \sqrt{N_0 u/mL^3}$ is the speed of sound.

Second-order spectrum. For sufficiently large interaction strengths and temperatures, the cubic and quartic terms of the many-body Hamiltonian that are neglected in the Bogoliubov transformation become important. In [23], Morgan develops a consistent extension of the Bogoliubov theory to second order that leads to a gapless excitation spectrum. This theory treats the cubic and quartic terms of the Hamiltonian using perturbation theory in the Bogoliubov quasiparticle basis, and results in energy-shifts of the excitations away from the Bogoliubov predictions of (132).

The results in Figure 13 clearly show that second-order theory provides a better description of mode occupations than Bogoliubov theory. Other results in [58] show that as the interaction strength increases, initially better agreement with second-order theory is observed, until the validity conditions of that theory are eventually surpassed. In [74] the temperature, as determined from the spectral fitting procedure [58], was shown to be in good agreement with the Rugh (dynamical) temperature (discussed in Section 3.2.5) in the regimes where spectral fitting was valid.

3.3.2. *Shift of T_c for the uniform Bose gas*

The shift in critical temperature T_c with interaction strength for the homogeneous Bose gas has been the subject of numerous studies and debate for almost fifty years since the first calculations of Lee and Yang [76,77]. While there is a finite shift to the chemical potential in mean-field theory, the shift of the critical temperature is zero [78]. The leading order effect is due to long-wavelength critical fluctuations and is inherently non-perturbative. Using effective field theory it was determined that the shift is

$$\Delta T_c/T_{c0} = can^{1/3}, \tag{133}$$

where n is the particle number density, a is the S-wave scattering length and c is a constant of order unity [79]. Until recently results for the value of c disagreed by an order of magnitude and even sign, as summarized in [80, Figure 1]. However, two calculations performed using lattice Monte Carlo have settled the matter, and confirm that the shift is in the positive direction with combined estimate of $c \approx 1.31 \pm 0.02$ (see [37,80]). A number

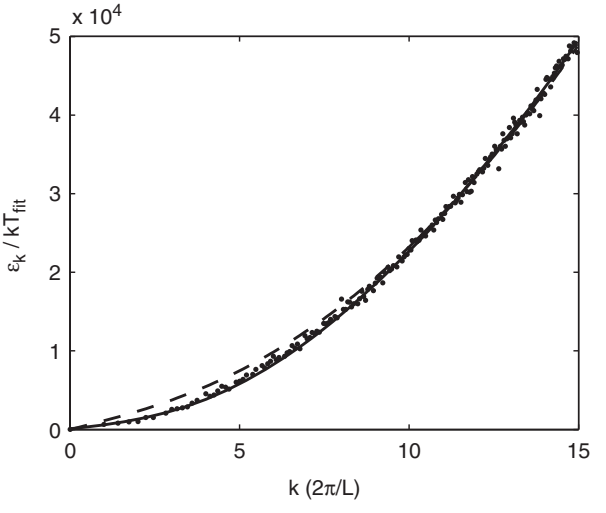

Figure 13. Fits of the simulation quasiparticle population data to dispersion relations. The dots are a plot of $(1/N_k - 1/N_0)$, the solid curve is for the dispersion relation predicted by second-order theory, and the dashed curve is the dispersion relation predicted by Bogoliubov theory. Simulation parameters: $u = 2000L^3\epsilon_L/N_C$, $E_C = 4000N_C\epsilon_L$ and $N_0/N_C = 0.279$, where the unit of energy is $\epsilon_L = \hbar^2/2mL^2$ and the unit of temperature is $T_0 = N_C\epsilon_L/k_B$. Reproduced with permission from [58]. Copyright © 2002 by The American Physical Society.

of recent improved results broadly agree, and useful discussions are provided by Andersen [81] and Holzmann *et al.* [82].

Here, we briefly describe the procedure used by Davis and Morgan [74] to calculate a value for c using the (uniform gas) PGPE.

(i) For a given non-linearity (i.e. scattering length) a randomized initial state of definite energy $E_{\mathbf{C}}$ is evolved with the PGPE, and the temperature is determined by using the methods described earlier in Section 3.2.5.
(ii) As the initial state energy is varied, the critical point is identified using the Binder cumulant $C_{\mathrm{b}} = \langle N_0^2 \rangle / \langle N_0 \rangle^2$, with N_0 the population of the zero-momentum condensate mode. This Binder cumulant characterizes condensate number fluctuations, and takes the universal value of $C_{\mathrm{b}}^{\mathrm{crit}} = 1.2430$ at the transition.
(iii) The shift in the critical temperature is calculated as a function of interaction strength, parameterized by the S-wave scattering length.

By fitting a straight line to the first two points as illustrated in Figure 14, we obtain an estimate for the coefficient

$$c = 1.3 \pm 0.4, \tag{134}$$

where the error specified is owing to the uncertainty in the value of T_{c} for the data point. This agrees with the value determined in [37,80].

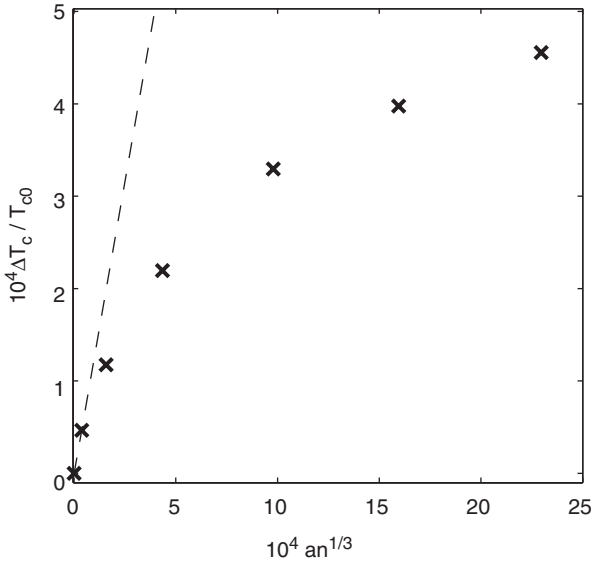

Figure 14. Shift in the critical temperature of a uniform Bose gas with interaction strength determined from PGPE simulations with $N_{\mathbf{C}} = 10^{10}$ for zero scattering length. The dashed line is a linear fit to the first two data points and this has a slope of 1.3 ± 0.4. Reproduced with permission from [74]. Copyright © 2003 by The American Physical Society.

3.4. *Applications to the trapped Bose gas*

3.4.1. *Shift in T_c for a trapped Bose gas: comparison with experiment*

The behaviour of T_c for the harmonically confined Bose gas is drastically different from the uniform gas. There is a shift in T_c owing to finite size effects arising from the fact that the system is not in the thermodynamic limit [83], and a first-order interaction shift owing to mean-field effects [84].

For a typical BEC experiment, the critical temperature deviates from the ideal gas result only by a few per cent. Thermometry of Bose gases at this level of accuracy is challenging: however, in 2004 Gerbier *et al.* reported precise measurements of the critical temperature for a range of atom numbers [73].

Davis and Blakie [85] used those measurements to make the first quantitative comparison of the PGPE formalism with experiment and other theories, which are summarized in Figure 15. The various other theories appearing in Figure 15 are as follows.

- A1: this is the mean-field analytic estimate as calculated by Giorgini *et al.* [84], and was compared with the experimental data in [86].
- A2: this is the analytic estimate as calculated by Arnold and Tomášik [87], which includes next order fluctuation results; however, it is only strictly valid in *broad* traps.

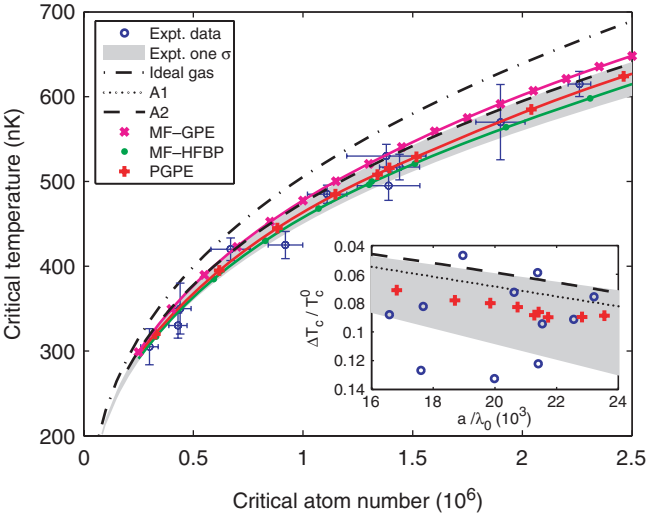

Figure 15. Comparison of theoretical calculations with experiment. The main figure plots T_c versus N_0, whereas the inset plots the shift of T_c against the relevant small parameter a/λ_0. Experimental results: data (open circles), one fit (grey area). Theoretical results for T_c: ideal gas (dot-dashed line), A1 (dotted line), A2 (dashed line), MF-GPE (crosses), MF-HFBP (dots), PGPE (pluses). Solid lines through the data points are polynomial fits. A1 is not shown in the main figure for clarity. The total number of atoms at the critical point is $N = 4.0 \times 10^6$ and $\lambda_0 = h/\sqrt{2\pi m k_B T}$ fits to the data. Reproduced with permission from [85]. Copyright © 2006 by The American Physical Society.

- MF-GPE: the GPE is solved numerically using a variational Gaussian ansatz, and the thermal cloud calculated using a semiclassical approximation [84]. At each temperature the condensate and non-condensate are determined self-consistently with a fixed number of particles, and the critical temperature is taken to be where the condensate fraction decreases to zero. This approach differs from theory A1 because it avoids using perturbation theory around the ideal (saturated) gas density profile to estimate interaction effects.
- MF-HFBP: here the condensate fraction is fixed, and the temperature determined that gives an appropriate self-consistent condensate mode and thermal density (the full Bogoliubov modes are used and the semiclassical approximation is avoided). We have verified that the results are unchanged for equipartition or Bose–Einstein statistics.

The PGPE calculations appear to provide the best theoretical description of experiment, however, error bars in the experimental results are not yet small enough to definitively discriminate between results.

We also note that the HFB Popov calculations (MF-HFBP) use the same procedure as in the PGPE calculation to determine the critical point, the above cutoff density and the total atom number, so that the difference between this *best* mean-field calculation and the PGPE results is a result of beyond mean-field fluctuation effects. This suggests that if experimental accuracy in thermometry could improve by an order of magnitude, then effects of fluctuations on the critical temperature in this system could be investigated directly.

3.4.2. *Quasi-two-dimensional Bose gas*

The phenomena of superconductivity and superfluidity are striking manifestations of the role played by quantum statistics at low temperatures. Altering the temperature or effective dimensionality may radically change the physical properties of quantum degenerate systems. A well-known consequence is that in contrast to the situation in three dimensions, there is no BEC for a homogeneous two-dimensional ideal gas in the thermodynamic limit at any finite temperature [40,41]. Nevertheless, the Berezinskii–Kosterlitz–Thouless (BKT) vortex binding–unbinding phase transition allows the emergence of superfluidity in two-dimensional systems [88,89]. Although weak particle interactions alone are not sufficient to change the situation, an external confinement modifies the density of states in such a manner that the critical point of BEC is elevated to a finite temperature [90]. Therefore, it is not certain *a priori* whether the transformation from normal to superfluid in such systems is a BEC- or BKT-type transition.

This properties of the finite-temperature trapped two-dimensional system have proven difficult to analyse. Strong fluctuations mean that mean-field approaches are inapplicable, however since these fluctuations are classical in nature the PGPE approach is appropriate. Indeed, early studies of the uniform two-dimensional Bose gas were performed by a c-field method, but sampled using Monte Carlo techniques [38,42]. More recently, Giorgetti *et al.* [91] have developed an accurate semiclassical approach for simulating this system.

Simula and Blakie [45] used PGPE simulations of quasi-two-dimensional Bose fields to characterize the low-temperature phases for such systems over a wide parameter range. These simulations show the emergence of thermally activated vortices (see Figure 16(b)

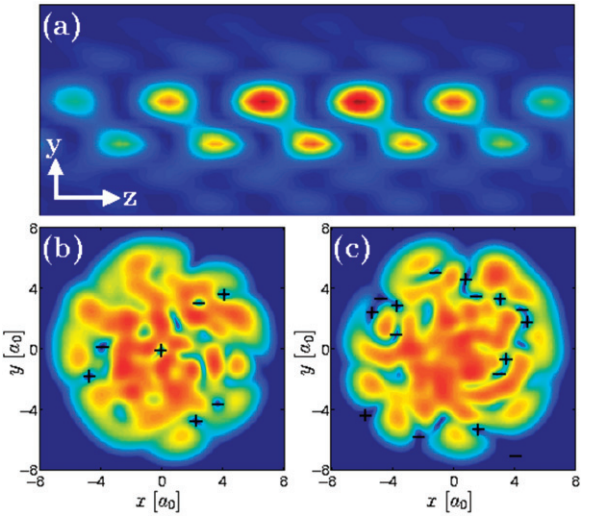

Figure 16. Interference pattern (a) produced by two independent c-fields (b) and (c) at temperature $T = 0.86T_0$. The relevant particle numbers are $N_{\rm cl} = 3.0 \times 10^3$ and $N = 4.0 \times 10^4$. The 'zipper' structure in (a) is the telltale signature of the phase singularity associated with the central vortex in (b). The locations of vortices and antivortices are marked by + and − signs, respectively. Reproduced with permission from [45]. Copyright © 2006 by The American Physical Society.

and (c)), their influence on interference patterns (see Figure 16(a)), and provide strong evidence supporting the view that the BKT-type phase was observed in the recent experiment by Stock *et al.* [92]. More recent work with PGPE simulations have characterized correlation and collective mode properties of the system to quantify the BKT transition point [66,93], and find good qualitative agreement with recent quantum Monte Carlo simulations [94].

3.4.3. *Two-point correlation functions*

Recent experimental developments in ultra-cold gases [95–100] have allowed atomic correlation measurements that are analogous to the photon correlations observed in the landmark experiments of Hanbury-Brown and Twiss [101]. Such correlations are of particular interest in systems where many-body interactions are important [102,103], and in the region of the phase transition, where critical exponents can be measured [104].

The PGPE description is valid in this regime and can be used to calculate these correlations, and assess beyond mean-field effects (cf. [105,106]). We now summarize an approach for calculating these correlations within the PGPE formalism that has been developed by Bezett *et al.* [65].

The quantities of interest are the normally ordered first-order correlation function, $G^{(1)}(\mathbf{x}, \mathbf{x}') \equiv \langle \hat{\psi}^\dagger(\mathbf{x}) \hat{\psi}(\mathbf{x}') \rangle$ (also known as the one-body density matrix), and second-order correlation function, $G^{(2)}(\mathbf{x}, \mathbf{x}') \equiv \langle \hat{\psi}^\dagger(\mathbf{x}) \hat{\psi}^\dagger(\mathbf{x}') \hat{\psi}(\mathbf{x}') \hat{\psi}(\mathbf{x}) \rangle$. From these functions other first- and second-order observables can be obtained directly, such as the density–density correlation function.

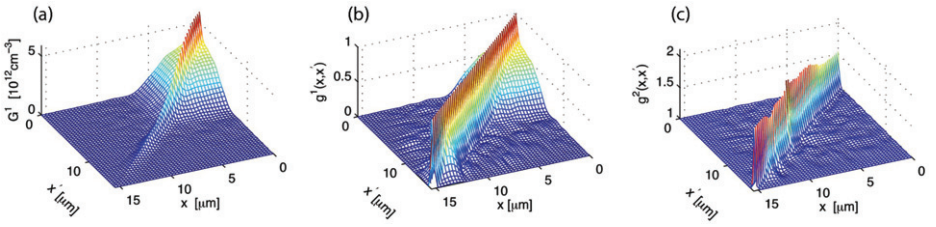

Figure 17. Two-point position space correlation functions of a harmonically trapped Bose gas of $N = 3 \times 10^5$ ^{87}Rb atoms at $T = 159$ nK. Other parameters: $N_0 = 3540$, $\epsilon_{\rm cut} = 36\hbar\omega_x$, with $\{\omega_x, \omega_y, \omega_z\} = 2\pi\{1, 1, \sqrt{8}\} \times 40\,{\rm s}^{-1}$. Reproduced with permission from [65]. Copyright © 2008 by The American Physical Society.

Breaking the full quantum field into c-field and incoherent parts, the correlation functions can be written as

$$G^{(1)}(\mathbf{x}, \mathbf{x}') = G^{(1)}_{\mathbf{C}}(\mathbf{x}, \mathbf{x}') + G^{(1)}_{\mathbf{I}}(\mathbf{x}, \mathbf{x}'), \tag{135}$$

$$\begin{aligned} G^{(2)}(\mathbf{x}, \mathbf{x}') = {} & G^{(2)}_{\mathbf{C}}(\mathbf{x}, \mathbf{x}') + G^{(2)}_{\mathbf{I}}(\mathbf{x}, \mathbf{x}') + 2G^{(1)}_{\mathbf{I}}(\mathbf{x}, \mathbf{x}')G^{(1)}_{\mathbf{C}}(\mathbf{x}, \mathbf{x}') \\ & + n_{\mathbf{I}}(\mathbf{x})n_{\mathbf{C}}(\mathbf{x}') + n_{\mathbf{I}}(\mathbf{x}')n_{\mathbf{C}}(\mathbf{x}), \end{aligned} \tag{136}$$

where $G^{(1)}_j(\mathbf{x}, \mathbf{x}') = \langle \hat{\psi}^\dagger_j(\mathbf{x}')\hat{\psi}_j(\mathbf{x})\rangle$ and $G^{(2)}_j(\mathbf{x}, \mathbf{x}') = \langle \hat{\psi}^\dagger_j(\mathbf{x}')\hat{\psi}^\dagger_j(\mathbf{x})\hat{\psi}_j(\mathbf{x})\hat{\psi}_j(\mathbf{x}')\rangle$ with $j = \{\mathbf{I}, \mathbf{C}\}$ for the incoherent and classical regions, respectively, and we have neglected any correlations between the c-field and incoherent regions.

While the c-field correlations can be evaluated using the approach detailed in Section 3.2.4, for the incoherent region we can make use of the one-particle Wigner function given in Equation (122). Appropriately transforming the Wigner function we obtain the first-order correlation function, i.e.

$$G^{(1)}_{\mathbf{I}}(\mathbf{x}, \mathbf{x}') = \int_{\Omega_{\mathbf{I}}} d^3\mathbf{k}\, e^{-i\mathbf{k}\cdot(\mathbf{x}-\mathbf{x}')} F_{\mathbf{I}}\left(\frac{\mathbf{x}+\mathbf{x}'}{2}, \mathbf{k}\right). \tag{137}$$

As the $F_{\mathbf{I}}$ Wigner description of the incoherent region is Gaussian, we can easily obtain the second-order $G^{(2)}_{\mathbf{I}}(\mathbf{x}, \mathbf{x}') = n_{\mathbf{I}}(\mathbf{x})n_{\mathbf{I}}(\mathbf{x}') + |G^{(1)}_{\mathbf{I}}(\mathbf{x}, \mathbf{x}')|^2$.

Figure 17 illustrates correlation functions for a trapped Bose gas at $T \approx T_{\rm c}$. The results shown are for the case of two points along the x-axis of the system, and in Figure 17(b) and (c) the normalized correlation functions, defined as $g^{(1)}(x, x') = G^{(1)}(x, x')/\sqrt{n(x)n(x')}$ and $g^{(2)}(x, x') = G^{(2)}(x, x')/n(x)n(x')$, are shown. The broad feature apparent in Figure 17(a) and (b) is the off-diagonal long-range order, arising from the emerging condensate in this system. The diagonal ridge is due to short-range thermal correlations. We also note that Holzmann and Castin [107] have used a quantum Monte Carlo method to obtain the pair distribution function for a trapped Bose gas.

3.5. *Applications of non-projected classical fields at finite temperature*

As well as the work of the current authors on quantitative projected c-field techniques, there have been a number of other studies of finite-temperature properties of degenerate

Bose gases. For completeness, in the final part of this section we briefly describe the results that have been obtained.

3.5.1. *Homogenous gas*

In one of the first papers on classical fields, Gòral *et al*. [54] demonstrated the thermalization of a homogeneous multimode Bose gas in a similar manner to Davis *et al*. [53,58]. They expanded the equation of motion for the c-field in terms of mode coefficients, and calculated the non-linear terms by performing the appropriate summations, and implicitly correctly applied a projection operation. Brewczyk *et al*. [75] performed a Bogoliubov analysis of homogeneous Bose gas using a GPE classical field description. Zawitkowski *et al*. [108] attempt to describe not just the classical modes but the **I** region modes using only the GPE by fixing a grid cutoff such that the condensate fraction and temperature agree with that for the ideal Bose gas. Doing this eliminates any possibility of describing, e.g., the effects of interactions on the transition temperature and includes a large number of modes in the problem that should not be described classically. It should be clear from this review that the current authors strongly disagree with this approach.

Leadbeater *et al*. [109] studied the effect of condensate depletion on the critical velocity when an object is dragged through a superfluid. On a related note, Zawitkowski *et al*. [110] performed an interesting study of placing a homogenous moving condensate in a static thermal cloud, and investigated the decay of the superflow as a function of velocity and temperature. Unfortunately, it seems that the lack of projection caused some numerical issues in this work, such as the violation of momentum conservation.

Witkowska *et al*. [111] related the dynamics of a non-linear string to the weakly interacting Bose gas. Nunnenkamp *et al*. [112] made a comparison of three versions of a classical field theory for a one-dimensional Bose gas on a ring. They found that an exact solution in the high-temperature limit of a transfer integral method agreed well with both a molecular dynamics approach and classical field simulations of the GPE. Recently Sinatra *et al*. [113] found non-diffusive phase spreading of a three-dimensional homogenous BEC at finite temperature.

Connaughton *et al*. [114] and Josserand *et al*. [115] have studied condensate formation in the homogeneous gas using a GPE model. In an interesting application related to classical fields, Picozzi and co-workers have investigated the dynamics of equilibration in incoherent non-linear optics both theoretically and experimentally. See, for example, [116–119].

3.5.2. *Trapped gas*

Gòral *et al*. [59] were the first to apply the condensation criterion of Penrose and Onsager [61] to a classical field. They solved a non-projected GPE for the trapped Bose gas at finite temperature, and developed some estimates of thermodynamics properties of the system. Schmidt *et al*. [120] applied the same simulation technique to investigate the decay of an off-centre vortex in a harmonic trap at finite temperature. Recently, Gawryluk *et al*. [121] seeded a trapped $F=1$ spinor condensate with thermal fluctuations and studied the resulting spin dynamics.

The effect of thermal fluctuations in Bose gases is more significant in low dimensions. Kadio *et al*. [67] studied the coherence properties in a quasi-one-dimensional trapped Bose

gas, and analysed the effects of phase fluctuations in a three-dimensional elongated trap. Mebrahtu *et al*. [122] have analysed coherence effects in the spatial splitting of a quasi-one-dimensional BEC and its subsequent merging at finite temperature.

3.5.3. *Superfluid turbulence*

Finally, we mention work in the area of superfluid turbulence, which attempts to describe the formation of tangles of vortices in the homogeneous superfluid transition and the subsequent relaxation to global phase coherence. Many of the simulations of these systems make use of the GPE to describe finite-temperature non-equilibrium dynamics, and hence are directly related to classical field techniques.

Of particular interest to this review is the work of Berloff and Svistunov [123], who studied condensation from a strongly non-equilibrium state in a three-dimensional homogeneous system using the GPE. Their main interest was in the decay of superfluid turbulence, and the establishment of phase coherence, validating the scenario of superfluid growth as earlier described by Kagan, Svistunov and Shlyapnikov [47–50]. Berloff subsequently studied the interactions of vortices and solitary waves and their role in the decay of superfluid turbulence [124], and Berloff and Yin studied their role in turbulence in a two-component system [125]. Recently, Berloff and Youd studied the decay of vortex rings in a homogeneous superfluid at finite temperature [126]. In [127] Kobayashi and Tsubota simulated a GPE with a dissipation at short wavelengths and obtained an energy spectrum consistent with the Kolmogorov law.

4. Applications of the TWPGPE to quantum matter-wave dynamics

As more experimental investigations have begun probing beyond mean-field quantum dynamics in BECs, theoretical applications have begun to explore the role of thermal and quantum fluctuations using the truncated Wigner method. Here, we give a brief survey of the background and recent developments of this method.

4.1. *Background*

The TWA was introduced by Graham in 1973 [128] and has found wide application in the field of laser physics. A precursor of work on trapped Bose gases was carried out by Carter *et al*. [129] who applied phase-space methods to the simulation of the quantum optical non-linear Schrödinger equation. The theoretical formulation and applications to Bose gas dynamics began with the work of Steel *et al*. [130] who developed phase-space techniques for atomic Bose fields and applied them to simulating the time evolution of a one-dimensional homogeneous Bose gas. The truncated Wigner method was compared with the functional positive-P phase-space method [131]. In calculations of the first-order coherence function $g^{(1)}(t) \equiv \langle \hat{a}_0^{\dagger}(t)\hat{a}_0(0)\rangle / \langle \hat{a}_0^{\dagger}(0)\hat{a}_0(0)\rangle$ for the condensate operator $\hat{a}_0$. Different initial states of the condensate were sampled including the coherent state and the Bogoliubov state. A general conclusion of this work, which provides a reliable guide, is that the positive-P method, while exact, is unstable except for very short simulation times, whereas the truncated Wigner method, while approximate, is stable. Many

subsequent works have considered aspects of the validity of the truncated Wigner method and its applications to dynamical Bose gases using both full phase-space approaches, and the classical field method based on analysis of single trajectories.

A distinction between the formulation of [130] and the c-field description presented in Section 2, is the emphasis placed on projection into a low-energy subspace, both formally and numerically. In the TWPGPE formulation, the projection operator imposes a formal UV cutoff which allows a measure of control over the sometimes spurious effects of vacuum noise arising in the truncated Wigner method.

4.2. *Condensate collisions in free space*

The Bragg scattering of a condensate into a superposition of states of momentum $\mathbf{0}$ and $2\hbar\mathbf{k}$ creates a well-characterized non-equilibrium initial condition that is easily produced in experiments [133–136]. This scenario is shown schematically in the centre-of-mass (COM) frame (in position space) in Figure 18(a), where the original and scattered wavepackets move away from each other. In the subsequent dynamics, but while the two wavepackets still overlap in position space, pairs of atoms are scattered onto a spherical shell in momentum space (see Figure 18(b)). This scattering, often referred to as an S-wave halo, is clearly seen in experiments [6,137], but is absent in a GPE description.

The truncated Wigner method was first used to model this process by Norrie *et al.* [34,132]. Beginning with a condensate with mode function $\xi_0(\mathbf{x})$, Bragg scattering was

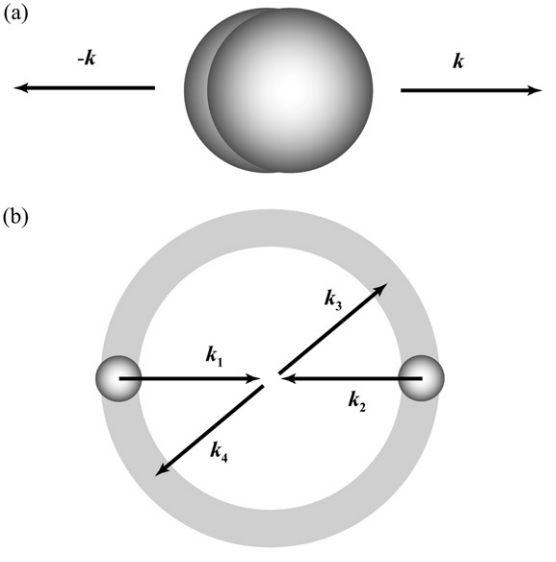

Figure 18. Schematic of the condensate collision scenario of [132]. (a) Position space densities of initially overlapping, counter-propagating condensate wavepackets. (b) Momentum space representation of possible energy and momentum-conserving collisions between atoms in the two condensates ($\mathbf{k}_1, \mathbf{k}_2$) onto the allowed spherical scattering halo ($\mathbf{k}_3, \mathbf{k}_4$), indicated by the grey annular region in the collision plane.

assumed to scatter half the condensate, resulting in the superposition of two wavepackets with momenta $\pm\hbar\mathbf{k}$ (in the COM frame) [138], i.e.

$$\psi_0(\mathbf{x}) = \frac{\xi_0(\mathbf{x})}{\sqrt{2}}\left[e^{i\mathbf{k}\cdot\mathbf{x}} + e^{-i\mathbf{k}\cdot\mathbf{x}}\right]. \tag{138}$$

The full initial condition (see Figure 19(a) and (b)) was sampled by adding vacuum noise to modes orthogonal to ψ_0 (see Equation (90)). In the truncated Wigner simulation modes on a spherical shell of radius $v \approx 10\,\text{mm s}^{-1}$ in velocity space are seen to grow, while the initial wavepackets are situated at the poles of this sphere (see Figure 19(c) and (d)).

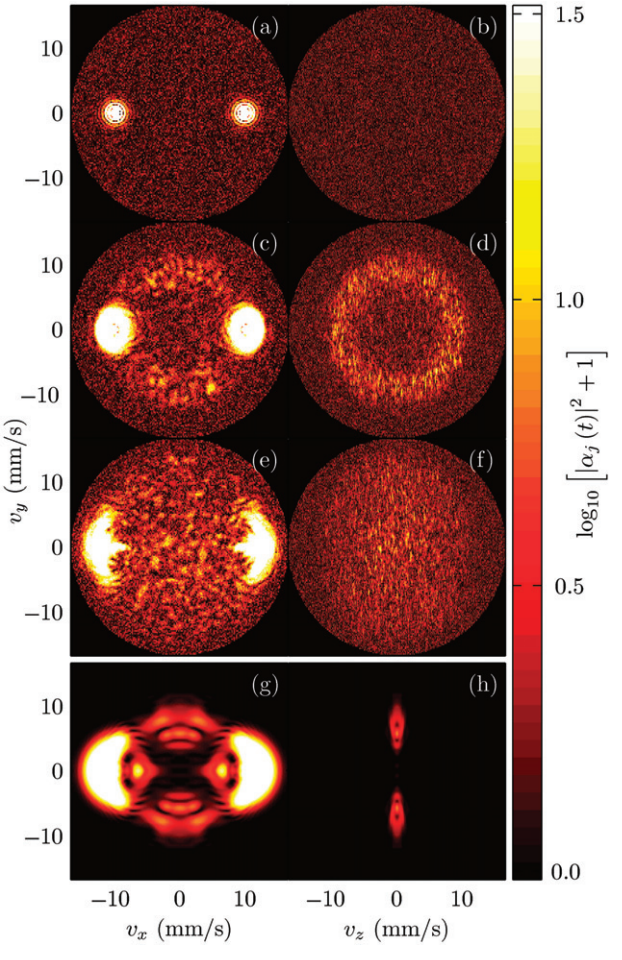

Figure 19. (a)–(f) Velocity mode populations on the planes $v_z = 0$ (left) and $v_x = 0$ (right) for the condensate collision described in the text at $t = 0$ (top), $t = 0.5$ ms and $t = 2.0$ ms (bottom). The spherical momentum cutoff is clearly visible in the upper plots owing to the presence of quantum fluctuations. (g)–(h) Mode populations at $t = 2.0$ ms for an identical collision excluding vacuum noise. Reproduced with permission from [132]. Copyright © 2005 by The American Physical Society.

The importance of vacuum fluctuations is clear: they seed the growth of the halo modes, thus *mimicking* spontaneous processes. It was found that after the halo first develops (see Figure 19(e) and (f)), the stimulated evolution of these scattered modes leads to turbulent dynamics. In contrast, no such spherical shell is seen to develop in the GPE simulations (see Figure 19(g) and (h)).

We also note the work of Deuar and Drummond [140] which used a positive-P method (see [141–143]) to simulate BEC collisions. The positive-P method is a phase-space approach, like the Wigner method, but does not require approximation (i.e. the *truncation* of third-order derivates) to arrive at a set of stochastic equations for any Hamiltonian which is at most quartic in operators. The application to condensate collisions represents a significant success of the method for modelling real-time dynamics of atomic Bose fields. While providing an exact mapping and being used widely for treating quantum optical systems (where dissipation is usually significant and interactions weaker), for pure Hamiltonian evolution the method suffers from stability problems limiting its use to short simulations and low-density systems. Comparing with truncated Wigner simulations, Deuar and Drummond found discrepancies between the two approaches for the early time dynamics of initially unoccupied modes into which atoms were scattered. While directly probing such a discrepancy in an experiment would be difficult, this result emphasizes the need for care in interpreting TWPGPE results for sparsely occupied modes.

4.2.1. *Condensate depletion*

A comparison between the truncated Wigner method and Fermi's second golden rule was made by Ferris *et al.* [139] for the case of colliding condensates in the uniform system. That study compared the early time depletion of the colliding condensates owing to spontaneous scattering with the prediction of Fermi's golden rule

$$\frac{\mathrm{d}N_0}{\mathrm{d}t} = \frac{u^2 m|\mathbf{k}|}{2\pi\hbar^3 V} N_0^2, \tag{139}$$

where N_0 is the number of remaining (unscattered) condensate atoms, and V is the system volume. The condensate population from the truncated Wigner simulation is shown in Figure 20, where the good agreement with the estimates of Fermi's golden rule is evident at short times. The growing discrepancy at long times arises from the depletion of the condensate and the stimulated dynamics of the scattered modes.

4.3. *Truncated Wigner treatment of three-body loss*

The three-body loss process is an inherently non-diffusive process in phase space (the generalized FPE contains derivatives beyond second order in the phase-space variables), and thus does not admit an exact formulation in terms of SDEs for any pseudo-probability distribution.

An important consideration must be borne in mind at this point: *practical* application of stochastic methods is not feasible for problems containing higher than second-order derivatives for phase-space variables. Thus, a more general statement of the TWA is that it should include all terms up to second order in phase-space variable derivatives, subject to

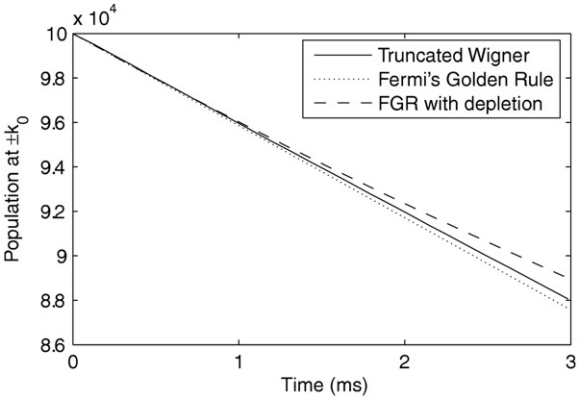

Figure 20. Reduction in condensate population during a condensate collision. Wigner simulations (solid), a linear fit to the rate given by Fermi's golden rule (dotted) and the solution to the differential Equation (139) that includes condensate depletion (dashed). Reproduced with permission from [139]. Copyright © 2008 by The American Physical Society.

the usual validity conditions of weak interactions and high mode occupation. This is the approach taken in the treatment of three-body loss.

The basic technical extension beyond the standard TWA presented in Section 2.3.6 is an additional stochastic term which models the diffusive effects of inelastic loss. Thus, while elastic two body collisions do not generate a stochastic equation of motion within TWA (second-order terms are identically zero), three body inelastic collisions introduce a stochastic element to the evolution.

The three-body loss master equation for the system density operator $\hat{\rho}$, which has been rigorously derived by Jack [144,145], takes the form

$$\left.\frac{\partial\hat{\rho}}{\partial t}\right|_3 = \frac{K_3}{6}\int \mathrm{d}^3\mathbf{x}\left\{2\hat{\psi}(\mathbf{x})^3\hat{\rho}\hat{\psi}^\dagger(\mathbf{x})^3 - \hat{\psi}^\dagger(\mathbf{x})^3\hat{\psi}(\mathbf{x})^3\hat{\rho} - \hat{\rho}\hat{\psi}^\dagger(\mathbf{x})^3\hat{\psi}(\mathbf{x})^3\right\}, \tag{140}$$

which generates the time evolution for the total atom number

$$\frac{\mathrm{d}N}{\mathrm{d}t} = -K_3\int \mathrm{d}^3\mathbf{x}\, g_3(\mathbf{x})n(\mathbf{x})^3, \tag{141}$$

where

$$g_3(\mathbf{x}) = \frac{\langle\hat{\psi}^\dagger(\mathbf{x})^3\hat{\psi}(\mathbf{x})^3\rangle}{\langle\hat{\psi}^\dagger(\mathbf{x})\hat{\psi}(\mathbf{x})\rangle^3}. \tag{142}$$

Within the TWA Equation (140) leads to a SDE for the c-field $\psi_{\mathbf{C}}(\mathbf{x})$

$$d\psi_{\mathbf{C}}(\mathbf{x}) = \mathcal{P}_{\mathbf{C}}\left\{-\frac{K_3}{2}|\psi_{\mathbf{C}}(\mathbf{x})|^4\psi_{\mathbf{C}}(\mathbf{x})\mathrm{d}t + \sqrt{\frac{3K_3}{2}}|\psi_{\mathbf{C}}(\mathbf{x})|^2\, dW_3(\mathbf{x},t)\right\}, \tag{143}$$

[146] (in addition to the terms already in the TWPGPE (60)) where the noise term is given by[6]

$$dW_3(\mathbf{x}, t) = \sum_{n \in \mathbf{C}} \mathrm{d}\xi_n \, \phi_n(\mathbf{x}), \tag{144}$$

with $\mathrm{d}\xi_n(t)$ a complex Gaussian noise satisfying

$$\overline{\mathrm{d}\xi_n(t)\mathrm{d}\xi_{n'}(t)} = 0, \tag{145}$$

$$\overline{\mathrm{d}\xi_n^*(t)\mathrm{d}\xi_{n'}(t)} = \delta_{nn'} \, \mathrm{d}t. \tag{146}$$

4.3.1. *Application to condensate collapse*

The three-body loss formalism was originally derived and applied to quantify the atom loses in condensate collisions [34,132], where it was shown to be a small effect. A regime where three-body corrections are more important is in the description of the Bose-nova experiment performed by Donley *et al*. [147]. In that experiment a Feshbach resonance was used to suddenly change the scattering length from a value of $a \approx 0$ (ideal stable BEC) to a negative value (i.e. attractive interactions), causing the system to collapse. During this process the condensate density increases significantly, and from Equation (141) it is clear that the three-body loss will become more important. This problem was studied with the TWPGPE approach by Wüster *et al*. [148], who assessed the effects of quantum and thermal fluctuations on the collapse process. Where comparison was possible, the TWPGPE simulations of the collapse process agreed quantitatively with the results of HFB theory, and both theories predicted slower collapse than observed in the experiment.

4.4. *Quantum reflection of a BEC*

Scott *et al*. [149,150] used the GPE and the TWA to model the collision of a BEC with an abrupt potential barrier, as studied experimentally by Pasquini *et al*. [151,152]. The system consists of a BEC held in a magnetic trap which is then accelerated at normal incidence toward a steep potential drop. Two regimes of behaviour for these reflections were characterized, as described below.

(i) For low approach velocities the BEC was observed to suffer from disruption owing to interference from incident and reflected components. Most aspects of these slow collisions were adequately explained by the GPE, however for dense initial condensates the inclusion of vacuum fluctuations was observed to have an appreciable effect on the dynamics through the formation of a scattering halo (see Figure 21).

(ii) At higher velocities there is negligible disruption owing to interference, so that the GPE results are relatively smooth. Studying this regime with the truncated Wigner approach, the inclusion of vacuum fluctuations cause a large scattering halo to develop.

In both regimes the experiments and the truncated Wigner results were found to be in quantitative agreement.

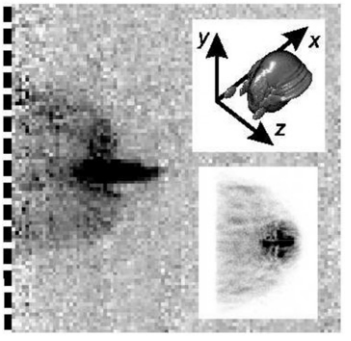

Figure 21. Experimental absorption image of BEC for an impact velocity of $v_x = 3.0\,\text{mm s}^{-1}$ at $t = 120$ ms, having reflected from the Casimir–Polder potential of a pillared silicon surface. The field of view is 500 μm, the vertical dashed line indicates the position of the barrier. Lower inset: corresponding simulated absorption image in the yx-plane including quantum fluctuations for reflection from a barrier of height $V = 1.67 \times 10^{-31}$ J. Upper inset: equivalent constant density surface excluding quantum fluctuations, axes are shown in the figure. The BEC in this simulation has a peak density of 5.2×10^{12} cm^{-3} with its long axis perpendicular to barrier. Reproduced with permission from [149]. Copyright © 2006 by The American Physical Society.

4.5. *Applications to optical lattices*

There have been several studies of atom dynamics in one-dimensional optical lattices using the truncated Wigner approach.

4.5.1. *Dynamical instability of a BEC at the band edge of an optical lattice*

Ferris *et al.* [139] presented experimental results and truncated Wigner simulations of the dynamically unstable evolution of a BEC prepared in a band-edge state in a one-dimensional optical lattice.

The theoretical description was based on a full three-dimensional simulation of the experimental system, and included degrees of freedom transverse to the lattice, and excited band states along the lattice direction. The large number of modes needed to accurately model the actual experimental system (i.e. in the combined lattice and weak harmonic potential), would violate the validity condition $N_{\mathbf{C}} \gg M/2$ (see Section 2.3.9). To avoid this, the theoretical model was simplified to a translationally invariant case, greatly reducing the number of basis modes required. The truncated Wigner simulations showed that vacuum fluctuations have an important role in seeding the growth of unstable modes, leading to rapid depletion and heating of the condensate. Furthermore, the drastic modifications of energy and momentum conservation in the lattice were observed to have a substantial effect on the initial dynamics in the system, particularly the modes into which atoms were spontaneously scattered.

4.5.2. *Quantum fluctuation effects on dipolar oscillations*

In [29], Polkovkinov and Wang considered the dipolar motion of a condensate displaced relative to the centre of the harmonic trap in a quasi-one-dimensional lattice. This study, conducted within the tight-binding Bose Hubbard description [35,153], examined the

nature of the damping, and how it is influenced by the quantum fluctuations included within the truncated Wigner treatment. An adiabatic mapping procedure was used to sample the initial Wigner distribution which allowed them to sample the ideal Bose gas in the harmonic and lattice potential [154] as discussed in Section 2.3.8. Their study presented evidence that there is a smooth crossover between the classical localization transition (overdamped oscillations that occur beyond a critical displacement) and the superfluid-to-insulator quantum phase transition in the limit of zero trap displacement. Using a similar tight binding approach, the evolution of phase coherence in a deep quasi-one-dimensional lattice with a large number of atoms per lattice site was examined and compared with experiments by Tuchman *et al*. [155].

4.5.3. *Number squeezing in one-dimensional lattices*

Ruostekoski and Isella have also considered quasi-one-dimensional optical lattice systems using the truncated Wigner approach, but used a beyond tight binding description [156,157], which included excited band states.

In [156], they considered the effect that lattice loading has on a quasi-one-dimensional gas initially prepared in a harmonic trap. The initial state was sampled using the Bogoliubov procedure [158,159] (see Section 2.3.7), and then evolved through a simulated lattice loading procedure. Coherence and number fluctuations were evaluated, and observed to be in qualitative agreement with the experiments of Orzel *et al*. [160].

In later work Ruostekoski and Isella considered the quantum dynamics in shallow lattices [157], and modelled experiments by Fertig *et al*. [161] of dipolar motion of a BEC in an optical lattice. In their simulations, the initial state was sampled using the Bogoliubov procedure for the combined harmonic and lattice potential. Using the truncated Wigner approach they modelled the sudden trap displacement and subsequent dynamics and found qualitatively good agreement with the damping behaviour observed in experiments. These results, which are for the low atom number regime (i.e. $N_{\mathbf{C}} \sim 10^2$), where the strict validity conditions (see Section 2.3.9) for the Wigner approach are not satisfied, provides an indication that the Wigner method has an extended range of applicability.

4.5.4. *Dephasing in one-dimensional interferometers*

Bistritzer *et al*. [162] examined the effect of quantum-phase fluctuations on a condensate split into two parts. Their system consisted of a pair of quasi-one-dimensional Bose gases which realize a basic model for an atom interferometer. These one-dimensional gases were modelled with a Bose Hubbard Hamiltonian using the Wigner method (note there was no explicit optical lattice potential, but the gases were treated in a *lattice approximation*). In detail they used the adiabatic mapping procedure to sample the initial Wigner distribution as discussed in Section 2.3.8. In this application, an initial non-equilibrium state was prepared by imposing a relative phase between the two quasi-one-dimensional systems. The dephasing between the (uncoupled) systems was then calculated as a function of time and shown to decay exponentially with little sensitivity to temperatures below a characteristic temperature T^*.

4.5.5. *Quantum phase transition in a one-dimensional optical lattice*

Dziarmaga *et al*. [163] investigated the quantum phase transition from Mott insulator to superfluid transition in a periodic one-dimensional optical lattice. The Kibble–Zurek mechanism (KZM) predicts that when the lattice is ramped down in a time of the order of τ_Q (ramping up the tunnelling rate) the winding number will grow through a random walk of BEC phases. In the high occupation regime the TWA leads to a discrete non-linear Schrödinger equation of motion, and the initial conditions were sampled to approximate a Mott insulator state $|n, n, n, \ldots, n\rangle$, where n is the (integer) number of particles per lattice site. The KZM scaling of the winding number with τ_Q was confirmed using truncated Wigner simulations of the transition dynamics.

4.6. *Dynamical instabilities and quasiparticle dynamics: quantum de Laval nozzle*

The quantum dynamics of a dynamically unstable supersonic current have been investigated by Jain *et al*. [164]. They considered the stationary flow of a condensate in a one-dimensional toroidal trap that was modified to form a double *de Laval nozzle* geometry by the inclusion of a spatially varying potential (around a torus of length L) of the form

$$V(x) = -V_0 \sin^2\left(\frac{2\pi x}{L}\right) \tag{147}$$

which has periodicity two over the region $-L/2 \le x \le L/2$. There are persistent current solutions for this system which have distinct spatial regions of subsonic and supersonic flow, with two acoustic horizons for sound waves (phonons): one where the flow goes supersonic (black hole, see Figure 22(a)) and the other where it returns to the subsonic level (white hole). A typical stationary solution of the GPE which has this property is shown in Figure 22(b) and the flow scenario is shown in Figure 22(c). Supersonic flows are known to be energetically unstable and will decay in the presence of dissipation unless the decay is topologically prohibited such as in a toroidal trapping configuration. It was found that the system can also be dynamically unstable in certain scenarios, and the quantum dynamics of the instability were investigated with the truncated Wigner approach and compared with the predictions of Bogoliugov theory.

For a system with a dynamical instability the usual Bogoliubov expansion (72) is inadequate [164,165], as modes arise with complex eigenvalues. For these unstable modes the Bogoliubov description acquires an irreducible off-diagonal component, which takes the form (see Equation (47) of [164])

$$\begin{aligned}\hat{H}_2 = &\sum_j \hbar\omega_j\left[(\hat{b}^\dagger_{j+}\hat{b}_{j+} - \hat{b}^\dagger_{j-}\hat{b}_{j-}) - \int \mathrm{d}x\,(|V_j^+|^2 - |V_j^-|^2)\right] \\ &+ \sum_j i\hbar\gamma_j\left[(\hat{b}_{j+}\hat{b}_{j-} - \hat{b}^\dagger_{j+}\hat{b}^\dagger_{j-}) + \int \mathrm{d}x\,(U_j^+ V_j^- - U_j^{+*} V_j^{-*})\right],\end{aligned} \tag{148}$$

where $\{U_j^+, V_j^+\}$ and $\{U_j^-, V_j^-\}$ are the positive and negative energy Bogoliubov modes, respectively, $\mathrm{e}_\mathrm{j}^\pm = (\pm\omega_\mathrm{j} - \mathrm{i}\gamma_\mathrm{j})\hbar$ are the respective (complex) eigenvalues for these modes with annihilation operators $\hat{b}_{j\pm}$ (see [165]). The second line is analogous to the interaction Hamiltonian for non-degenerate down-conversion of light by a non-linear crystal.

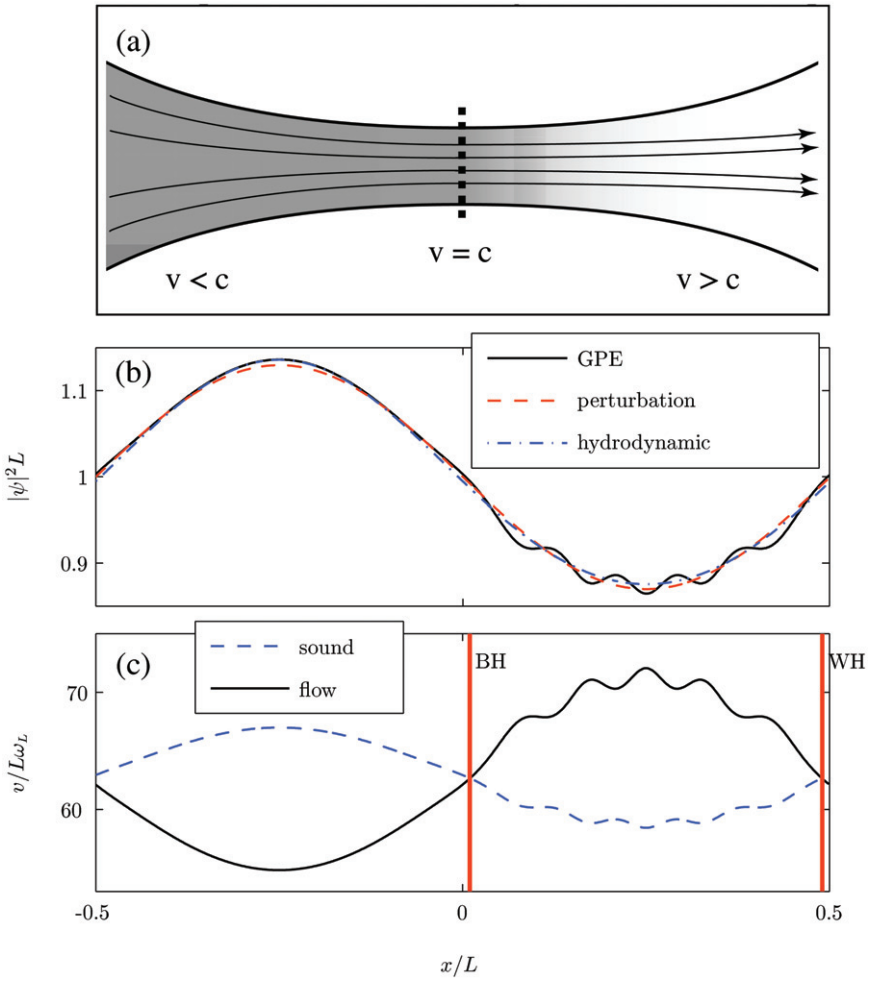

Figure 22. Stationary flow in a doubly constricted toroid potential. (a) Schematic of a hydrodynamic de Laval nozzle. A flow that attains the speed of sound ($v = c$) at the narrowest point of the nozzle becomes supersonic beyond the nozzle. (b) Stationary GPE solution in a quasi-one-dimensional toroidal geometry perturbed by the potential (147), with winding number $w_0 = 10$ (other parameters are given in [164]). The full solution is compared with the results of hydrodynamic and perturbation theory approaches showing the importance of beyond hydrodynamic corrections in the supersonic region. (c) Flow velocity and sound velocity corresponding to the GPE solution of (b), showing the position of the black hole (BH) and white hole (WH) horizons for sound waves. The energy unit of the toroid is $\hbar\omega_L = \hbar^2/mL^2$. Reproduced with permission from [164]. Copyright © 2007 by The American Physical Society.

In regimes where only a pair of modes are coupled then $\hat{H}_2$ describes the formation of a two-mode squeezed state [12]. In this case, tracing over the negative energy mode, the density matrix for the positive energy state is of the form of that for a thermal state with mean occupation $\langle n \rangle_+ = \sinh^2 \gamma t$. This is analogous to the Hawking effect in that pairs of quasiparticles are produced at no energy cost: one enters the negative energy state (in the

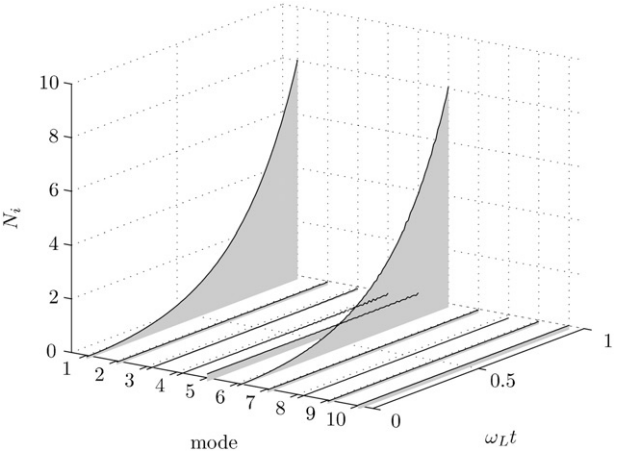

Figure 23. Mode populations from averaging 40 trajectories of the truncated Wigner evolutions for the quantum de Laval nozzle. Modes 1 and 6 are dynamically unstable, corresponding to the negative and positive energy modes respectively. Reproduced with permission from [164]. Copyright © 2007 by The American Physical Society.

supersonic regime) and the other is promoted to positive energy and emerges at the horizon.

While the Bogoliubov analysis is useful in predicting the regions of instability, it cannot describe the process dynamics, as the unstable modes grow exponentially (at least initially) and rapidly invalidate the linearized Bogoliubov analysis. Simulations with the truncated Wigner approach (see Figure 23) avoid such limitations as they include the non-linear interactions between excitations and their back-reaction. These features of the Wigner approach have seen several recent applications to the study of cosmological analogue models in BEC systems, such as particle production in an expanding universe [166], and studies of Hawking radiation [167].

In relation to the treatment of instabilities, also note the work of Polkovnikov [168] on the evolution of the macroscopically entangled states in optical lattices, where the truncated Wigner approach was used to deal with an unstable system where the usual Bogoliubov treatment breaks down. In that work the author presents arguments that this formalism should be able to adequately describe collapse and revival dynamics of the condensate.

Another application to quasiparticle dynamics was performed by Modugno *et al.* [169] who investigated the possibility of driving a parametric resonance in a toroidally trapped BEC. It was shown that specific quasiparticle modes could be resonantly excited, and then individually observed via expansion imaging. Starting from a zero-temperature BEC, the quasiparticle excitation was initiated from vacuum fluctuations present in the initial state of the Wigner representation and driven by modulating the trapping potential.

4.7. *Vortex formation in a stirred BEC*

A number of experiments have shown that rotationally stirring a low-temperature BEC can lead to the formation of a vortex lattice, e.g. [171–174]. In the most typical scenario,

the stirring excites a dynamical instability of the condensate [175], which is transformed into a highly turbulent state, and then after a long period evolves into a rotating state containing a regular vortex lattice. This system provides a challenging test for dynamical theories of cold bosonic gases, because while the process (ideally) involves only an initial pure ground state subject to a conserving (Hamiltonian) process, dissipation is required for the system to evolve into a state in equilibrium with the stirrer; see, e.g., [176,177]. A number of approaches have been given based either on the pure GPE, e.g. [178,179] or the GPE supplemented with phenomenological damping terms [176], but the description of the turbulent state is clearly beyond the validity of the GPE. An *a priori* description of the thermalization which is central to the process, and provides the necessary dissipation mechanism, was first given by Lobo *et al.* [180] using a classical field method. They simulated a three-dimensional condensate stirred by an elliptically perturbed rotating harmonic trap, and considered the case of an initial $T=0$ condensate (which they modelled as the ground state of the GP equation), and also the case of an initial finite temperature condensate. Their simulations for an initially $T=0$ condensate showed evolution similar to that seen in earlier approaches (e.g. [177–179]), with vortices eventually entering the high-density region of the field a few hundred trap cycles after the creation of the turbulent state. The vortices settle into an ordered lattice after another period of a few hundred trap cycles, and then the lattice slowly damps over a further period of about 1000 trap cycles. Lobo *et al.* made an approximate estimate of the total energy transferred irreversibly out of the condensate, and by assuming equipartition over the available modes, obtained a temperature of the thermal cloud which they assumed was responsible for the dissipation. More recently, Wright *et al.* [170] have treated this stirring problem using a TWPGPE approach. The initial vacuum noise gives an irreducible mechanism for seeding the dynamical instability, and their method ensures particle number and rotating frame energy are conserved to very high accuracy over the length of the simulation. Furthermore, the basis choice and numerical method they use is free from the grid method and boundary artifacts such as aliasing and spurious damping at high momenta, so that any thermalization and damping observed can be unambiguously attributed to the intrinsic field theory, rather than numerical artifact. The authors considered systems in 'pancake' traps, which are effectively two dimensional. A typical final state, after the system has been subjected to a constantly rotating elliptical perturbation for 3000 trap cycles, is shown in Figure 24(a).

This treatment allows a detailed and quantitative description of the thermalization of the condensate. The thermal cloud created is initially located primarily in an outer annulus, and quickly obtains a classical moment of inertia, while the central region of the field is irrotational until penetrated by vortices. The temperature and chemical potential of the thermal cloud are obtained by a self-consistent fit, and good agreement is obtained to an analytic estimate. The Penrose–Onsager criterion (see Section 3.2.4) for identifying the condensate component fails in this system, owing to the complex phase and amplitude structure associated with the vortex array. As an alternative method of characterizing the coherence properties of the system, the authors examine the local behaviour of the temporal power spectra of the classical field about time t_0, namely

$$H(\mathbf{x}, \omega; t_0) = \left| \frac{1}{T} \int_{t_0 - T/2}^{t_0 + T/2} \psi_{\mathbf{C}}(\mathbf{x}, t) e^{-i\omega t} \, \mathrm{d}t \right|^2 . \tag{149}$$

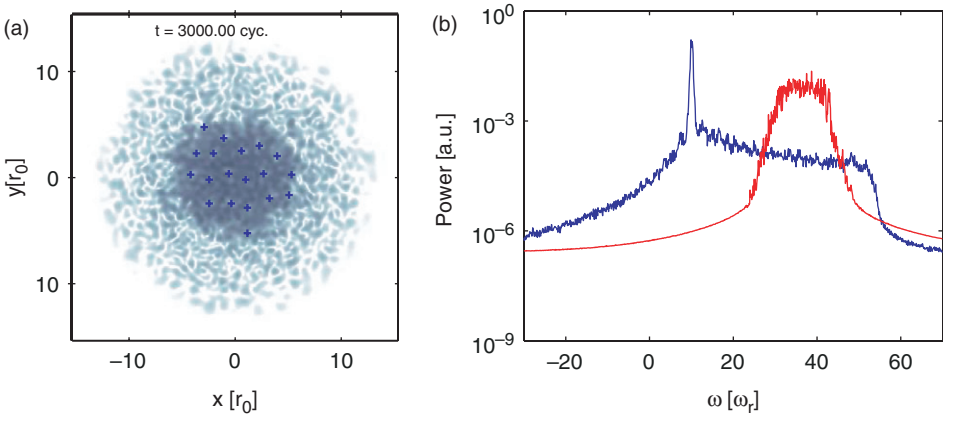

Figure 24. (a) Classical field density of the equilibrium state of stirred condensate. Vortices are indicated by + symbols, and are indicated only where the surrounding density of the fluid exceeds some threshold value. (b) Power spectral density traces at particular radii. The black (blue) and dark grey (red) lines correspond to radii $r = 3.1894 r_0$ and $r = 11.9575 r_0$, respectively. Data corresponds to the period $t = 9900$–9910 trap cycles. The plots in (a) and (b) are from the same simulation, in which the condensate was initially in a trap of frequency ω_r, at temperature $T = 0$, chemical potential $\mu_i = 14\hbar\omega_r$. The elliptical perturbation rotates continuously at $\Omega = 0.75\omega_r$. The spatial scale is the oscillator length $r_0 = \sqrt{\hbar/m\omega_r}$. Colour refers to the online version. Reproduced with permission from [170]. Copyright © 2008 by The American Physical Society.

The sampling period T is chosen to be a number of trap cycles, and is long compared with the timescales characterizing the phase evolution of the condensate ($\hbar/\mu$), but short compared with the relaxation time of the field. Spectra such as those shown in Figure 24(b) are obtained. The spectrum from the central region of the field has a prominent and narrow peak at $\omega \approx 10\omega_r$, which is interpreted as the condensate eigenvalue. At larger radii ($r \gtrsim 9r_0$) the spectrum is broadened and is approximately that of the non-interacting gas. The local correlation times obtained from these data (by Fourier transform of H) allow an unambiguous distinction to be made between superfluid turbulence and thermal gas (which has a much shorter correlation time). We note that a feature of the two-dimensional system is that the final state is not a regular Abrikosov lattice, but instead is a spatially disordered vortex liquid state. This can be interpreted as a thermally excited vortex lattice, and indeed both the simulations and an analytic prediction given in [170] show that a considerable amount of thermal energy is generated in the stirring process, and that therefore the final condensate state must have considerable thermal excitation. The final state of the simulations is consistent with the condensate being in thermal and rotational equilibrium with the thermal cloud.

4.8. *Quantum statistical effects in superchemistry*

The field of *superchemistry* was defined by Heinzen *et al.* [181] as 'the coherent stimulation of chemical reactions via macroscopic occupation of a quantum state by a bosonic chemical species'. Truncated Wigner simulations were used by Olsen *et al.* [27,28,182–184]

to investigate superchemistry based on photoassociation of trapped BECs into molecular dimers. The atom–molecule coupling occurs through a Raman two-photon transition for which the interaction Hamiltonian can be written as [28]

$$\hat{H}_{\rm int} = \frac{i}{2}\int d^3\mathbf{x}\chi(\mathbf{x})\Big(\hat{\psi}_a^{\dagger 2}(\mathbf{x})\hat{\psi}_{m^*}(\mathbf{x}) - \hat{\psi}_a^2(\mathbf{x})\hat{\psi}_{m^*}^\dagger(\mathbf{x})\Big) + i\int d^3\mathbf{x}\Omega(\mathbf{x})\Big(\hat{\psi}_{m^*}^\dagger(\mathbf{x})\hat{\psi}_m(\mathbf{x}) - \hat{\psi}_{m^*}(\mathbf{x})\hat{\psi}_m^\dagger(\mathbf{x})\Big), \tag{150}$$

where $\hat{\psi}_a(\mathbf{x})$ is the atomic field, $\hat{\psi}_{m^*}(\mathbf{x})$ the excited molecular field and $\hat{\psi}_m(\mathbf{x})$ is the molecular ground-state field. Here $\chi(\mathbf{x})$ is the Rabi frequency of the transition from atoms to excited molecules and $\Omega(\mathbf{x})$ is the Rabi frequency for the transition from excited to ground molecular states.

A notable feature of this work was the departure from the mean-field predictions (see also [185]). The quadratic dependence of (150) on atomic fields combined with the relatively short timescale of the atom–molecule transition combine to make the process highly sensitive to quantum statistical effects such as squeezing (see, e.g., Figure 3 for a comparison of some different quantum states for the condensate). Results of those studies demonstrated a regime where the quantum statistics of the atomic condensate play a crucial role in superchemistry dynamics and confirmed that photoassociation of a trapped BEC into molecules provides a signature of the quantum state of the BEC. This can be seen in Figure 25 where photoassociation dynamics are compared for different quantum states of the initial BEC.

4.9. *The quantum linewidth of an atom laser*

Johnsson and Hope [186] used the TWA to model the process of weak outcoupling from a trapped BEC and to determine the linewidth of the outcoupled beam. Semi-classical

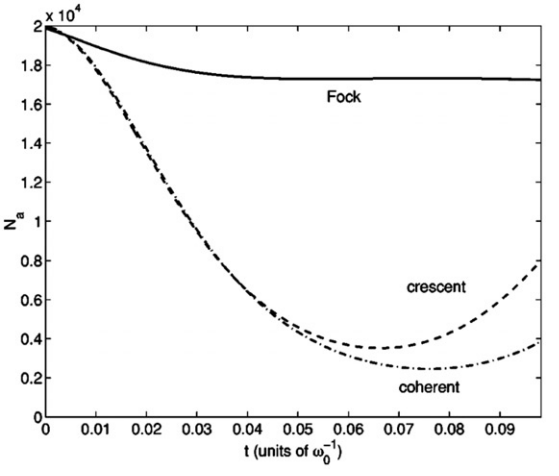

Figure 25. Comparison of atom number in photoassociation dynamics for Fock (solid line), coherent (dash-dot) and crescent quantum states of the initial atomic BEC. Reproduced with permission from [27]. Copyright © 2004 by The American Physical Society.

analysis predicts the linewidth will be essentially Fourier limited, scaling as the inverse of the outcoupling time [187]. Determining the quantum linewidth requires a multimode quantum theory of the atom laser outcoupler which the was implemented using the TWA. For Raman transition-based outcouplers the primary source of linewidth broadening in the weak outcoupling regime comes from phase fluctuations of the condensate. The main source of phase fluctuations is the non-linear interactions in the condensate which convert number fluctuations into phase fluctuations [188]. A simple estimate for the quantum linewidth, ΔE, of the output coupled atom laser beam from condensate containing N_0 atoms in a harmonic trap is given by

$$\Delta E = \frac{\partial \mu_{\mathrm{TF}}}{\partial N_0} \Delta N_0, \tag{151}$$

where μ_{TF} is the Thomas–Fermi chemical potential (see Equation (103)). If the quantum state of the BEC is approximately a coherent state then the fluctuations in condensate number are Poissonian, i.e. $\Delta N_0 = \sqrt{N_0}$, and an analytic expression for ΔE can be calculated.

In [186] one- and two-dimensional truncated Wigner simulations were used to obtain the atom laser linewidth as a function of output coupling time, and these results were compared against GPE simulations. For short times the linewidth was found to be inversely proportional to the output coupling time, a feature adequately described by the GPE. However, on longer timescales the linewidth predictions of the two theories differed: the truncated Wigner simulations plateaued towards the Poissonian limit (151), whereas the GPE continued to narrow.

5. The SPGPE

The SPGPE is a truncated Wigner theory of Bose gases which takes into account the interactions between the atoms in the c-field region and the **I** region. The theory is valid for sufficiently large systems for temperatures from about $0.5T_{\mathrm{c}}$ to just above the BEC transition at $T = T_{\mathrm{c}}$ when the **I** region contains many weakly populated thermal modes. For a trapped system with largest trap frequency ω the condition $\hbar\omega \ll k_{\mathrm{B}}T$ must be satisfied; in this sense it is a high-temperature theory, extending the PGPE theory treated in Section 3 and complimenting the low-temperature TWPGPE approach described in Section 4. An important point of difference is that the SPGPE theory is a grand canonical theory, in contrast to the microcanonical approaches described in previous sections. In its simplest implementation the theory is parameterized by the (in general, time-dependent) temperature T and chemical potential μ of the thermal reservoir comprising the thermally occupied modes contained in the **I** region. Thus, in contrast to microcanonical approaches for which temperature must be determined *a posteriori*, the SPGPE formalism allows direct control of the temperature of the interacting system. In general, the **I** and **C** regions may be out of equilibrium (such as during quench cooling towards T_{c}). The dynamics of the condensation process are particularly well suited to treatment with this theory.

5.1. *Formalism*

The treatment of thermal processes using stochastic methods has a long history, beginning with the theory of Brownian motion [189,190]. The theory of open *quantum* systems

couples the modes of interest in the quantum system to a reservoir [11]. The precise details of the derivation can be found in [8,26,191,192]. As a full treatment is rather lengthy, here we briefly outline the development of the theory.

The essential conditions for a treatment of the degenerate Bose gas with minimal complexity are (i) the system and the reservoir are uncorrelated and (ii) the reservoir is in *local equilibrium*, described by the semiclassical Bose–Einstein distribution. In many systems of interest these conditions can be readily satisfied by appropriately choosing the cutoff energy $\epsilon_{\rm cut}$. In essence, the SPGPE theory extends the PGPE theory by including the coupling of **C** region atoms with atoms in **I** which form a grand-canonical reservoir. The coupling generates additional damping and stochastic terms in the PGPE, which necessarily takes the form of a SDE.

The assumption of local equilibrium for the **I** region is convenient, but does not pose a fundamental limitation of the formalism. In principle, it is possible to derive a quantum Boltzmann-like kinetic equation for the particles in **I** coupled to a stochastic c-field equation for the particle in **C**. However, this would result in further computational complexity which is not necessary for a broad range of applications. Such a description remains a goal for the future, and would result in a near-complete model of Bose gas dynamics at high temperature.

5.1.1. *Background*

The theory of finite temperature BEC dynamics of Zaremba *et al*. [193], which was developed along the lines of the two-fluid theory of superfluid helium, provided the foundations for generalized GPE theory from a hydrodynamic point of view. The essential assumption of the theory is that atoms enter and leave the condensate so as to enforce *local* energy and momentum conservation. The resulting description takes the form of a finite-temperature GPE for the condensate, coupled to a Boltzmann equation for the non-condensate. The theory has the advantage that the condensate and non-condensate are described on an equal footing, making the description of coupled dynamics of thermal cloud and condensate tractable. While being intuitively appealing and a providing a powerful approach for extending zero-temperature mean-field theory, enforcing local conservation of energy and momentum also has disadvantages which are removed by the SPGPE approach. First, as a mean-field theory it cannot be valid near the BEC phase transition where the condensate is relatively small or non-existent. Furthermore, a locally conserving theory neglects the non-locality of quantum mechanics, which plays a fundamental role in determining the dynamics of atoms stimulated into a highly occupied field.

The SGPE formulation of Stoof is closely related to the SPGPE theory presented here: the formulation leads to a SDE for the condensate which is driven by a noise term associated with condensate growth. However, there are two important differences. First, in [194] the reservoir is chosen to contain all modes with energy in excess of the chemical potential μ. The stochastic GPE so-obtained involves self-energy functions, necessitating a many-body T-matrix treatment of interactions. As well as being difficult to implement numerically, the c-field of the theory only describes the condensate and few very low-energy excitations. As discussed in Section 3.1.2, in the vicinity of the transition there are typically 10^3–10^4 degenerate modes warranting a c-field treatment. Second, the approach neglects scattering terms which conserve population but transfer

energy from the reservoir to the c-field region. The inclusion of these terms in the SPGPE stems from the explicit use of a high-energy projector, which renders them finite and tractable.

SPGPE. The quantum kinetic theory of Bose–Einstein condensation [195–197] has been shown to provide a good description of the process of condensate formation [198–200] at the level of condensate population dynamics provided condensation occurs into the absolute ground state of the system. Recent work by Gardiner *et al.* [8,26,46,191,192] developed the SPGPE theory to explicitly include a high-energy cutoff, thus unifying the PGPE theory with the reservoir theory of high-temperature BECs.

Since its inception, the theory of finite-temperature BECs has presented many challenges and a rich body of work has accumulated [22]. Several key problems are the consistent treatment of two-body interactions [20,23], the description of thermal cloud coupling and dynamics [193,194] and the unification of GPE approaches with dissipative finite-temperature phenomenology [176,201]. In these respects, the SPGPE theory has some notable computational and physical advantages which we briefly summarize as follows.

(i) *Consistent UV-cutoff*. The imposition of a high-energy cutoff using the methods of Section 3 imposes a consistent cutoff, even for trapped systems. As noted in Section 3.1.1, if the cutoff is only imposed in momentum space the precise wavelength for the cutoff is position dependent. The PGPE formalism addresses this problem by imposing a cutoff in the single-particle basis which approximately diagonalizes the many-body Hamiltonian at high energies.

(ii) *Two-body T-matrix*. By imposing the cutoff at high energies the need to use the many-body T-matrix to describe scattering is eliminated, requiring only the two-body T-matrix description of S-wave scattering: $T(0) \to 4\pi\hbar^2 a/m$.

(iii) *Non-local description of condensate growth*. Fundamentally the theory is non-local: atoms which leave the high-energy cloud enter the c-field region so as to minimize the difference between the chemical potential of the high-energy region and the GPE operator acting on the c-field. Beyond hydrodynamic effects are thus explicitly included.

(iv) *Scattering terms*. Imposing a cutoff at high energies allows the so-called *scattering* terms, reservoir interactions that do not directly change the populations of the reservoir or c-field, to be consistently included in the theory. Analogous terms proved to play an important role in the quantum kinetic theory description of condensate growth [202]. In the SPGPE theory, the scattering terms couple to dynamical excitations in the c-field region.

(v) *Valid at the BEC transition*. A notable feature of the SPGPE is that it is particularly well suited for dynamical studies in the regime $T \sim T_c$ since the conditions of validity are *high temperature* ($\hbar\bar{\omega} \ll k_B T$) and moderate occupation of modes, both of which are readily satisfied near the BEC transition.

(vi) *Reservoir dynamics*. In principle, the dynamics of the incoherent region can be treated with a quantum Boltzmann equation with little additional formalism provided the region remains in approximate local equilibrium.

(vii) *Consistent mean-field treatment of dissipation*. The mean-field theory recovered by setting all noises to zero gives a GPE of motion with extra dissipative terms. The dissipation evolves the c-field to a ground state with the chemical potential of

the reservoir. In contrast to phenomenological approaches [176,201], the dissipation rate arising in the equation of motion is the physical rate of the theory which can be derived from a Boltzmann integral[7] [192].

5.1.2. *The system and its separation*

We again consider a dilute Bose gas held in a trapping potential defined by (3), but extend the PGPE description of Section 3 to consider the coupling of the c-field region to the **I** region. To accommodate applications such as the formation of vortex lattices in BECs (discussed below in Section 5.4), we include the possibility that the **I** region may be rotating. This requires either that the trapping potential is axially symmetric, or time-independent in a rotating frame of reference (corresponding to elliptical stirring at a constant angular frequency). For simplicity we restrict our attention to systems where either (i) the **I** region is stationary in the laboratory frame or (ii) the **I** region is rotating in an axially symmetric trap. For the latter case the theory is conveniently formulated in the frame rotating at the frequency of the **I** region, which we denote by Ω. Choosing the symmetry axis of the system to be the z-axis, the single-particle Hamiltonian for the system transformed to the rotating frame is

$$H_{\rm sp} = H_0 = -\frac{\hbar^2\nabla^2}{2m} + V_0(\mathbf{x}) - \Omega L_z, \tag{152}$$

where $L_z = -\mathrm{i}\hbar(x\partial_y - y\partial_x)$ is the z-component of the angular momentum operator. It has been shown that when the incoherent region is in rotational equilibrium in a harmonic trap the theory is modified by transforming the c-field description to the rotating frame and making the replacement $\omega_r \to \omega_\perp$, where

$$\omega_\perp = \sqrt{\omega_r^2 - \Omega^2}, \tag{153}$$

in the dissipation rates of the SPGPE [192]. We can thus treat the rotating case in the formalism by including the effects of rotating frame transformation in the c-field description (152), parameterized by Ω. We return to rotating systems in more detail in Section 5.4.3, but in what follows the formalism applies to systems that are either non-rotating and in general non-axisymmetric, or rotating and axisymmetric ($\omega_x = \omega_y \equiv \omega_r$).

As described in Section 2.2, the field operator for the full system is decomposed into a c-field and an incoherent field. The SGPE takes the form of an equation of motion for the c-field $\psi_{\mathbf{C}}(\mathbf{x})$ with terms arising from interaction with the incoherent region **I**. The two regions are treated using different approximations.

5.1.3. *Treatment of the incoherent region*

The local equilibrium assumption for the state of the incoherent region allows all higher-order correlation functions arising in the theory to be factorized into products of second-order correlation functions. At this level of approximation the essential reservoir interaction physics can be reduced to functions of the single-particle Wigner function

for the incoherent region

$$F_{\mathbf{I}}(\mathbf{x},\mathbf{K}) = \int d^3\mathbf{x}' \left\langle \hat{\psi}_{\mathbf{I}}^{\dagger}(\mathbf{x}+\mathbf{x}'/2)\hat{\psi}_{\mathbf{I}}(\mathbf{x}-\mathbf{x}'/2)\right\rangle e^{i\mathbf{K}\cdot\mathbf{x}'}, \tag{154}$$

previously introduced in Section 3.2.6. Introducing the variables $\mathbf{u} \equiv (\mathbf{x}+\mathbf{x}')/2$, $\mathbf{v} \equiv \mathbf{x}'-\mathbf{x}$, we can write

$$\begin{aligned}\langle \hat{\psi}_{\mathbf{I}}^{\dagger}(\mathbf{x}')\hat{\psi}_{\mathbf{I}}(\mathbf{x},\tau)\rangle &= \langle \hat{\psi}_{\mathbf{I}}^{\dagger}(\mathbf{u}+\mathbf{v}/2)\hat{\psi}_{\mathbf{I}}(\mathbf{u}-\mathbf{v}/2,\tau)\rangle, \\ &\approx \frac{1}{(2\pi)^3}\int_{\Omega_{\mathbf{I}}} d^3\mathbf{K}\, F_{\mathbf{I}}(\mathbf{u},\mathbf{K}) e^{-i\mathbf{K}\cdot\mathbf{v}-i\omega(\mathbf{u},\mathbf{K})\tau},\end{aligned} \tag{155}$$

$$\langle \hat{\psi}_{\mathbf{I}}(\mathbf{x}')\hat{\psi}_{\mathbf{I}}^{\dagger}(\mathbf{x},\tau)\rangle \approx \frac{1}{(2\pi)^3}\int_{\Omega_{\mathbf{I}}} d^3\mathbf{K}\,[1+F_{\mathbf{I}}(\mathbf{u},\mathbf{K})] e^{i\mathbf{K}\cdot\mathbf{v}+i\omega(\mathbf{u},\mathbf{K})\tau}, \tag{156}$$

where phase-space integration over the incoherent region $\Omega_{\mathbf{I}}$ constrains the coordinates to satisfy $\hbar\omega(\mathbf{x},\mathbf{K}) > \epsilon_{\mathrm{cut}}$ (see (124) and (127)) and the energy in the frame rotating with angular frequency vector $\mathbf{\Omega} = \Omega\hat{z}$ has the semiclassical form

$$\hbar\omega(\mathbf{x},\mathbf{K}) = \frac{\hbar^2\mathbf{K}^2}{2m} - \hbar\mathbf{\Omega}\cdot(\mathbf{x}\times\mathbf{K}) + V_0(\mathbf{x}). \tag{157}$$

The dissipation rates of the theory are time-integrated products of such functions, as can be seen from (171) and (174).

Semi-classical Bose–Einstein distribution. For many applications the **I** region may be described by a semiclassical Bose–Einstein distribution

$$F_{\mathbf{I}}(\mathbf{x},\mathbf{K}) = \frac{1}{\exp[(\hbar\omega(\mathbf{x},\mathbf{K})-\mu)/k_{\mathrm{B}}T]-1}, \tag{158}$$

where we note that for high energies where this is assumed to apply, the gas is always rapidly thermalized and interactions with the c-field region are a small correction to the single-particle energy (157). This form has been used to evaluate the dissipation rates of the SPGPE theory [192].

The properties of the ideal gas description of (158) and (157), including the effect of the cutoff, can be expressed in terms of the incomplete Bose–Einstein function defined as [192]

$$\begin{aligned} g_\nu(z,y) &\equiv \frac{1}{\Gamma(\nu)}\int_y^\infty \mathrm{d}x\, x^{\nu-1}\sum_{l=1}^{\infty}(ze^{-x})^l, \\ &= \sum_{l=1}^{\infty}\frac{z^l}{l^\nu}\frac{\Gamma(\nu,yl)}{\Gamma(\nu)}, \end{aligned} \tag{159}$$

where $\Gamma(\nu,x) \equiv \int_x^\infty \mathrm{d}y\, y^{\nu-1}e^{-y}$ is the incomplete Gamma function. In analogy with the reduction to an ordinary Gamma function $\Gamma(\nu,0) = \Gamma(\nu)$, we have

$g_\nu(z,0) = g_\nu(z) \equiv \sum_{l=1}^{\infty} z^l/l^\nu$, reducing to the ordinary Bose–Einstein function. We then find for the **I** region density, for example

$$\begin{aligned} n_{\mathbf{I}}(\mathbf{x}) &= \int_{\Omega_{\mathbf{I}}} \frac{d^3\mathbf{k}}{(2\pi)^3} F_{\mathbf{I}}(\mathbf{x},\mathbf{k}) \\ &= \lambda_{\mathrm{dB}}^{-3} g_{3/2}\left(e^{\beta[\mu - V_\perp(\mathbf{x})]}, \beta\hbar^2 K_{\mathrm{cut}}(\mathbf{x})^2/2m\right), \end{aligned} \tag{160}$$

where $\hbar^2 K_{\mathrm{cut}}(\mathbf{x})^2/2m = \max\{\epsilon_{\mathrm{cut}} - V_\perp(\mathbf{x}), 0\}$ and we have introduced the effective potential

$$V_\perp(\mathbf{x}) = \frac{m}{2}(\omega_\perp^2 r^2 + \omega_z^2 z^2), \tag{161}$$

which accounts for the transformation to the rotating frame (153). Setting $\epsilon_{\mathrm{cut}} = 0$, we recover the standard form for the semiclassical particle density of the ideal gas [57]. The total number in **I** region is given by

$$N_{\mathbf{I}} = g_3\left(e^{\beta\mu}, \beta\epsilon_{\mathrm{cut}}\right)/(\beta\hbar\bar{\omega})^3, \tag{162}$$

where $\bar{\omega} = (\omega_z\omega_\perp^2)^{1/3}$ is the geometric mean frequency in the rotating fame. In this way the usual semiclassical expressions can be generalized to include a cutoff in terms of the incomplete Bose–Einstein function.

5.1.4. *Treatment of the c-field region: deriving the equation of motion*

The standard procedure of phase-space methods for open systems involves deriving a master equation for the reduced system by eliminating the reservoir degrees of freedom. The master equation may then be mapped to a generalized FPE of motion for a quasi-probability distribution, such as the Wigner representation, by making use of operator correspondences (e.g. (52)–(55)). Provided that the FPE contains derivatives which are at most second order (representing diffusion), an equivalent SDE may be found which can be conveniently simulated numerically. The TWA involves neglecting third-order terms in the FPE (see (58)), and in the context of the SPGPE theory the TWA reduces the FPE to second order, allowing a formulation of the problem in terms of SDEs.

Validity of the SPGPE treatment of the c-field. In addition to treating the **I** region semiclassically, the SPGPE formalism makes the TWA which requires that the modes under consideration are highly occupied. An approximate master equation that can be mapped to a SDE is then obtained by truncating the interaction between **C** and **I** at first order in powers of $\hbar\omega/k_{\mathrm{B}}T$, where $\omega = \max\{\omega_i\}$ is the largest oscillator frequency of the system.

A feature of the high-temperature theory is that the dissipation arising from the reservoir coupling acts to smooth out sharp phase-space structure that would otherwise generate significant third-order term corrections [203]. In this sense the high-temperature Bose gas is particularly well suited to treatment using the truncated Wigner method.

5.1.5. *SPGPE*

In the rotating frame the full non-local form of the SPGPE is given by the following SDE in Stratonovich form

$$(S)\mathrm{d}\psi_{\mathbf{C}}(\mathbf{x},t) = \mathcal{P}_{\mathbf{C}}\Big\{ -\frac{i}{\hbar}L_{\mathbf{C}}\psi_{\mathbf{C}}(\mathbf{x})\mathrm{d}t \tag{163a}$$

$$+\frac{G(\mathbf{x})}{k_{\mathrm{B}}T}(\mu - L_{\mathbf{C}})\psi_{\mathbf{C}}(\mathbf{x})\mathrm{d}t + dW_G(\mathbf{x},t) \tag{163b}$$

$$+\int d^3\mathbf{x}' M(\mathbf{x}-\mathbf{x}')\frac{i\hbar\nabla\cdot\mathbf{j}_{\mathbf{C}}(\mathbf{x}')}{k_{\mathrm{B}}T}\psi_{\mathbf{C}}(\mathbf{x})\mathrm{d}t + i\psi_{\mathbf{C}}(\mathbf{x})\,dW_M(\mathbf{x},t)\Big\}. \tag{163c}$$

The first line of the SPGPE (163a) describes Hamiltonian evolution according to the PGPE introduced in Section 2.3.6 and developed in Section 3. The projector $\mathcal{P}_{\mathbf{C}}$ appears as a natural consequence of formally imposing a high-energy cutoff in the definition of the c-field region. The operator $L_{\mathbf{C}}$ is the Hamiltonian evolution operator for the c-field region defined via Equations (65) and (67). Its explicit form is

$$L_{\mathbf{C}}\psi_{\mathbf{C}}(\mathbf{x}) \equiv \left(H_{\mathrm{sp}} + u|\psi_{\mathbf{C}}(\mathbf{x},t)|^2\right)\psi_{\mathbf{C}}(\mathbf{x}). \tag{164}$$

The second line of the SPGPE (163b) is directly responsible for condensate growth from scattering between two **I** region atoms as illustrated in Figure 26(a). The μ and T that arise are respectively the chemical potential and temperature of the thermal reservoir of particles in the **I** region. The quantity $G(\mathbf{x})$ is a spatially dependent collision rate, specified by a quantum Boltzmann integral over the **I** region as discussed in more detail in Section 5.2.1 below. The complex noise associated with growth is $dW_G(\mathbf{x}',t)$ and satisfies

$$\langle dW_G^*(\mathbf{x},t)\,dW_G(\mathbf{x}',t)\rangle = 2G(\mathbf{x})\delta_C(\mathbf{x},\mathbf{x}')\mathrm{d}t, \tag{165}$$

$$\langle dW_G(\mathbf{x},t)\,dW_G(\mathbf{x}',t)\rangle = \langle dW_G^*(\mathbf{x},t)\,dW_G^*(\mathbf{x}',t)\rangle = 0. \tag{166}$$

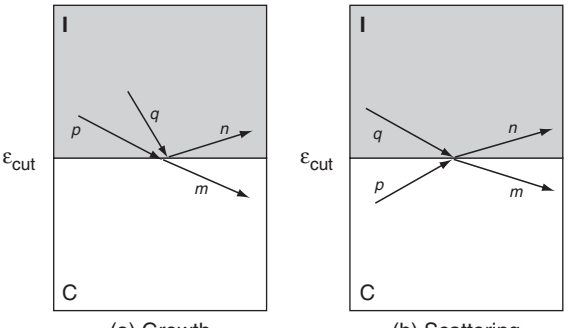

Figure 26. Schematic of the processes arising from the interactions between the c-field and incoherent regions. (a) Two c-field region atoms collide, with a significant fraction of the collision energy transferred to one of the atoms, with the other atom passing into the c-field region. The time-reversed process also occurs. (b) A c-field region atom collides with a incoherent region atom with no change in c-field region population.

The third line of the SPGPE (163c) represents number-conserving scattering processes between atoms in **C** and **I** and provides a mechanism for energy transfer between the two regions as illustrated in Figure 26(b). This couples to the divergence of the c-field region current given by

$$\mathbf{j}_{\mathbf{C}}(\mathbf{x}) \equiv \frac{i\hbar}{2m}\left([\nabla\psi^*_{\mathbf{C}}(\mathbf{x})]\psi_{\mathbf{C}}(\mathbf{x}) - \psi^*_{\mathbf{C}}(\mathbf{x})\nabla\psi_{\mathbf{C}}(\mathbf{x})\right) - (\mathbf{\Omega}\times\mathbf{x})|\psi_{\mathbf{C}}(\mathbf{x})|^2, \tag{167}$$

where the last line is a rigid-body rotation term arising from the transformation to the rotating frame. The limit $\boldsymbol{j}_{\mathbf{C}}(\mathbf{x}) = 0$ gives the laboratory frame velocity field $\mathbf{v} = \mathbf{\Omega}\times\mathbf{x}$, corresponding to the irrotational system mimicking rigid-body rotation. The rate function $M(\mathbf{x}-\mathbf{x}')$ is specified by a second quantum Boltzmann integral, and is discussed in detail below in Section 5.2.2.

The real noise $dW_M(\mathbf{x}, t)$ associated with scattering is specified by

$$\langle dW_M(\mathbf{x}, t)\, dW_M(\mathbf{x}', t)\rangle = 2M(\mathbf{x}-\mathbf{x}')\mathrm{d}t. \tag{168}$$

Grand canonical equilibrium. As described in Section 3.2.4, the PGPE provides a means to sample the microcanonical ensemble of equilibrium states. By including interactions with the incoherent region we have arrived at a grand canonical description, parameterized by the chemical potential and temperature of **I**. Irrespective of the form of $G(\mathbf{x})$ and $M(\mathbf{x})$, the SPGPE evolves the system to the grand canonical equilibrium distribution

$$W_s \propto \exp\left(\frac{\mu N_{\mathbf{C}} - H_{\mathbf{C}}}{k_{\mathrm{B}}T}\right), \tag{169}$$

corresponding to the density matrix

$$\hat{\rho}_s \propto \exp\left(\frac{\mu \hat{N}_{\mathbf{C}} - \hat{H}_{\mathbf{C}}}{k_{\mathrm{B}}T}\right), \tag{170}$$

in the TWA. Once the c-field reaches equilibrium single trajectories may be used to sample the grand canonical ensemble.

5.2. *Growth and scattering in the SPGPE*

We now discuss the properties of the dissipative terms in the SPGPE (163). We give the explicit form of the rate functions $G(\mathbf{x})$ and $M(\mathbf{x})$, the regimes under which they may be evaluated in closed form, and discuss details of their physical interpretation.

5.2.1. *Growth terms*

Growth rate. The explicit form of the growth rate is [8,192]

$$G(\mathbf{x}) \equiv \frac{u^2}{(2\pi)^5\hbar^2}\int\int\int_{\Omega_{\mathbf{I}}} d^3\mathbf{K}_1\, d^3\mathbf{K}_2\, d^3\mathbf{K}_3\, F(\mathbf{x}, \mathbf{K}_1)F(\mathbf{x}, \mathbf{K}_2) \times [1 + F(\mathbf{x}, \mathbf{K}_3)]\Delta_{123}(0, 0), \tag{171}$$

where $\Delta_{123}(\mathbf{k}, \epsilon) \equiv \delta(\mathbf{K}_1 + \mathbf{K}_2 - \mathbf{K}_3 - \mathbf{k})\delta(\omega_1 + \omega_2 - \omega_3 - \epsilon/\hbar)$ conserves energy and momentum during the collision.

The rate $G(\mathbf{x})$ can be calculated in the regime where the **I** region is quasi-static, and well-approximated by an ideal semiclassical Bose–Einstein distribution (158) with slowly varying $\mu(t)$ and $T(t)$. For the inner spatial region of a harmonic trap satisfying $V(\mathbf{x}) \leq 2E_R/3$ we find that $G(\mathbf{x}) \equiv \gamma$ is independent of position with

$$\gamma = \gamma_0 \left\{ \left[\ln\left(1 - e^{\beta(\mu-\epsilon_{\rm cut})}\right)\right]^2 + e^{2\beta(\mu-\epsilon_{\rm cut})} \sum_{r=1}^{\infty} e^{r\beta(\mu-2\epsilon_{\rm cut})} \left(\Phi[e^{\beta(\mu-\epsilon_{\rm cut})}, 1, r+1]\right)^2 \right\}, \qquad (172)$$

where $\gamma_0 = 4m(ak_{\rm B}T)^2/\pi\hbar^3$ and $\Phi[x, y, z]$ is the Lerch transcendent. Outside this region there is a weak spatial dependence which can be neglected for most purposes [192]. The bare rate, γ_0, has been used as an estimate in the literature, often requiring a 'fudge factor' (usually chosen as about three) to obtain a rate that gives physically reasonable damping times. In Figure 27 we show γ for a fixed choice of $\epsilon_{\rm cut} = 3\mu$. The full picture is more complicated than shown in Figure 27 because the choice $\epsilon_{\rm cut} = 3\mu$ would not be appropriate near $T_{\rm c}$, but instead a much higher $\epsilon_{\rm cut}$ would be necessary. In practice, the more accurate form typically increases the ratio γ/γ_0 by a factor which is in the range 1–10.

Dissipative dynamics of condensate growth. By neglecting the scattering and noise terms in the SPGPE (163) it is possible to show that

$$\frac{\partial(H_{\mathbf{C}} - \mu N_{\mathbf{C}})}{\partial t} = -\frac{2\gamma}{\hbar} \int d^3\mathbf{x} |(\mu - L_{\mathbf{C}})\psi_{\mathbf{C}}(\mathbf{x}, t)|^2, \qquad (173)$$

where we used the approximation $G(\mathbf{x}) \approx \gamma$ as given by Equation (172). As the right-hand side of Equation (173) is a strictly non-positive term, we can see that the growth term acts to minimize the effective grand-canonical Hamiltonian $K_{\mathbf{C}} \equiv H_{\mathbf{C}} - \mu N_{\mathbf{C}}$. The equilibrium solution is the ground state of the PGPE (68) with chemical potential μ. The growth terms describe the Bose-stimulated transfer of particles between the **C** and **I** regions during two-body collisions.

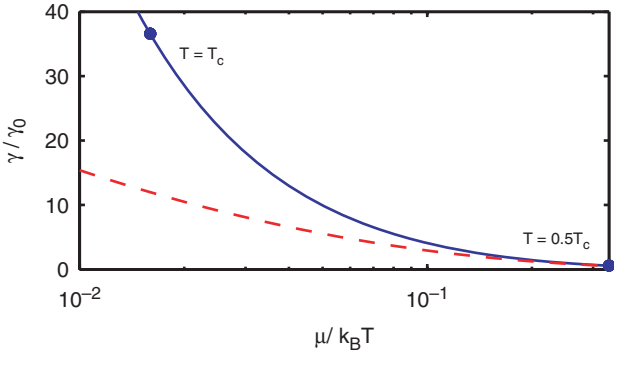

Figure 27. Dependence of the growth rate γ (172) on μ for the choice $\epsilon_{\rm cut} = 3\mu$. The full rate (172) (solid line) is compared with the logarithmic term (dashed line). The two points are calculated for $N = 10^6$ ^{87}Rb atoms in a trap with geometric mean frequency $\bar{\omega} = 2\pi \times 25$ Hz using the ideal gas relation for $T_{\rm c}$. The chemical potentials are estimated from $\mu \approx 3\hbar\bar{\omega}/2$ at $T = T_{\rm c}$, and $\mu \approx \mu_{\rm TF}(N_0)$ at $T = 0.5T_{\rm c}$.

5.2.2. *Scattering terms*

Scattering rate. The rate function for the scattering term of the SPGPE (163) is most easily calculated by transforming to momentum space $M(\mathbf{x}) = \int d^3\mathbf{k}\, e^{-i\mathbf{k}\cdot\mathbf{x}}\tilde{M}(\mathbf{k})$, where we find

$$\tilde{M}(\mathbf{k}) = \frac{2u^2}{(2\pi)^5\hbar^2}\int\int_{\Omega_\mathrm{I}} d^3\mathbf{K}_1\, d^3\mathbf{K}_2\, \Delta_{12}(\mathbf{k},0)F(\mathbf{u},\mathbf{K}_1)[1+F(\mathbf{u},\mathbf{K}_2)], \tag{174}$$

with $\Delta_{12}(\mathbf{k},\epsilon) \equiv \delta(\omega_1+\omega_2-\epsilon/\hbar)\delta(\mathbf{K}_1+\mathbf{K}_2-\mathbf{k})$. It has been shown that to a good approximation that this expression is independent of $\mathbf{u}$ (see [8,192]), and for this reason we suppress the argument in the present definitions.

Using the same approximation of a quasi-static thermal cloud as used in the calculation of the rate $G(\mathbf{x})$ in the previous section we find that

$$\tilde{M}(\mathbf{k}) = \frac{16\pi a^2 k_\mathrm{B}T}{(2\pi)^3\hbar|\mathbf{k}|}\frac{e^{\beta(E_R-\mu)}}{(e^{\beta(E_R-\mu)}-1)^2} \equiv \frac{\mathcal{M}}{(2\pi)^3|\mathbf{k}|}, \tag{175}$$

and, thus,

$$M(\mathbf{x}) = \frac{\mathcal{M}}{(2\pi)^3}\int d^3\mathbf{k}\,\frac{e^{-i\mathbf{k}\cdot\mathbf{x}}}{|\mathbf{k}|}. \tag{176}$$

so that $M(\mathbf{x})$ is a spatially dependent function over the whole $\mathbf{C}$ region. At first glance this term appears somewhat pathological, but well-defined results are obtained since $M(\mathbf{x})$ is convolved with functions of condensate band fields. Such functions are both UV and infrared cutoffs, giving a finite result for the convolution in (163c).

Effect of scattering on hydrodynamic collective modes. To gain some physical insight into the nature of the scattering we note that the evolution according to the deterministic part of (163c) can be written as a real effective potential

$$i\hbar\frac{\partial\psi_\mathbf{C}(\mathbf{x},t)}{\partial t}\bigg|_M = \mathcal{P}_\mathbf{C}\{V_M(\mathbf{x},t)\psi_\mathbf{C}(\mathbf{x},t)\}, \tag{177}$$

where

$$V_M(\mathbf{x},t) = -\int d^3\mathbf{x}' M(\mathbf{x}-\mathbf{x}')\frac{\hbar^2}{k_\mathrm{B}T}\nabla\cdot\mathbf{j}_\mathbf{C}(\mathbf{x}'). \tag{178}$$

To first approximation we can neglect all dissipation as relatively weak corrections to the PGPE evolution (163a), giving the continuity equation $\nabla\cdot\boldsymbol{j}_\mathbf{C}(\mathbf{x}) \approx -\partial n_\mathbf{C}(\mathbf{x})/\partial t$ for the c-field region and

$$V_M(\mathbf{x},t) \approx \int d^3\mathbf{x}' M(\mathbf{x}-\mathbf{x}')\frac{\hbar^2}{k_\mathrm{B}T}\frac{\partial n_\mathbf{C}(\mathbf{x}')}{\partial t}. \tag{179}$$

Thus, the scattering term generates an effective potential from dynamical density fluctuations in the c-field region.

As a specific example we consider excitations of a system with spherical symmetry, since the momentum distribution will have the same symmetry as the scattering kernel (176). We can then evaluate the effective potential for collective modes in the hydrodynamic and Thomas–Fermi approximations. For a spherically symmetric trap

the condensate wavefunction in the Thomas–Fermi approximation is $n_{\rm TF}(\mathbf{x}) = (\mu_{\rm TF}/u)(1-(r/R_{\rm TF})^2)$, with Thomas–Fermi radius $R_{\rm TF} = \sqrt{2\mu_{\rm TF}/m\omega_r^2}$. The density profile for spherically symmetric modes [204] with amplitude A can be written as

$$\delta n_n(\mathbf{x}, t) = \frac{A\mu_{\rm TF}}{u} \sin(\omega_n t) f_n(r/R_{\rm TF}), \tag{180}$$

where the radial form is given by the Jacobi polynomials $f_n(x) = \binom{n+1/2}{1/2^{-1}} P_n^{(0,1/2)}(2x^2-1)\theta(1-x)$ and $\theta(x)$ is the unit step function. Since $f_n(0) = 1$ the peak density of the excitation is $A\mu_{\rm TF}/u$. The modes have frequencies $\omega_n = \omega_r\sqrt{2n^2+3n}$, for example the breathing mode has frequency $\omega_1 = \sqrt{5}\omega_r$. Evaluating Equations (179) and (176) leads to

$$V_{M,n}(\mathbf{x}, t) = A\hbar\omega_n \cos(\omega_n t)\left(\frac{4aR_{\rm TF}^3}{\pi a_r^4}\right)\frac{e^{\beta(\epsilon_{\rm cut}-\mu)}}{(e^{\beta(\epsilon_{\rm cut}-\mu)}-1)^2} F_n(r/R_{\rm TF}), \tag{181}$$

where $a_r = \sqrt{\hbar/m\omega_r}$ is the radial harmonic oscillator length, and

$$F_n(x) = \int_0^\infty dk\, \frac{\sin(kx)}{kx} \int_0^1 {\rm d}y\, y \sin(ky) f_n(y). \tag{182}$$

In Figure 28, we show the effect of scattering on the breathing mode. At $t=0$ the density modulation (180) vanishes, but has maximal rate of change, reflected by the phase of (181) relative to (180). The radial shape of the mode $f_1(r/R_{\rm TF})$ is shown in Figure 28(a), corresponding to outward flow at $t=0$. The potential, shown in Figure 28(b) (at $t=0$), generates damping of the excitation by imposing an additional potential gradient that acts to oppose the outward flow. The same qualitative result holds for higher modes, where $V_{M,n}(r)$ is found to have the same overall shape as $f_n(r/r_{\rm TF})$ and a relative phase so as to oppose the excitations with an additional potential gradient. From Figure 28(b) it is clear

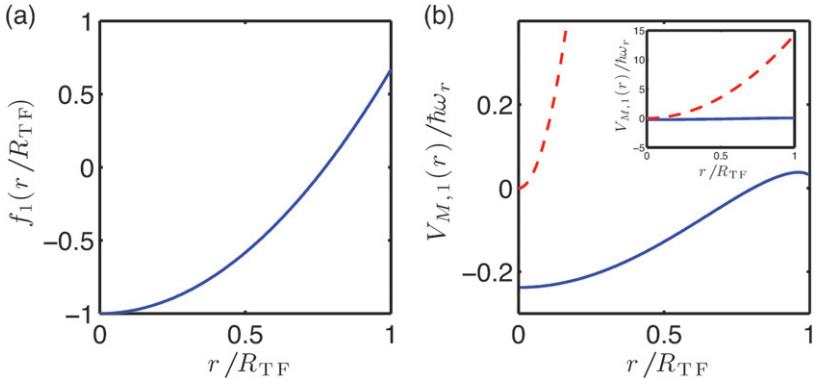

Figure 28. Scattering potential for the breathing mode $\delta n_1(r, t)$ of a Thomas–Fermi condensate. (a) The radial shape of the mode $f_1(r/R_{\rm TF})$ (see the text). (b) The scattering potential for a breathing mode excitation with amplitude $A=0.1$ (solid line, shown at $t=0$) and the harmonic trapping potential (dashed line). We have used $\epsilon_{\rm cut} = 3\mu$ and $\mu \approx \mu_{\rm TF}(N_0)$ for $T = 0.7T_{\rm c}$ and have estimated N_0 using the ideal gas relation for 10^6 ^{87}Rb atoms in a trap with radial frequency $\omega_r = 2\pi \times 25$ Hz. For these parameters $V_{M,1}(r)$ is small compared with the harmonic trap for significant radii (shown in the inset).

that $V_{M,1}(r)$ can be a significant correction to the bare trapping potential near the centre of the trap, but is unimportant near R_{TF} (see the inset).

5.3. *Simple growth SPGPE*

The scattering term of the SPGPE (163c) does not alter the population of the condensate band directly, nor does it affect the grand canonical equilibrium of the c-field. It is generally expected to be less important to the c-field dynamics in comparison to the growth term (163b), which directly describes the dominant collision processes resulting in Bose–Einstein condensation. Combined with the difficulty in its numerical implementation arising from the non-locality of the deterministic part and the multiplicative nature of the associated noise, it seems reasonable to neglect it in the first instance. This results in the simple growth SPGPE

$$\mathrm{d}\psi_{\mathbf{C}}(\mathbf{x},t)=\mathcal{P}_{\mathbf{C}}\left\{-\frac{i}{\hbar}L_{\mathbf{C}}\psi_{\mathbf{C}}(\mathbf{x},t)\mathrm{d}t+\frac{\gamma}{k_{\mathrm{B}}T}(\mu-L_{\mathbf{C}})\psi_{\mathbf{C}}(\mathbf{x},t)\mathrm{d}t+dW_{\gamma}(\mathbf{x},t)\right\}, \tag{183}$$

where

$$\langle dW_{\gamma}^{*}(\mathbf{x},t)\,dW_{\gamma}(\mathbf{x}',t)\rangle=2\gamma\delta_{C}(\mathbf{x},\mathbf{x}')\mathrm{d}t. \tag{184}$$

The numerical implementation of this simplified form is relatively straightforward, being only somewhat more complicated than the PGPE. As the only noise term is additive, the simple growth SPGPE can be integrated using high-order algorithms, such as a modified fourth-order Runge–Kutta algorithm [205].

5.4. *Applications to the dynamics of partially condensed Bose gases*

5.4.1. *Background*

The first stochastic Gross–Pitaevskii treatment of Bose gases was developed by Stoof [194] using a functional integral formulation of the Keldysh method. The first application of SGPE theory was carried out by Stoof and Bijlsma [207] who used the SGPE theory developed in [194] to study finite-temperature dynamics of a one-dimensional Bose gas. Focusing on the scenario of growth into a one-dimensional dimple trap Stamper-Kurn *et al*. studied reversible condensate formation (see [208]), and the frequencies and damping rates of collective modes. The SGPE theory has also been used in conjunction with variational techniques to study finite temperature collective excitations [207,209], and dissipative vortex dynamics [210]. More recently, Proukakis [43] have used the method to investigate quasicondensate growth into a one-dimensional dimple trap. For a deep dimple the dynamics were found to involve shockwave propagation in addition to quasicondensate formation.

Applications of the SPGPE theory are still relatively few in number. The current authors have only recently completed the implementation of the simple growth SPGPE for a harmonic trap in two dimensions with rotation, and in three dimensions without. However, even the dissipative mean-field equation obtained by neglecting all noise terms in the SPGPE has given significant insight into the dynamics of finite-temperature BECs. Here, we briefly review the applications that have appeared to date.

5.4.2. *Spontaneous vortex formation during Bose–Einstein condensation*

The formation of topological defects in symmetry-breaking phase transitions has been a topic of interest in both cosmological [211] and condensed matter [212] scenarios. Until recently quantitative models of the formation dynamics of trapped BECs have only been studied at the level of populations without allowing for the possibility of topological excitations [197–200,213,214]. The possibility of the spontaneous formation of vortices in the growth of a trapped BEC has been suggested previously by Anglin and Zurek [215] and Svistunov [216], but until recently had not been confirmed by experiment and the possibility has been the subject of much speculation [217]. Recent work by Weiler *et al.* [206] has reported the observation of spontaneous vortex formation in the growth of a trapped BEC, and compared the statistics of formation with predictions of the simple growth SPGPE (183).

Experiment. The experiments of Weiler *et al.* [206] evaporatively cooled a dilute gas of ^{87}Rb atoms from slightly above T_c in both an oblate harmonic trap and a toroidal trap formed by the addition of a Gaussian barrier from a tightly focused blue-detuned laser beam along the symmetry axis. The oblate nature of the trapping potential resulted in an energy penalty for vortices not aligned with the symmetry axis, hence improving the fidelity of vortex detection. After condensate formation and sufficiently long time-of-flight expansion, vortex cores were observed with a probability in the range 20–60%.

Theory. The results of Weiler *et al.* [206] were modelled using the simple growth SPGPE (183) matched to the growth of the condensate number in the experiments by ramping the chemical potential and temperature of the thermal cloud. For each experimental evaporative cooling ramp an ensemble of around 300 SPGPE trajectories was computed[6] and the vortex observation statistics were compared with the experimental measurements. A comparison between experimental absorption images and column densities of representative SPGPE trajectories is shown in Figure 29, with clear qualitative similarity. A comparison of the vortex observation statistics yielded quantitative agreement between experiment and the SPGPE theory. In Figure 30 a time series of density iso-surfaces is shown for a particular trajectory. The emergence of the final BEC is seen to be a turbulent process, in this case resulting in a metastable vortex.

5.4.3. *Rotating Bose–Einstein condensation*

Bradley *et al.* [192] have used the simple growth Equation (183) to model the dynamics of the formation of a *rotating* BEC [218] where it is possible for stable vortices to form *during* condensation. The following question arises: does a vortex-free condensate form before it is penetrated by vortices, or does condensation proceed into a state with vortices already present?

It is helpful to consider the single-particle energy spectrum (in the rotating frame) of the cylindrically symmetric harmonic trap in three dimensions

$$\epsilon_{nlm} = \hbar\omega_r(2n + |l| + 1) - \hbar\Omega l + \hbar\omega_z(m + 1/2), \tag{185}$$

where n, l, m are the radial, angular and axial quantum numbers. In the absence of interactions a BEC will form in the ground-state mode with energy $\epsilon_{000} = \hbar\omega_r + \hbar\omega_z/2$. Vortices arise from occupation of states with non-zero angular momentum and the positive angular momentum part of the spectrum behaves as $\hbar(\omega_r - \Omega)l$ leading to near-degeneracy

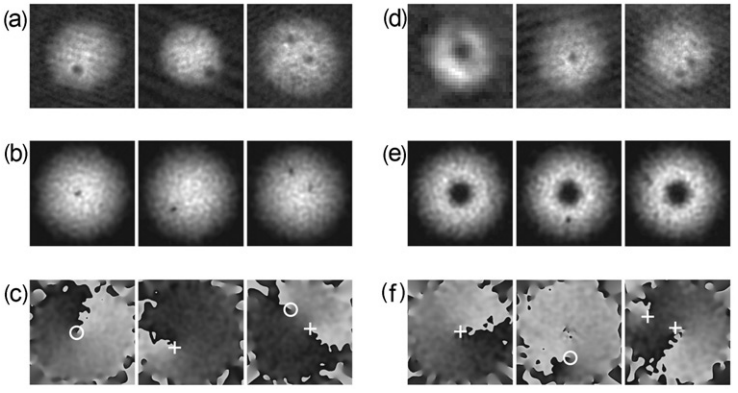

Figure 29. Spontaneous formation of vortices during Bose–Einstein condensation. (a) Images of a 200-μm^2 expansion of BECs created in a harmonic trap, showing single vortices (left, centre) and two vortices (right). Sample simulation results from evaporative cooling in a harmonic trap, showing (b) in-trap integrated column densities along z and (c) associated phase profiles in the $z=0$ plane, with vortices indicated by crosses and circles at $\pm 2\pi$ phase windings. (d) Left image: 70-μm^2 phase-contrast experimental image of a BEC in a toroidal trap; other images: vortices in 200-μm^2 expansion images of BECs created in the toroidal trap. (e), (f) Simulations of BEC growth in the toroidal trap show vortices (as in (b) and (c)) and persistent currents. Reproduced with permission from [206]. Copyright © (2004), Nature Publishing Group.

of positive angular momentum modes as $\Omega \to \omega_r$. States with angular momentum $\langle \hat{L}_z \rangle = \hbar l > 0$ are increasingly easy to populate as the rate of rotation increases.

For a rapidly rotating BEC transition, vortices can play a dominant role at all stages in the BEC growth process. It is then possible that atoms condense into a vortex-filled but spatially disordered state: a *vortex liquid*.

SPGPE treatment of rotation. In our development of the SPGPE we have included the possibility that the thermal cloud occupying **I** may be in rotational equilibrium in a symmetric trap. The transformation has consequences for the choice of $\epsilon_{\rm cut}$ and the basis of single-particle states. In harmonic oscillator units the single particle modes corresponding to (185) are also eigenstates of L_z:

$$\phi_{nlm}(r,\theta,z) = \mathcal{N}_{nlm} e^{i\theta} r^{|l|} e^{-r^2/2} L_n(r^2) e^{-z^2/2} H_m(z), \tag{186}$$

which is the appropriate basis for introducing a projection operator to separate the **C** and **I** regions. Imposing the cutoff in the rotating frame leads to a bias (in the direction of the rotation) for the angular momentum for the c-field region modes. In the limit of very fast rotation ($\Omega \to \omega_r$), z-excitations are strongly suppressed and only the lowest Landau level (LLL) is contained in the c-field if $\epsilon_{\rm cut} < \hbar\omega_z$.

In Figure 31, we show a representative SPGPE simulation of the BEC transition in a rapidly rotating system (not in the LLL regime). An initial thermal state with no condensate present is evolved subject to a sudden change in the thermal cloud temperature and chemical potential consistent with a quench below the critical point. When the final temperature after the quench is comparatively low ($T \ll T_{\rm c}$ shown here) the dynamics show a phase of rapid growth into a vortex liquid, followed by a much slower ordering phase where the vortices assemble into a regular lattice. At higher temperatures ($T \sim T_{\rm c}$),

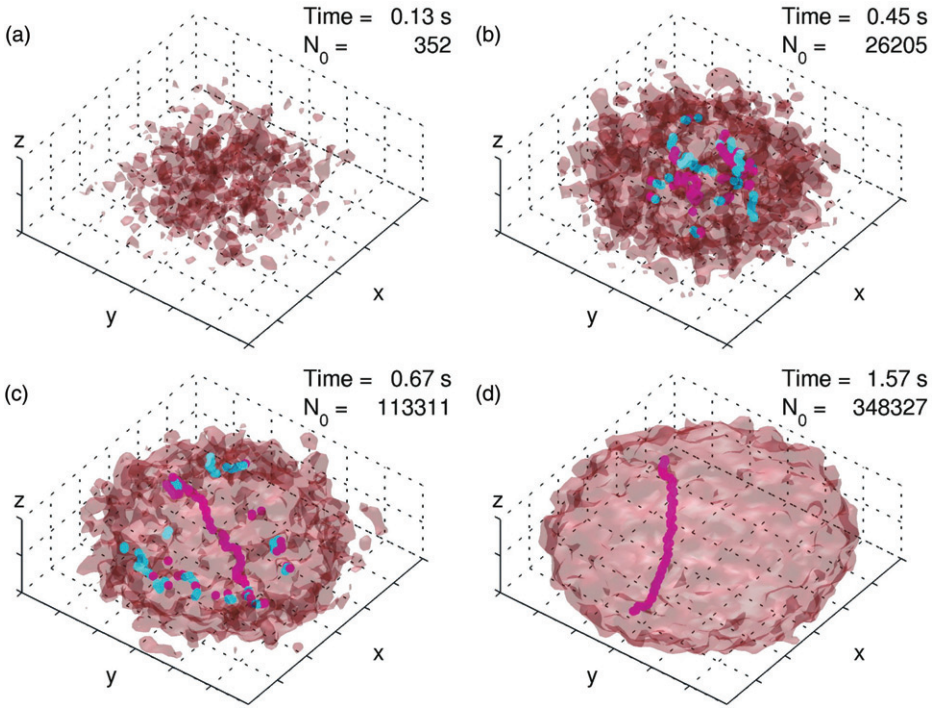

Figure 30. BEC growth dynamics. (a)–(d) Four snapshots during the simulated growth of a BEC showing isodensity surfaces (in light red) in a three-dimensional rendering. Vortex cores of opposite charges about the z-axis are indicated as magenta and cyan lines. The corresponding times are: (a) 0.13 s; (b) 0.45 s; **c**, 0.67 s; **d**, 1.57 s, where $t = 0$ s is the time when the quench is initiated in the simulation. Colour refers to the online version. Reprinted with permission from [206]. Copyright © (2004), Nature Publishing Group.

condensation into a vortex liquid still occurs but the ordering phase is frustrated by thermal fluctuations.

6. Conclusion

In this review we have outlined a unified c-field theory for studying the dynamics and statistical mechanics of ultra-cold Bose gases. The various c-field approaches considered apply to situations as diverse as the zero-temperature quantum dynamics of colliding BECs, through to the effects of critical fluctuations at the condensation transition. Perhaps one of the most surprising aspect of these approaches is that underlying them is the well-known, and computationally obliging, GPE. Two essential adaptations to the Gross–Pitaevskii theory bring this power to describe quantum and thermal effects: stochastization of the field and evolution equation, and projection onto the c-field region.

Recently, there has been increasing use of classical field techniques in the ultra-cold atom community, and particularly in the truncated Wigner approach to describe beyond-mean-field dynamics in BECs at zero temperature. Most of the classical field calculations performed at finite temperature have not made controlled use of projectors, other than the

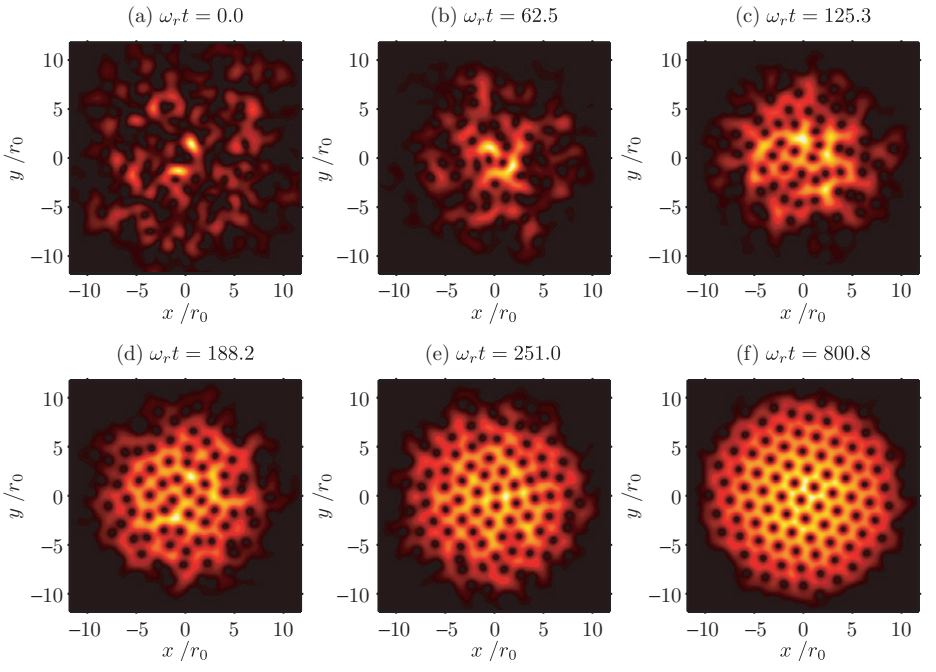

Figure 31. Rotating Bose–Einstein condensation: c-field region density for a single trajectory of the SPGPE (in the frame of the thermal cloud rotating at $\Omega_0 = 0.979\omega_r$). (a) Initial state for 1.3×10^6 ^{87}Rb atoms at $T_0 = 12$ nK, with $\mu_0 = 0.5\epsilon_{000}$. At time $t = 0$ the non-condensate band is quenched to $T = 1$ nK, $\mu = 3.5\epsilon_{000}$, and $\Omega = \Omega_0$ preserving the rotation rate. (b)–(d) The c-field region undergoes rapid growth into a vortex liquid state. (e), (f) At this low temperature the vortices then assemble into a regular Abrikosov lattice. Reproduced with permission [192]. Copyright © 2008 by The American Physical Society.

accidental projection intrinsic to the numerical representation. One of the consequences is that these results often cannot be easily related to experiment. In this review, we have extolled the virtues of a consistent energy projector used to define the c-field region, and have shown that this allows a theory that can be applied to quantitatively describe experiment.

The future development of c-field techniques is closely related to the direction in which many ultra-cold gas experiments are heading. We close this review by pointing to a few such areas under investigation:

6.1. *Full implementation of SPGPE*

To date the SPGPE scattering term has yet to be implemented numerically, primarily because of technical challenges. This term is expected to have an effect on strongly non-equilibrium scenarios such as condensate growth and unstable vortex dynamics, although it is currently not clear in what regimes it would give rise to measurable differences. Developing a formulation that can handle the dynamics of the incoherent region remains

an important future challenge which would complete the theoretical description for most practical purposes.

6.2. *General interactions*

Long-range interactions, such as dipole interactions, and strong S-wave interactions using Feshbach resonances are now routinely available in experiments. For these systems finite temperature and incoherent processes appear to become more important than in the weakly interacting S-wave case, and should be well-suited to a c-field description.

6.3. *Fermionic systems*

The quantum statistics of bosons allows for the modes of the atomic field to be highly occupied, providing the coherence central to the c-field description of the ultra-cold Bose gas. In contrast, quantum statistics prohibits multiple fermions from occupying a single mode, and thus invalidating a c-field approach at face value. A fundamental question to address is whether there is some other pathway to providing a useful c-field description of Fermi gases.

Acknowledgements

The authors gratefully acknowledge discussions and interactions with D. Baillie, A. H. Bezett, R. N. Bisset, K. Burnett, C. W. Clark, J. F. Corney, B. J. Dąbrowska-Wüster, P. D. Drummond, A. J. Ferris, C. J. Foster, T. I. A. Fudge, D. A. W. Hutchinson, P. Jain, K. V. Kheruntsyan, M. D. Lee, W. Moore, S. A. Morgan, A. A. Norrie, M. K. Olsen, B. Schneider, R. G. Scott, T. P. Simula, A. G. Sykes, T. M. Wright, S. Wüster, as well as many others who have played an important role in shaping the development of the theories and applications discussed in this review.

This work was financially supported by the University of Otago, the New Zealand Foundation for Research Science and Technology under the contracts NERF-UOOX0703: Quantum Technologies, and UOOX0801, Marsden Contract No. UOO509, the University of Queensland, and the Australian Research Council Centre of Excellence for Quantum–Atom Optics (project number CE0348178).

Notes

1. The term ‘c-field’ techniques has been coined to unify the methods discussed in this review. This terminology is derived from the name ‘*classical field* method’, often given to the pure projected GPE formalism, but which we have avoided because it can give the misleading impression that is not a quantum mechanical treatment.
2. It is worth noting that the **C** region has also been referred to as the *coherent region*, the *condensate band* or the *classical region* in the literature, although some of these names also imply additional restrictions on **C.**
3. There are several different operator orderings that are commonly used to define the quantum characteristic function, with the symmetric case being the standard choice for defining the Wigner function.
4. We consider the description of coupled **C** and **I** regions in Section 5.
5. We note that the familiar result of $\lambda = \mu$ only holds in the thermodynamic limit, and for finite size systems it is often important to ensure that the chemical potential μ and condensate eigenvalue λ are distinct.

6. Note that while this SDE gives an exact correspondence with the TWA FPE derived from Equation (140), the noise must be computed on a dense quadrature grid to ensure that the SDE preserves the correspondence (see appendix C for a discussion of quadrature methods and SDEs).
7. The difference between the effective dissipation rates in the two descriptions is usually small for weak dissipation, but the equations of motion are formally distinct. See [191] for a more detailed comparison of dissipative mean field approaches to vortex formation in BECs.
8. See the online supplementary information for [206] for a subset of trajectories showing possible outcomes for each scenario of the experiment.
9. This restriction simply allows us to avoid using cumbersome notation to account for different spectral bases in each direction, and the fully anisotropic case is of no additional computational complexity.
10. Since a polynomial of degree $2N-1$ is integrated exactly using an N-point quadrature.
11. Here, we form $e^{2|\tilde{\mathbf{x}}_{ijk}|^2}|\tilde{\psi}_{\mathbf{C}}|^2\tilde{\psi}_{\mathbf{C}}$ as this corresponds to the polynomial (P) required for the quadrature (see (A19)).

References

[1] J. Denschlag, J.E. Simsarian, D.L. Feder, Charles W. Clark, L.A. Collins, J. Cubizolles, L. Deng, E.W. Hagley, K. Helmerson, W.P. Reinhardt, S.L. Rolston, B.I. Schneider, and W.D. Phillips, Science 287 (2000), p. 97.
[2] T.P. Simula, P. Engels, I. Coddington, V. Schweikhard, E.A. Cornell, and R.J. Ballagh, Phys. Rev. Lett. 94 (2005), p. 080404.
[3] D.S. Jin, M.R. Matthews, J.R. Ensher, C.E. Wieman, and E.A. Cornell, Phys. Rev. Lett. 78 (1997), p. 764.
[4] D.A.W. Hutchinson, E. Zaremba, and A. Griffin, Phys. Rev. Lett. 78 (1997), p. 1842.
[5] B. Jackson and E. Zaremba, Phys. Rev. Lett. 88 (2001), p. 180402.
[6] A.P. Chikkatur, A. Görlitz, D.M. Stamper-Kurn, S. Inouye, S. Gupta, and W. Ketterle, Phys. Rev. Lett. 85 (2000), p. 483.
[7] Y.B. Band, M. Trippenbach, J.P. Burke, and P.S. Julienne, Phys. Rev. Lett. 84 (2000), p. 5462.
[8] C.W. Gardiner and M.J. Davis, J. Phys. B 36 (2003), p. 4731.
[9] C.J. Pethick and H. Smith, *Bose-Einstein Condensation in Dilute Gases*, 2nd ed., Cambridge University Press, Cambridge, 2002.
[10] A. Sinatra, C. Lobo, and Y. Castin, J. Phys. B 35 (2002), p. 3599.
[11] C.W. Gardiner and P. Zoller, *Quantum Noise*, 3rd ed., Springer, Berlin, 2004.
[12] D.F. Walls and G.J. Milburn, *Quantum Optics*, 2nd ed., Springer, Berlin, 1994.
[13] E. Wigner, Phys. Rev. 40 (1932), p. 749.
[14] M.O. Scully and M.S. Zubairy, *Quantum Optics*, 2nd ed., Cambridge University Press, Cambridge, 1997.
[15] A. Polkovnikov, Phys. Rev. A 68 (2003), p. 053604.
[16] C.W. Gardiner, *Handbook of Stochastic Methods*, 3rd ed., Springer, Berlin, 2004.
[17] C.W. Gardiner, Phys. Rev. A 56 (1997), p. 1414.
[18] Y. Castin and R. Dum, Phys. Rev. A 57 (1998), p. 3008.
[19] D.A.W. Hutchinson, R.J. Dodd, and K. Burnett, Phys. Rev. Lett. 81 (1998), p. 2198.
[20] D.A.W. Hutchinson, K. Burnett, R.J. Dodd, S.A. Morgan, M. Rusch, E. Zaremba, N.P. Proukakis, M. Edwards, and C.W. Clark, J. Phys. B 33 (2000), p. 3825.
[21] S.A. Morgan, M. Rusch, D.A.W. Hutchinson, and K. Burnett, Phys. Rev. Lett. 91 (2003), p. 250403.
[22] N.P. Proukakis and B. Jackson, J. Phys. B 41 (2008), p. 203002.
[23] S.A. Morgan, J. Phys. B 33 (2000), p. 3847.
[24] A. Sinatra, C. Lobo, and Y. Castin, Phys. Rev. Lett. 87 (2001), p. 210404.

[25] A. Sinatra, Y. Castin, and C. Lobo, J. Mod. Opt. 47 (2000), p. 2629.
[26] C.W. Gardiner, J.R. Anglin, and T.I.A. Fudge, J. Phys. B 35 (2002), p. 1555.
[27] M.K. Olsen, A.S. Bradley, and S.B. Cavalcanti, Phys. Rev. A 70 (2004), p. 063611.
[28] M.K. Olsen, Phys. Rev. A 69 (2004), p. 013601.
[29] A. Polkovnikov and D. Wang, Phys. Rev. Lett. 93 (2004), p. 070401.
[30] A. Polkovnikov and V. Gritsev, Nature Physics 4 (2008), p. 477.
[31] P.D. Drummond and P. Kinsler, Phys. Rev. A 40 (1989), p. R4813.
[32] P. Kinsler and P.D. Drummond, Phys. Rev. A 43 (1991), p. 6194.
[33] L.I. Plimak, M.K. Olsen, M. Fleischhauer, and M.J. Collett, Europhys. Lett. 56 (2001), p. 372.
[34] A.A. Norrie, R.J. Ballagh, and C.W. Gardiner, Phys. Rev. A 73 (2006), p. 043617.
[35] D. Jaksch, C. Bruder, J.I. Cirac, C.W. Gardiner, and P. Zoller, Phys. Rev. Lett. 81 (1998), p. 3108.
[36] P. Buonsante, V. Penna, A. Vezzani, and P.B. Blakie, Phys. Rev. A 76 (2007), p. 011602.
[37] V.A. Kashurnikov, N.V. Prokof'ev, and B.V. Svistunov, Phys. Rev. Lett. 87 (2001), p. 120402.
[38] N.V. Prokof'ev, O. Ruebenacker, and B.V. Svistunov, Phys. Rev. Lett. 87 (2001), p. 270402.
[39] P.O. Fedichev and G.V. Shlyapnikov, Phys. Rev. A 58 (1998), p. 3146.
[40] N.D. Mermin and H. Wagner, Phys. Rev. Lett. 17 (1966), p. 1133.
[41] P.C. Hohenberg, Phys. Rev. 158 (1967), p. 383.
[42] N.V. Prokof'ev and B.V. Svistunov, Phys. Rev. A 66 (2002), p. 043608.
[43] N.P. Proukakis, Laser Phys. 13 (2003), p. 527.
[44] N.P. Proukakis, J. Schmiedmayer, and H.T.C. Stoof, Phys. Rev. A 73 (2006), p. 053603.
[45] T.P. Simula and P.B. Blakie, Phys. Rev. Lett. 96 (2006), p. 020404.
[46] A.S. Bradley, P.B. Blakie, and C.W. Gardiner, J. Phys. B: At. Mol. Opt. Phys. 38 (2005), p. 4259.
[47] B.V. Svistunov, J. Mosc. Phys. Soc. 1 (1991), p. 373.
[48] Yu. Kagan, B.V. Svistunov, and G.V. Shlyapnikov, Zh. Éksp. Teor. Fiz. 101 (1992), p. 528, [JETP 75 387 (1992)].
[49] Yu. Kagan and B.V. Svistunov, Zh. Éksp. Teor. Fiz. 105 (1994), p. 353.
[50] Yu. Kagan and B.V. Svistunov, Phys. Rev. Lett. 79 (1997), p. 3331.
[51] K. Damle, S.N. Majumdar, and S. Sachdev, Phys. Rev. A 54 (1996), p. 5037.
[52] R.J. Marshall, G.H.C. New, K. Burnett, and S. Choi, Phys. Rev. A 59 (1999), p. 2085.
[53] M.J. Davis, S.A. Morgan, and K. Burnett, Phys. Rev. Lett. 87 (2001), p. 160402.
[54] K. Gòral, M. Gajda, and K. Rzążewski, Opt. Express 8 (2001), p. 92.
[55] M. Brewczyk, G. Gajda, and K. Rzążewski, J. Phys. B 40 (2007), p. R1.
[56] P.B. Blakie and M.J. Davis, J. Phys. B 40 (2007), p. 2043.
[57] F. Dalfovo, S. Giorgini, L.P. Pitaevskii, and S. Stringari, Rev. Mod. Phys. 71 (1999), p. 463.
[58] M.J. Davis, S.A. Morgan, and K. Burnett, Phys. Rev. A 66 (2002), p. 053618.
[59] K. Gòral, M. Gajda, and K. Rzążewski, Phys. Rev. A 66 (2002), p. 051602(R).
[60] W. Krauth, Phys. Rev. Lett. 77 (1996), p. 3695.
[61] O. Penrose and L. Onsager, Phys. Rev. 104 (1956), p. 576.
[62] C.N. Yang, Rev. Mod. Phys. 34 (1962), p. 694.
[63] A.J. Leggett, Rev. Mod. Phys. 73 (2001), p. 307.
[64] P.B. Blakie and M.J. Davis, Phys. Rev. A 72 (2005), p. 063608.
[65] A. Bezett, E. Toth, and P.B. Blakie, Phys. Rev. A 77 (2008), p. 023602.
[66] T.P. Simula, M.J. Davis, and P.B. Blakie, Phys. Rev. A 77 (2008), p. 023618.
[67] D. Kadio, M. Gajda, and K. Rzążewski, Phys. Rev. A 72 (2005), p. 013607.
[68] M.J. Davis, R.J. Ballagh, and K. Burnett, J. Phys. B 34 (2001), p. 4487.
[69] H.H. Rugh, Phys. Rev. Lett. 78 (1997), p. 772.
[70] H.H. Rugh, J. Phys. A: Math. Gen. 31 (1998), p. 7761.
[71] H.H. Rugh, Phys. Rev. E 64 (2001), p. 055101.
[72] M.J. Davis and P.B. Blakie, J. Phys. A: Math. Gen. 38 (2005), p. 10259.
[73] F. Gerbier, J.H. Thywissen, S. Richard, M. Hugbart, P. Bouyer, and A. Aspect, Phys. Rev. A 70 (2004), p. 013607.

[74] M.J. Davis and S.A. Morgan, Phys. Rev. A 68 (2003), p. 053615.
[75] M. Brewczyk, P. Borowski, M. Gajda, and K. Rzążewski, J. Phys. B 37 (2004), p. 2725.
[76] T.D. Lee and C.N. Yang, Phys. Rev. 105 (1957), p. 1119.
[77] T.D. Lee and C.N. Yang, Phys. Rev. 112 (1958), p. 1419.
[78] G. Baym, J.-P. Blaizot, M. Holzmann, F. Laloë, and D. Vautherin, Eur. Phys. J. B 112 (2001), p. 107.
[79] G. Baym, J.-P. Blaizot, M. Holzmann, F. Laloë, and D. Vautherin, Phys. Rev. Lett. 83 (1999), p. 1703.
[80] P. Arnold and G. Moore, Phys. Rev. Lett. 87 (2001), p. 120401.
[81] J.O. Andersen, Rev. Mod. Phys. 76 (2004), p. 5999.
[82] M. Holzmann, J.N. Fuchs, G.A. Baym, J.-P. Blaizot, and F. Laloë, C. R. Physique 5 (2004), p. 21.
[83] S. Grossmann and M. Holthaus, Phys. Lett. A 208 (1995), p. 188.
[84] S. Giorgini, L.P. Pitaevskii, and S. Stringari, Phys. Rev. A 54 (1996), p. R4633.
[85] M.J. Davis and P.B. Blakie, Phys. Rev. Lett. 96 (2006), p. 060404.
[86] F. Gerbier, J.H. Thywissen, S. Richard, M. Hugbart, P. Bouyer, and A. Aspect, Phys. Rev. Lett. 92 (2004), p. 030405.
[87] P. Arnold and B. Tomášik, Phys. Rev. A 64 (2001), p. 053609.
[88] V.L. Berezinskii, Sov. Phys. JETP 32 (1971), p. 493.
[89] J.M. Kosterlitz and D.J. Thouless, J. Phys. C: Solid State Phys. 6 (1973), p. 1181.
[90] V. Bagnato and D. Kleppner, Phys. Rev. A 44 (1991), p. 7439.
[91] L. Giorgetti, I. Carusotto, and Y. Castin, Phys. Rev. A 76 (2007), p. 013613.
[92] S. Stock, Z. Hadzibabic, B. Battelier, M. Cheneau, and J. Dalibard, Phys. Rev. Lett. 95 (2005), p. 190403.
[93] R.N. Bisset, M.J. Davis, T.P. Simula, and P.B. Blakie, Quasi-condensation and coherence in the quasi-two-dimensional trapped Bose gas, Preprint arXiv:0804.0286 (2008).
[94] M. Holzmann and W. Krauth, Phys. Rev. Lett. 100 (2008), p. 190402.
[95] M. Schellekens, R. Hoppeler, A. Perrin, J.V. Gomes, D. Boiron, A. Aspect, and C.I. Westbrook, Science 310 (2005), p. 648.
[96] A. Öttl, S. Ritter, M. Köhl, and T. Esslinger, Phys. Rev. Lett. 95 (2005), p. 090404.
[97] T. Jeltes, J.M. McNamara, W. Hogervorst, W. Vassen, V. Krachmalnicoff, M. Schellekens, A. Perrin, H. Chang, D. Boiron, A. Aspect et al., Nature 445 (2006), p. 402.
[98] S. Fölling, F. Gerbier, A. Widera, O. Mandel, T. Gericke, and I. Bloch, Nature 434 (2005), p. 481.
[99] M. Greiner, C.A. Regal, J.T. Stewart, and D.S. Jin, Phys. Rev. Lett. 94 (2005), p. 110401.
[100] T. Rom, Th. Best, D. van Oosten, U. Schneider, S. Fölling, B. Paredes, and I. Bloch, Nature 444 (2006), p. 733.
[101] R. Hanbury-Brown and R.Q. Twiss, Nature 177 (1956), p. 27.
[102] E. Altman, E. Demler, and M.D. Lukin, Phys. Rev. A 70 (2004), p. 013603.
[103] E. Toth, A.M. Rey, and P.B. Blakie, Phys. Rev. A 78 (2008), p. 013627.
[104] T. Donner, S. Ritter, T. Bourdel, A. Ottl, M. Köhl, and T. Esslinger, Science 315 (2007), p. 1556.
[105] R.J. Dodd, C.W. Clark, M. Edwards, and K. Burnett, Opt. Exp. 1 (1997), p. 284.
[106] M. Naraschewski and R.J. Glauber, Phys. Rev. A 59 (1999), p. 4595.
[107] M. Holzmann and Y. Castin, Eur. Phys. J. D 7 (1999), p. 425.
[108] Ł. Zawitkowski, M. Brewczyk, M. Gajda, and K. Rzążewski, Phys. Rev. A 70 (2004), p. 033614.
[109] M. Leadbeater, T. Winiecki, and C.S. Adams, J. Phys. B 36 (2003), pp. L143–L148.
[110] Ł. Zawitkowski, M. Gajda, and K. Rzążewski, Phys. Rev. A 74 (2006), p. 043601.
[111] E. Witkowska, M. Gajda, and J. Mostowski, J. Phys. B 40 (2007), p. 1465.
[112] A. Nunnenkamp, J.N. Milstein, and K. Burnett, Phys. Rev. A 75 (2007), p. 033604.

[113] A. Sinatra, Y. Castin, and E. Witkowska, Phys. Rev. A 75 (2007), p. 033616.
[114] C. Connaughton, C. Josserand, A. Picozzi, Y. Pomeau, and S. Rica, Phys. Rev. Lett. 395 (2005), p. 263901.
[115] C. Josserand, Y. Pomeau, and S. Rica, J. Low Temp. Phys. 145 (2006), p. 1111.
[116] A. Picozzi, Optics Express 15 (2007), p. 9063.
[117] S. Pitois, S. Lagrange, H.R. Jauslin, and A. Picozzi, Phys. Rev. Lett. 97 (2006), p. 033903.
[118] S. Lagrange, H.R. Jauslin, and A. Picozzi, Europhys. Lett. 79 (2007), p. 64001.
[119] A. Picozzi and P. Aschieri, Phys. Rev. E 72 (2005), p. 046606.
[120] H. Schmidt, K. Gòral, F. Floegel, M. Gajda, and K. Rzążewski, J. Opt. B 5 (2003), p. 96.
[121] K. Gawryluk, M. Brewczyk, M. Gajda, and K. Rzążewski, Phys. Rev. A 76 (2007), p. 013616.
[122] A. Mebrahtu, A. Sanpera, and M. Lewenstein, Phys. Rev. A 73 (2006), p. 033601.
[123] N.G. Berloff and B.V. Svistunov, Phys. Rev. A 66 (2002), p. 013603.
[124] N.G. Berloff, Phys. Rev. A 69 (2004), p. 053601.
[125] N.G. Berloff and C. Yin, J. Low Temp. Phys. 145 (2006), p. 187.
[126] N.G. Berloff and A.J. Youd, Phys. Rev. Lett. 99 (2007), p. 145301.
[127] M. Kobayashi and M. Tsubota, Phys. Rev. Lett. 69 (2004), p. 053601.
[128] R. Graham, *'Statistical theory of instabilities in stationary non-equilibrium systems with applications to lasers and nonlinear optics*, in *Quantum Statistics in Optics and Solid-State Physics*, Vol. 66, Springer Tracts in Modern Physics, G. Hohler, ed., Springer, New York, 1973, p. 1.
[129] S.J. Carter, P.D. Drummond, M.D. Reid, and R.M. Shelby, Phys. Rev. Lett. 58 (1987), p. 1841.
[130] M.J. Steel, M.K. Olsen, L.I. Plimak, P.D. Drummond, S.M. Tan, M.J. Collett, D.F. Walls, and R. Graham, Phys. Rev. A 58 (1998), p. 4824.
[131] P.D. Drummond and C.W. Gardiner, J. Phys. A: Math. Gen. 13 (1980), p. 2353.
[132] A.A. Norrie, R.J. Ballagh, and C.W. Gardiner, Phys. Rev. Lett. 94 (2005), p. 040401.
[133] M. Kozuma, L. Deng, E.W. Hagley, J. Wen, R. Lutwak, K. Helmerson, S.L. Rolston, and W.D. Phillips, Phys. Rev. Lett. 82 (1999), p. 871.
[134] J. Stenger, S. Inouye, A.P. Chikkatur, D.M. Stamper-Kurn, D.E. Pritchard, and W. Ketterle, Phys. Rev. Lett. 82 (1999), p. 4569.
[135] P.B. Blakie, R.J. Ballagh, and C.W. Gardiner, Phys. Rev. A 65 (2002), p. 033602.
[136] J. Steinhauer, N. Katz, R. Ozeri, N. Davidson, C. Tozzo, and F. Dalfovo, Phys. Rev. Lett. 90 (2003), p. 060404.
[137] A. Perrin, H. Chang, V. Krachmalnicoff, M. Schellekens, D. Boiron, A. Aspect, and C.I. Westbrook, Phys. Rev. Lett. 99 (2007), p. 150405.
[138] P.B. Blakie and R.J. Ballagh, J. Phys. B 33 (2000), p. 3961.
[139] A.J. Ferris, M.J. Davis, R.W. Geursen, P.B. Blakie, and A.C. Wilson, Phys. Rev. A 77 (2008), p. 012712.
[140] P. Deuar and P.D. Drummond, Phys. Rev. A 98 (2007), p. 120402.
[141] P.D. Drummond and J.F. Corney, Phys. Rev. A 60 (1999), pp. R2661–R2664.
[142] J.F. Corney and P.D. Drummond, Phys. Rev. A 93 (2004), p. 260401.
[143] P. Deuar and P.D. Drummond, Phys. Rev. A 66 (2002), p. 033812.
[144] M.W. Jack, Phys. Rev. Lett. 89 (2002), p. 140402.
[145] M.W. Jack, Phys. Rev. A 67 (2003), p. 043612.
[146] A.A. Norrie, R.J. Ballagh, C.W. Gardiner, and A.S. Bradley, Phys. Rev. A 73 (2006), p. 043618.
[147] E.A. Donley, N.R. Claussen, S.L. Cornish, J.L. Roberts, E.A. Cornell, and C.E. Wieman, Nature 412 (2001), p. 295.
[148] S. Wüster, B.J. Dabrowska-Wüster, A.S. Bradley, M.J. Davis, P.B. Blakie, J.J. Hope, and C.M. Savage, Phys. Rev. A 75 (2007), p. 043611.
[149] R.G. Scott, D.A.W. Hutchinson, and C.W. Gardiner, Phys. Rev. A 74 (2006), p. 053605.

[150] R.G. Scott, D.A.W. Hutchinson, and C.W. Gardiner, Las. Phys. 17 (2007), p. 527.
[151] T.A. Pasquini, Y. Shin, C. Sanner, M. Saba, A. Schirotzek, D.E. Pritchard, and W. Ketterle, Phys. Rev. Lett. 93 (2004), p. 223201.
[152] T.A. Pasquini, M. Saba, G.-B. Jo, Y. Shin, W. Ketterle, and D.E. Pritchard, Phys. Rev. Lett. 97 (2006), p. 093201.
[153] P.B. Blakie and C.W. Clark, J. Phys. B 37 (2004), p. 1391.
[154] P.B. Blakie and W.-X. Wang, Phys. Rev. A 76 (2007), p. 053620.
[155] A.K. Tuchman, C. Orzel, A. Polkovnikov, and M.A. Kasevich, Phys. Rev. A 74 (2006), p. 051601.
[156] L. Isella and J. Ruostekoski, Phys. Rev. A 72 (2005), p. 011601(R).
[157] J. Ruostekoski and L. Isella, Phys. Rev. Lett. 95 (2005), p. 110403.
[158] A.M. Rey, K. Burnett, R. Roth, M. Edwards, C.J. Williams, and C.W. Clark, J. Phys. B 36 (2003), p. 825.
[159] B.G. Wild, P.B. Blakie, and D.A.W. Hutchinson, Phys. Rev. A 73 (2006), p. 023604.
[160] C. Orzel, A.K. Tuchman, M.L. Fenselau, M. Yasuda, and M.A. Kasevich, Science 291 (2001), p. 2386.
[161] C.D. Fertig, K.M. O'Hara, J.H. Huckans, S.L. Rolston, W.D. Phillips, and J.V. Porto, Phys. Rev. Lett. 94 (2005), p. 120403.
[162] R. Bistritzer and E. Altman, Proc. Natl. Acad. Sci. USA 104 (2007), p. 9955.
[163] J. Dziarmaga, J. Meisner, and W.H. Zurek, Phys. Rev. Lett. 101 (2008), p. 115701.
[164] P. Jain, A.S. Bradley, and C.W. Gardiner, Phys. Rev. A 76 (2007), p. 023617.
[165] U. Leonhardt, T. Kiss, and P. Öhberg, Phys. Rev. A 67 (2003), p. 033602.
[166] P. Jain, S. Weinfurtner, M. Visser, and C.W. Gardiner, Phys. Rev. A 76 (2007), p. 033636.
[167] I. Carusotto, S. Fagnocchi, A. Recati, R. Balbinot, and A. Fabbri, New J. Phys. 10 (2008), p. 103001.
[168] A. Polkovnikov, Phys. Rev. A 68 (2003), p. 033609.
[169] M. Modugno, C. Tozzo, and F. Dalfovo, Phys. Rev. A 74 (2006), p. 061601.
[170] T.M. Wright, R.J. Ballagh, A.S. Bradley, P.B. Blakie, and C.W. Gardiner, Dynamical thermalization and vortex formation in stirred 2D Bose-Einstein condensates, Preprint arXiv:0808.3552 (2008).
[171] K.W. Madison, F. Chevy, W. Wohlleben, and J. Dalibard, Phys. Rev. Lett. 84 (2000), p. 806.
[172] J.R. Abo-Shaeer, C. Raman, J.M. Vogels, and W. Ketterle, Science 292 (2001), p. 476.
[173] J.R. Abo-Shaeer, C. Raman, and W. Ketterle, Phys. Rev. Lett. 88 (2002), p. 070409.
[174] E. Hodby, G. Hechenblaikner, S.A. Hopkins, O.M. Marago, and C.J. Foot, Phys. Rev. Lett. 88 (2001), p. 010405.
[175] S. Sinha and Y. Castin, Phys. Rev. Lett. 87 (2001), p. 190402.
[176] M. Tsubota, K. Kasamatsu, and M. Ueda, Phys. Rev. A 65 (2002), p. 023603.
[177] K. Kasamatsu, M. Tsubota, and M. Ueda, Phys. Rev. A 67 (2003), p. 033610.
[178] E. Lundh, J.-P. Martikainen, and K.-A. Suominen, Phys. Rev. A 67 (2003), pp. 063604–1.
[179] N.G. Parker and C.S. Adams, Phys. Rev. Lett. 95 (2005), pp. 145301–1.
[180] C. Lobo, A. Sinatra, and Y. Castin, Phys. Rev. Lett. 92 (2004), p. 020403.
[181] D.J. Heinzen, Roahn Wynar, P.D. Drummond, and K.V. Kheruntsyan, Phys. Rev. Lett. 84 (2000), p. 5029.
[182] M.K. Olsen and L.I. Plimak, Las. Phys. 14 (2004), p. 331.
[183] M.K. Olsen, Braz. Journ. Phys. 34 (2004), p. 1486.
[184] M.K. Olsen and L.I. Plimak, Phys. Rev. A 68 (2003), p. 031603.
[185] J.J. Hope and M.K. Olsen, Phys. Rev. Lett. 86 (2001), p. 3220.
[186] M.T. Johnsson and J.J. Hope, Phys. Rev. A 75 (2007), p. 043619.
[187] M.T. Johnsson, S.A. Haine, J.J. Hope, N. Robins, C. Figl, M. Jeppesen, J. Dugué, and J. Close, Phys. Rev. A 75 (2007), p. 043618.
[188] H.M. Wiseman and L.K. Thomsen, Phys. Rev. Lett. 86 (2001), p. 1143.

[189] A. Einstein, Ann. Phys. 17 (1905), p. 549.
[190] P. Langevin, Comptes. Rendues 146 (1908), p. 530.
[191] A.S. Bradley and C.W. Gardiner, The stochastic Gross-Pitaevskii equation: III, Preprint cond-mat:0602162 (2006).
[192] A.S. Bradley, C.W. Gardiner, and M.J. Davis, Phys. Rev. A 77 (2008), p. 033616.
[193] E. Zaremba, T. Nikuni, and A. Griffin, J. Low Temp. Phys. 116 (1999), p. 277.
[194] H.T.C. Stoof, J. Low Temp. Phys. 114 (1999), p. 11.
[195] C.W. Gardiner and P. Zoller, Phys. Rev. A 58 (1998), p. 536.
[196] C.W. Gardiner and P. Zoller, Phys. Rev. A 61 (2000), p. 033601.
[197] M.J. Davis, C.W. Gardiner, and R.J. Ballagh, Phys. Rev. A 62 (2000), p. 063608.
[198] C.W. Gardiner, P. Zoller, R.J. Ballagh, and M.J. Davis, Phys. Rev. Lett. 79 (1997), p. 1793.
[199] C.W. Gardiner, M.D. Lee, R.J. Ballagh, M.J. Davis, and P. Zoller, Phys. Rev. Lett. 81 (1998), p. 5266.
[200] M. Köhl, M.J. Davis, C.W. Gardiner, T.W. Hänsch, and T.W. Esslinger, Phys. Rev. Lett. 88 (2002), p. 080402.
[201] S. Choi, S.A. Morgan, and K. Burnett, Phys. Rev. A 57 (1998), p. 4057.
[202] M.D. Lee and C.W. Gardiner, Phys. Rev. A 62 (2000), p. 033606.
[203] W.H. Zurek, Physica Scripta T76 (1998), p. 186.
[204] S. Stringari, Phys. Rev. Lett. 77 (1996), p. 2360.
[205] G.N. Milstein and M.V. Tretyakov, *Stochastic Numerics for Mathematical Physics*, 2nd ed., Springer, Berlin, 2004.
[206] C.N. Weiler, T.W. Neely, D.R. Scherer, A.S. Bradley, M.J. Davis, and B.P. Anderson, Nature 455 (2004), p. 948.
[207] H.T.C. Stoof and M.J. Bijlsma, J. Low Temp. Phys. 124 (2001), p. 431.
[208] D.M. Stamper-Kurn, H.-J. Miesner, A.P. Chikkatur, S. Inouye, J. Stenger, and W. Ketterle, Phys. Rev. Lett. 81 (1998), p. 2194.
[209] R.A. Duine and H.T.C. Stoof, Phys. Rev. A 65 (2001), p. 013603.
[210] R.A. Duine, B.W.A. Leurs, and H.T.C. Stoof, Phys. Rev. A 69 (2004), p. 053623.
[211] T.W.B. Kibble, J. Phys. A 9 (1976), p. 1387.
[212] W.H. Zurek, Nature 317 (1985), p. 505.
[213] M.J. Bijlsma, E. Zaremba, and H.T.C. Stoof, Phys. Rev. A 62 (2000), p. 063609.
[214] M.J. Davis and C.W. Gardiner, J. Phys. B 35 (2002), p. 733.
[215] J.R. Anglin and W.H. Zurek, Phys. Rev. Lett. 83 (1999), p. 1707.
[216] B.V. Svistunov, Phys. Lett. A 287 (2001), p. 169.
[217] H.T.C. Stoof, Nature 447 (2007), p. 390.
[218] P.C. Haljan, I. Coddington, P. Engels, and E.A. Cornell, Phys. Rev. Lett. 87 (2001), p. 210403.
[219] P.B. Blakie, Phys. Rev. E 78 (2008), p. 026704.
[220] W. Press, S. Teukolsky, W. Vetterling, and B. Flannery, *Numerical Recipes in C*, 2nd ed., Cambridge University Press, Cambridge, UK, 1992.
[221] C.M. Dion and E. Cancès, Phys. Rev. E 67 (2003), p. 046706.
[222] W. Bao and J. Shen, SIAM J. Sci. Comput. 26 (2005), p. 2010.
[223] M. Abramowitz and I.A. Stegun, *Handbook of Mathematical Functions with Formulas, Graphs, and Mathematical Tables*, Ninth Dover printing, tenth GPO printing edition, Dover, New York, 1964.

Appendix A: Numerical technique for the harmonically trapped system

In this appendix, we give an overview of a numerical method that allows an efficient and accurate solution of the PGPE in a harmonic potential. In appendix B we briefly discuss a method for the uniform gas and refer the interested reader to [64,170,192,219] for a more detailed discussion of implementation details and applications to rotating systems.

A.1. *Numerical requirements*

The modes of the system are of central importance in the assumptions used to derive the various c-field methods presented in this review, and care must be taken in numerical implementations to ensure that the modes are faithfully represented. Any useful simulation technique must satisfy the following requirements.

(i) The space spanned by the modes of the simulation should match the c-field region as closely as possible.
(ii) All modes in the c-field regime must be propagated accurately.

The case we examine here is the PGPE for the harmonically trapped system, i.e. where

$$V_0(\mathbf{x}) = \frac{1}{2}m\omega^2(x^2 + y^2 + z^2). \tag{A1}$$

To simplify the discussion we have taken the harmonic trapping potential to be isotropic[8] and will not consider the perturbation potential δV. We take the c-field region to be defined by an energy cutoff in the single-particle basis, i.e. eigenstates of $H_0 = p^2/2m + V_0(\mathbf{x})$ with energy less than $\epsilon_{\rm cut}$.

A.2. *Spectral representation of the PGPE*

For convenience, we write the PGPE in dimensionless units to simplify the discussion, and explicitly indicate all dimensionless quantities in this section by use of tildes. We do this by introducing a unit of distance $x_0 = \sqrt{\hbar/m\omega}$ and time $t_0 = 1/\omega$. These choices immediately imply computational units for energy $E_0 = \hbar\omega$ and momentum $p_0 = \sqrt{\hbar\omega}$. So, for example, our dimensionless distance variable is defined as $\tilde{x} = x/x_0$, dimensionless time, $\tilde{t} = t/t_0$, and c-field, $\tilde{\psi}_{\mathbf{C}} = \psi_{\mathbf{C}} x_0^{3/2}$. The coefficient of the non-linear term in the GPE is given by the product u. In dimensionless units we define this as the non-linearity constant $C_{\rm NL} \equiv ut_0/\hbar x_0^3$.

In dimensionless units, the PGPE takes the form

$$i\frac{\partial\tilde{\psi}_{\mathbf{C}}}{\partial\tilde{t}} = \tilde{H}_0\tilde{\psi}_{\mathbf{C}} + \mathcal{P}_{\mathbf{C}}\{C_{\rm NL}|\tilde{\psi}_{\mathbf{C}}|^2\tilde{\psi}_{\mathbf{C}}\}, \tag{A2}$$

where

$$\tilde{H}_0 = -\frac{1}{2}\tilde{\nabla}^2 + \frac{1}{2}(\tilde{x}^2 + \tilde{y}^2 + \tilde{z}^2). \tag{A3}$$

The c-field is expanded in a spectral basis as

$$\tilde{\psi}_{\mathbf{C}}(\tilde{\mathbf{x}}, \tilde{t}) = \sum_{n\in\mathbf{C}} c_n(\tilde{t})\tilde{\phi}_n(\tilde{\mathbf{x}}), \tag{A4}$$

where $\{\tilde{\phi}_n(\tilde{\mathbf{x}})\}$ are the harmonic oscillator eigenstates of $\tilde{H}_0$ with respective eigenvalues $\tilde{\epsilon}_n$, and the $\{c_n\}$ are complex amplitudes. The projection is explicitly implemented by limiting the summation indices in (A4) to the set of values

$$\mathbf{C} = \{n : \tilde{\epsilon}_n \leq \tilde{\epsilon}_{\rm cut}\}, \tag{A5}$$

i.e. the field $\tilde{\psi}_{\mathbf{C}}$ only contains the modes of interest.

A.3. *Mode evolution*

Having used the modes of $\tilde{H}_0$ as the spectral basis and to realize the projector, we follow the Galerkin approach (i.e. projecting (A2) onto our spectral basis) to obtain the amplitude evolution equation

$$\frac{\partial c_n}{\partial\tilde{t}} = -i[\tilde{\epsilon}_n c_n + C_{\rm NL}G_n], \tag{A6}$$

where

$$G_n \equiv \int d^3\tilde{\mathbf{x}}\, \tilde{\phi}_n^*(\tilde{\mathbf{x}})|\tilde{\psi}_{\mathbf{C}}(\tilde{\mathbf{x}},\tilde{t})|^2\tilde{\psi}_{\mathbf{C}}(\tilde{\mathbf{x}},\tilde{t}), \tag{A7}$$

is the non-linear matrix element. Once this matrix elements is evaluated, the evolution of the system can be calculated using numerical algorithms for systems of ordinary differential equations, e.g. the Runge–Kutta algorithm (see [220]). Since this is a well-understood area of numerical mathematics we do not concern ourselves with the details of the propagation algorithm, but instead focus on evaluating (A7).

We can point out the central issue for numerical implementation. Expanding the fields in expression (A7) into the mode basis we obtain

$$G_n = \sum_{pqr}\left\{\int d^3\tilde{\mathbf{x}}\, \tilde{\phi}_n^*(\tilde{\mathbf{x}})\tilde{\phi}_p^*(\tilde{\mathbf{x}})\tilde{\phi}_q(\tilde{\mathbf{x}})\tilde{\phi}_r(\tilde{\mathbf{x}})\right\} c_p^* c_q c_r. \tag{A8}$$

While the matrix elements within the brackets can be calculated exactly in advance, computing all G_n values using this expression requires $O(M^4)$ floating point operations, where M is the number of c-field region modes. Such scaling would be prohibitive for performing realistic calculations. In what follows we show how to compute these matrix elements with a scheme that only requires $O(M^{4/3})$ operations. Such spectral representations have also been considered for the zero-temperature (non-projected) GPE in [221,222].

A.4. *Separability*

An important feature of the basis states (i.e. eigenstates of $\tilde{H}_0$) is that they are separable into one-dimensional eigenstates, i.e.

$$\tilde{\phi}_n(\tilde{\mathbf{x}}) \leftrightarrow \tilde{\varphi}_\alpha(\tilde{x})\tilde{\varphi}_\beta(\tilde{y})\tilde{\varphi}_\gamma(\tilde{z}), \tag{A9}$$

$$\tilde{\epsilon}_n \leftrightarrow \tilde{\varepsilon}_\alpha + \tilde{\varepsilon}_\beta + \tilde{\varepsilon}_\gamma, \tag{A10}$$

$$c_n \leftrightarrow c_{\alpha\beta\gamma}, \tag{A11}$$

where $\{\tilde{\varphi}_\alpha(\tilde{x})\}$ are eigenstates of the one-dimensional harmonic oscillator Hamiltonian, i.e.

$$\left[-\frac{1}{2}\frac{d^2}{d\tilde{x}^2} + \frac{1}{2}\tilde{x}^2\right]\tilde{\varphi}_\alpha(\tilde{x}) = \tilde{\varepsilon}_\alpha\tilde{\varphi}_\alpha(\tilde{x}), \tag{A12}$$

with eigenvalue $\tilde{\varepsilon}_\alpha = (\alpha + \frac{1}{2})$, for α a non-negative integer.

For clarity we use Greek subscripts to label the one-dimensional eigenstates, so that the specification of the c-field region in (A5) becomes

$$\mathbf{C} = \{\alpha, \beta, \gamma : \tilde{\varepsilon}_\alpha + \tilde{\varepsilon}_\beta + \tilde{\varepsilon}_\gamma \leq \tilde{\epsilon}_{\mathrm{cut}}\}. \tag{A13}$$

Within the c-field region there exists M_x ($\approx \tilde{\epsilon}_{\mathrm{cut}}$) distinct one-dimensional eigenstates (i.e. $\tilde{\varphi}_\alpha$) in each direction, and thus $M \approx \frac{1}{6}M_x^3$ three-dimensional basis states ($\tilde{\phi}_n$) in the c-field region (see the left subplot of Figure A1).

A.5. *Evaluating the matrix elements*

An important observation made in [221] was that the non-linear matrix element given in (A7) can be computed exactly with an appropriately chosen Gauss–Hermite quadrature. To show this we note

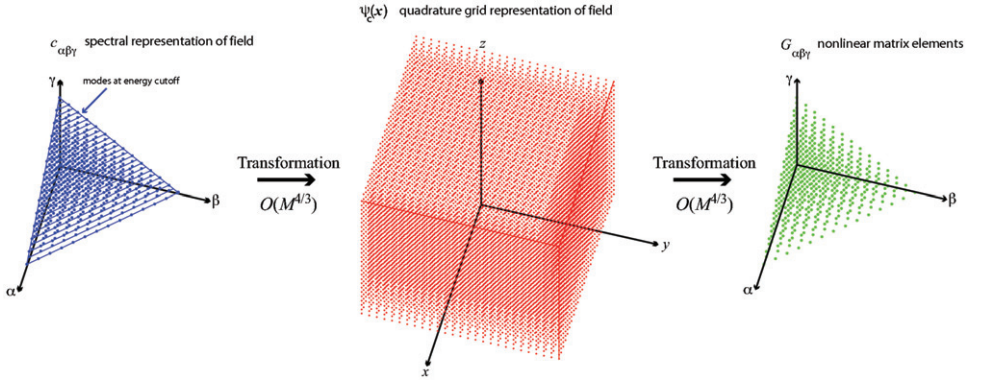

Figure A1. Schematic of numerical procedure to evaluate the non-linear matrix elements $G_{\alpha\beta\gamma}$.

that because the harmonic oscillator states are of the form $\tilde{\varphi}_\alpha(\tilde{x}) = h_\alpha H_\alpha(\tilde{x})\exp(-\tilde{x}^2/2)$, where $H_\alpha(\tilde{x})$ is a Hermite polynomial of degree α, the field (at any instant of time) can be written as

$$\tilde{\psi}_{\mathbf{C}}(\tilde{\mathbf{x}}, \tilde{t}) = Q(\tilde{x}, \tilde{y}, \tilde{z})e^{-(\tilde{x}^2+\tilde{y}^2+\tilde{z}^2)/2}, \tag{A14}$$

where

$$Q(\tilde{x}, \tilde{y}, \tilde{z}) \equiv \sum_{\{\alpha\beta\gamma\}\in\mathbf{C}} c_{\alpha\beta\gamma}(\tilde{t})h_\alpha H_\alpha(\tilde{x})h_\beta H_\beta(\tilde{y})h_\gamma H_\gamma(\tilde{z}), \tag{A15}$$

is a polynomial that, as a result of the cutoff, is of maximum degree $M_x - 1$ in the independent variables.

Similarly, it follows that because the interaction term (A7) is fourth order in the field, it can be written in the form

$$G_{\alpha\beta\gamma} = \int d^3\tilde{\mathbf{x}}\, e^{-2(\tilde{x}^2+\tilde{y}^2+\tilde{z}^2)} P_{\alpha\beta\gamma}(\tilde{x}, \tilde{y}, \tilde{z}), \tag{A16}$$

where

$$P_{\alpha\beta\gamma}(\tilde{x}, \tilde{y}, \tilde{z}) \equiv h_\alpha H_\alpha(\tilde{x})h_\beta H_\beta(\tilde{y})h_\gamma H_\gamma(\tilde{z})|Q(\tilde{x}, \tilde{y}, \tilde{z})|^2 Q(\tilde{x}, \tilde{y}, \tilde{z}), \tag{A17}$$

is a polynomial of maximum degree $4(M_x - 1)$ in the independent variables. To evaluate these integrals, we note the general form of the N_Q point Gauss–Hermite quadrature

$$\int_{-\infty}^{+\infty} d\tilde{x}\, w(\tilde{x})f(\tilde{x}) \approx \sum_{j=1}^{N_Q} w_j f(\tilde{x}_j), \tag{A18}$$

where $w(\tilde{x})$ is a Gaussian weight function, and the N_Q values of w_j and x_j are the quadrature weights and roots, respectively (see [223]). This quadrature is exact if $f(\tilde{x})$ a polynomial of maximum degree $2N_Q - 1$.

Identifying the exponential term in (A16) as the usual weight function for quadrature, the integral can be exactly evaluated using a three-dimensional spatial grid of $8(M_x - 1)^3$ points (i.e. $2(M_x - 1)$ points in each direction[9]), i.e.

$$G_{\alpha\beta\gamma} = \sum_{ijk} w_i w_j w_k P_{\alpha\beta\gamma}(\tilde{x}_i, \tilde{x}_j, \tilde{x}_k), \tag{A19}$$

where $\tilde{x}_i$ and w_i are the $2(M_x-1)$ roots and weights of the one-dimensional Gauss–Hermite quadrature with weight function $w(\tilde{x})=\exp(-2\tilde{x}^2)$ (see [223]). Note that owing to the isotropy of the trapping potential, the quadrature grids in all spatial directions are identical.

A.6. *Overview of numerical procedure*

Here, we briefly overview how the quadrature described above can be efficiently implemented numerically. We require the transformation matrices, given by one-dimensional basis states evaluated on the quadrature grid, i.e.

$$U_{i\alpha}=\tilde{\varphi}_\alpha(\tilde{x}_i), \tag{A20}$$

to be pre-calculated. Starting from the basis set representation of the field (i.e. $\{c_{\alpha\beta\gamma}\}$) at an instant of time $\tilde{t}$, the steps for calculating the matrix elements are as follows (also see Figure A2).

(i) Transform from spectral to spatial representation:

$$\tilde{\psi}_{\mathbf{C}}(\tilde{\mathbf{x}}_{ijk},\tilde{t})=\sum_{\{\alpha\beta\gamma\}\in\mathbf{C}} U_{i\alpha}U_{j\beta}U_{k\gamma}c_{\alpha\beta\gamma}(\tilde{t}), \tag{A21}$$

where $\tilde{\mathbf{x}}_{ijk}=(\tilde{x}_i,\tilde{x}_j,\tilde{x}_k)$.

(ii) The quadrature integrand of the non-linear matrix element (A7) is constructed by appropriately dividing by the weight function and pre-multiplying by the weights[10], i.e.

$$g(\tilde{\mathbf{x}}_{ijk})\equiv w_i w_j w_k e^{2|\tilde{\mathbf{x}}_{ijk}|^2}|\tilde{\psi}_{\mathbf{C}}(\tilde{\mathbf{x}}_{ijk},\tilde{t})|^2\tilde{\psi}_{\mathbf{C}}(\tilde{\mathbf{x}}_{ijk},\tilde{t}). \tag{A22}$$

(iii) Inverse transforming these integrand functions yields the desired matrix elements:

$$G_{\alpha\beta\gamma}=\sum_{ijk} U^*_{i\alpha}U^*_{j\beta}U^*_{k\gamma}g(\tilde{\mathbf{x}}_{ijk}). \tag{A23}$$

The slowest step in this procedure is carrying out the basis transformation, which requires $O(M_x^4)$, i.e. $O(M^{4/3})$ floating point operations when carried out as a series of matrix multiplications. Typical simulations, where we evolve a c-field field with $M\approx 2000$ modes for 100 trap periods, take about 2 hours.

Appendix B: Numerical technique for the uniform system

B.1. *Spectral representation*

The basic quadrature arguments presented for the harmonic oscillator case can be applied to the numerical description of the uniform Bose gas. In this section we briefly discuss the uniform case, referring to results from Appendix A where they are the same. The system of interest is taken to be in a cuboid volume with linear dimensions $\{L,L,L\}$ and subject to periodic boundary conditions.

The dimensionless PGPE takes the same form as in Equation (A2), but with a basis Hamiltonian of the form

$$\tilde{H}_0=-\frac{\tilde{\nabla}^2}{(2\pi)^2}, \tag{B1}$$

where we take periodic boundary conditions,

$$\tilde{\psi}_{\mathbf{C}}(\tilde{x}+1,\tilde{y},\tilde{z})=\tilde{\psi}_{\mathbf{C}}(\tilde{x},\tilde{y}+1,\tilde{z})=\tilde{\psi}_{\mathbf{C}}(\tilde{x},\tilde{y},\tilde{z}+1)=\tilde{\psi}_{\mathbf{C}}(\tilde{x},\tilde{y},\tilde{z}), \tag{B2}$$

and have used $x_0=L$ and $t_0=mL^2/\pi h$ as the units of length and time.

As in the harmonic case (see Equations (A9)–(A11)) the basis states are separable into one-dimensional eigenstates (i.e. $\tilde{\phi}_n(\tilde{\mathbf{x}}) = \tilde{\varphi}_\alpha(\tilde{x})\tilde{\varphi}_\beta(\tilde{y})\tilde{\varphi}_\gamma(\tilde{z})$) of the form

$$\tilde{\varphi}_\alpha(\tilde{x}) = e^{i\tilde{k}_\alpha \cdot \tilde{x}}, \tag{B3}$$

with the wavevectors $\tilde{k}_\alpha$ chosen as harmonics of the periodicity interval, i.e. $\tilde{k}_\alpha = 2\pi\alpha$, with α an integer, and respective eigenvalues $\tilde{\varepsilon}_\alpha = \alpha^2$. The values of the indices $\{\alpha, \beta, \gamma\}$ specifying the c-field region is given by Equation (A13), which defines a sphere of radius $\sqrt{\tilde{\epsilon}_{\rm cut}}$ in $\alpha\beta\gamma$ space for the uniform system. For later convenience we define $\alpha_{\max}$ as the maximum value of α that occurs in $\mathbf{C}$, i.e. the highest-order basis state in each direction. For the planewave case we have $\alpha_{\max} \simeq \sqrt{\tilde{\epsilon}_{\rm cut}}$, and thus in the c-field region we have a total of $M_x = 2\alpha_{\max} + 1$ distinct one-dimensional basis states (i.e. $\tilde{\varphi}_\alpha$) in each direction, with $M \approx (\pi/6)M_x^3$ three-dimensional basis states (i.e. $\tilde{\phi}_n$).

B.2. *Evaluating the matrix elements*

In the planewave spectral representation the PGPE takes the form (A6), for which the main challenge is evaluating the non-linear matrix element (A7). We now show how a quadrature approach can be used to evaluate this matrix element exactly. The essence of this approach is to transform the field to a spatial representation where the non-linear term is local.

In each spatial dimension, the quadrature grid of interest (for the uniform case) consists of $N_{\rm Q}$ equally spaced points given by

$$\tilde{x}_j = j\Delta\tilde{x}, \quad 1 \le j \le N_{\rm Q}, \tag{B4}$$

with spacing $\Delta\tilde{x} = 1/N_{\rm Q}$, which spans the spatial region $(0, 1]$. The quadrature expression for an integral of an arbitrary function f is

$$\int_0^1 d\tilde{x}\, w(\tilde{x}) f(\tilde{x}) \approx \sum_{j=1}^{N_{\rm Q}} w_j f(\tilde{x}_j), \tag{B5}$$

where $w(\tilde{x}) = 1$ is the weight function, and $w_j = \Delta\tilde{x}$. That is, for the planewave approach, the quadrature rule is the well-known *rectangular rule* from elementary numerical analysis.

The requirement that our quadrature will exactly calculate the non-linear matrix elements is equivalent to the requirement that the one-dimensional integrals between are all products of four $\tilde{\varphi}_j(\tilde{x})$ are evaluated exactly, i.e.

$$I_{\alpha\beta\gamma\delta} = \sum_{j=1}^{N_{\rm Q}} \Delta\tilde{x}\tilde{\varphi}_\alpha^*(\tilde{x}_j)\tilde{\varphi}_\beta^*(\tilde{x}_j)\tilde{\varphi}_\gamma(\tilde{x}_j)\tilde{\varphi}_\delta(\tilde{x}_j), \quad -\alpha_{\max} \le \alpha, \beta, \gamma, \delta \le \alpha_{\max}, \tag{B6}$$

$$= \delta_{\alpha+\beta,\gamma+\delta}, \tag{B7}$$

which holds for the quadrature described above if we take $N_{\rm Q} \ge 2M_x$. Thus, the most efficient and accurate representation is when we choose $2M_x$ grid points in each spatial dimension.

B.2.1. *Fourier interpretation*

The quadrature grid requirement ($N_{\rm Q} = 2M_x$) can be interpreted in terms of Fourier properties of the spatial grid. To represent a maximum wavevector of $\tilde{k}_{\rm cut} = 2\pi\alpha_{\max} \approx \pi M_x$, the Nyquist requirement for the spatial grid is that the distance between points should be $\Delta\tilde{x} = 1/M_x$ (or smaller), which requires at least M_x points over the interval $(0, 1)$. However, our quadrature argument above was that to evaluate the non-linear matrix elements correctly we need twice as many grid points, i.e. $N_Q = 2M_x$. Such a grid is sufficient to satisfy the Nyquist condition for wavevectors of magnitude up to $2\tilde{k}_{\rm cut}$. To understand why we need so many points consider the *worst case* for the matrix element in (B6): the case $-\alpha = -\beta = \gamma = \delta = \alpha_{\max}$, i.e. where all modes occur with the maximum magnitude wavevector $\tilde{k}_{\rm cut}$. The integrand of (B6), i.e. the product of these four modes, is itself a planewave with

wavevector $4\tilde{k}_{\rm cut}$. On the spatial grid with $2M_x$ points this cannot be represented unambiguously (i.e. it exceeds the Nyquist limit of $2\tilde{k}_{\rm cut}$), and is aliased. However, for the choice of $2M_x$-points, this aliasing does not map the wavevector into the region $[-\tilde{k}_{\rm cut}, \tilde{k}_{\rm cut}]$, and hence does not effect the matrix elements evaluated for the c-field region. For any fewer points the aliased wavevector maps into $[-\tilde{k}_{\rm cut}, \tilde{k}_{\rm cut}]$, and gives rise to spurious dynamics.

B.3. *Overview of numerical procedure*

We could apply an identical procedure to that discussed in Section A.6 to evaluate the matrix elements with a computational cost per evaluation of $O(M^4)$. However, for the planewave case the basis transformation between spectral (momentum space) and position space quadrature grids (i.e. steps (i) and (iii) in Section A.6) is equivalent to a fast Fourier transformation, which has a computational cost of $O\ (M^3\ \log(M))$. For more details on the planewave procedure we refer the reader to [219].

Appendix C: Mapping to stochastic equations

The utility of phase-space methods requires that the equation of motion for the quasi-probability distribution (here (58)) can be mapped to an equivalent SDE, which is comparatively much easier to solve. A projected functional FPE of the form

$$\begin{aligned}\frac{\partial P}{\partial t} = \int d^3\mathbf{x}\Big\{ &-\frac{\bar{\delta}}{\bar{\delta}\psi_{\mathbf{C}}(\mathbf{x})} A\big(\psi_{\mathbf{C}}(\mathbf{x}), \psi^*_{\mathbf{C}}(\mathbf{x}), t\big) + \text{h.c.} \\ &+ \frac{\bar{\delta}^2}{\bar{\delta}\psi_{\mathbf{C}}(\mathbf{x})\bar{\delta}\psi_{\mathbf{C}}(\mathbf{x})} D_{11}\big(\psi_{\mathbf{C}}(\mathbf{x}), \psi^*_{\mathbf{C}}(\mathbf{x}), t\big) + \text{h.c.} \\ &+ \frac{\bar{\delta}^2}{\bar{\delta}\psi_{\mathbf{C}}(\mathbf{x})\psi^*_{\mathbf{C}}(\mathbf{x})} D_{12}\big(\psi_{\mathbf{C}}(\mathbf{x}), \psi^*_{\mathbf{C}}(\mathbf{x}), t\big) + \text{h.c.}\Big\} P,\end{aligned} \tag{C1}$$

with drift vector $\boldsymbol{A} = [A, A^*]$ and diffusion matrix $\mathbf{D} \equiv [D_{11}, D_{12}; D^*_{12}, D^*_{11}]$ has an equivalent stochastic equation if the diffusion matrix is positive semi-definite. A factorization of the diffusion matrix in the form $\boldsymbol{D} = \boldsymbol{B}\boldsymbol{B}^T$ can then be found, and the Itô SDE is given by

$$\mathbf{d}\boldsymbol{\psi}_{\mathbf{C}}(\mathbf{x}, t) = \mathcal{P}_{\mathbf{C}}\big\{\mathbf{A}(\mathbf{x}, t)\mathrm{d}t + \mathbf{B}(\mathbf{x}, t)\,\mathbf{dW}(\mathbf{x}, t)\big\} \tag{C2}$$

where $\mathbf{d}\boldsymbol{\psi}_{\mathbf{C}} = [d\psi_{\mathbf{C}}, \mathrm{d}\psi^*_{\mathbf{C}}]^{\mathrm{T}}$, $\mathcal{P}_{\mathbf{C}} = [\mathcal{P}_{\mathbf{C}}, \mathcal{P}^*_{\mathbf{C}}]^{\mathrm{T}}$ and $\mathbf{dW}(\mathbf{x}, t)$ is a vector of noises. In general, mapping to ordinary SDEs is only possible if the equation of motion for the quasi-probability is strictly a FPE (derivatives up to second order).

There is an important technical point regarding the equivalence of (C1) and (C2). The strict equivalence holds only if the projector $\mathcal{P}_{\mathbf{C}}$ is implemented with sufficient care. In the language of Section A.5, the quadrature chosen to compute (C2) must be sufficient to generate a c-field delta function of the appropriate numerical order upon stochastic averaging. The standard proofs of equivalence [16] can be adapted to show that for a diffusion term of polynomial degree $2D_x$, giving $\boldsymbol{B}$ of degree D_x, the delta function must to be a true delta function for terms up to order $D_x + M_x$, requiring expansion of the noise up to states of degree $D_x + M_x$ and implementation of Equation (C2) using a numerical quadrature rule sufficient to integrate terms of order $2D_x + 2M_x$ or a rule of order $D_x + M_x - 1$ to generate the appropriate equivalence.